Adaptive Array Processing Techniques for Terrain Scattered Interference Mitigation

A THESIS

Presented to

The Academic Faculty

By

Stephen Michel Kogon

In Partial Fulfillment

of the Requirements for the Degree of

Doctor of Philosophy in Electrical Engineering

Georgia Institute of Technology

December 1996

Adaptive Array Processing Techniques for Terrain Scattered Interference Mitigation

Approved:

Douglas B. Williams, Chairman

James H. McClellan

E. Jeff Holder

Date approved by Chairman December 19, 1996

Dedicated to the memory of the women who have most influenced my life:

Shirley Kogon and Charlotte Kogon

Acknowledgments

First and foremost, thanks to God for giving me the strength, the ambition, and the ability to complete this thesis.

There are a number of people I also wish to thank for their help and support during my graduate studies at Georgia Tech. First, I would like to thank my advisor, Professor Doug Williams, for his guidance throughout this thesis research. He has always given me the freedom to choose my own direction, while offering critical advice when it was needed. My thanks go out to Jeff Holder at GTRI, who has has always given freely of his time and was my first teacher in radar signal processing. I am also indebted to Bob Gabel from MIT Lincoln Laboratory, not only for flying down to Atlanta for the thesis defense, but for also being so generous with his time throughout the last few years. Thanks to Professor Jim McClellan for being part of my thesis reading committee and for always taking the time to give advice at various stages along the way. I am grateful to Jeff Schodorf and Yaron Seliktar for our many discussions that have increased my understanding of various signal processing topics. I also would like to express my sincere appreciation to Kay Gilstrap and Stacy Schultz for all the help they have given me throughout my stay at Georgia Tech. In addition, I would like to thank the many people who have taken the time to read through various portions of this thesis, making valuable suggestions that improved its quality.

Thanks to all the faculty at the Center for Signal and Image Processing of Georgia Tech for creating such a fertile learning environment. On a personal level, I would like to thank Osama Al-Shaykh, David Anderson, Joey Arrowood, Halûk

Aydınoğlu, Kevin Bowman, James DeBardelaben, Dan Drake, Antonio Gentile, T.J. Klausutis, Chris Lanciani, Mike Macon, Alvaro Marenco, Darnell Moore, Ram Rao, Richard Rau, Jeff Schodorf, Yaron Seliktar, and Jonathon Su for providing friendship and for helping to make my time at Georgia Tech an enjoyable one.

I am grateful to Dimitris Manolakis for sparking my interest in signal processing and providing constant encouragement throughout my graduate studies. I would also like to express my gratitude to the many people at MIT Lincoln Laboratory who have been very generous with their time. In particular, I would like to thank Michael Zatman for the many discussions on his trips to Atlanta and for encouraging me to pursue career opportunities at Lincoln Labs.

A special thanks go out to all the members of my family for their love and support over the years. Thanks to my mother, Shirley Kogon, for teaching me so many of the important things about life. The only thing I regret is that we had such a short time together. I know you are looking down on me today and smiling. Thanks also to my father, Rainer Kogon, for initially getting me interested in math and science and teaching me the importance of putting forth an effort in everything I do. Also thanks to my grandmother, Charlotte Kogon, for acting as a mother to me at a critical time in my life. I am grateful to my sister, Marny Kogon, for always being there for me and for being more supportive than I could ever imagine. A very special thanks to Marge Duprey and Renate Menzinger for filling an important void in my life as my new "mothers." My gratitude also goes out to my wife's parents, Ray and Kathy Tomasetti, for taking me in as one of their own.

Last but certainly not least, thanks to my wonderful wife, Lorna, for helping me to realize all my dreams. By offering your love, support, and affection, you have helped me not only endure, but enjoy every step of the way.

Contents

List of Tables

List of Figures

Summary

The mitigation of terrain scattered interference (TSI) in airborne radar sensor arrays presents a unique adaptive array processing problem. TSI is produced by jammer multipath reflections that are incident on the radar from a large sector of the azimuth plane. Often, the interference is found throughout the mainbeam of the receiver array, precluding any spatial nulling methods. Instead, TSI mitigation techniques use temporal correlation found in the returns to achieve interference suppression. A beamspace canceler is proposed that uses TSI energy found in the spatial sidelobes of the mainbeam to estimate and remove the mainbeam TSI. The method is shown to have several important advantages over the currently used method, the single-reference beam canceler. Namely, the beamspace canceler is able to effectively mitigate TSI produced by airborne jammers without the use of Doppler compensation channels and is implemented with a drastic reduction in the blind interval. The proposed method is demonstrated on experimental TSI collected as part of the DARPA/Navy Mountaintop program. An extension of the beamspace canceler is also proposed for mainbeam jammer cancellation where the target and jammer are spatially co-located.

Another important aspect of this thesis is the investigation of issues essential for the implementation of the beamspace canceler in actual airborne radar systems. First, a number of rank reduction strategies are investigated for the TSI mitigation problem. Rank reduction is necessary due to computational restrictions and sample support limitations. Another important issue is the mitigation of combinations of

TSI and monostatic clutter since actual airborne radars almost inevitably contain ground clutter returns. Using an extension of the beamspace TSI canceler, a factored mitigation approach is proposed that performs TSI mitigation in the entire beamspace domain to preserve the spatial dimension of the data. Then, the output of the TSI cancellation stage can make use of all the spatial degrees of freedom to perform space-time adaptive processing (STAP) for monostatic clutter suppression. Results with experimental data comparing the performance of the proposed method to single-beam TSI mitigation with moving target indicator (MTI) clutter nulling are presented.

CHAPTER 1

Introduction

The goal of pulsed airborne surveillance radar systems is to detect targets in the presence of interference. The interference sources most often considered are hostile stand-off barrage noise jammers and monostatic clutter. These types of interference can be effectively mitigated in the element-pulse or azimuth-Doppler domains using space-time adaptive processing (STAP) techniques. STAP is able to reduce their contributions below the thermal noise floor [67]. Terrain scattered interference (TSI), also known as hot clutter, is another type of interference encountered by airborne radar systems [17, 19]. Rather than directly jamming the radar receiver, hostile jammers produce TSI by directively transmitting energy at large surface scatterers to generate terrain reflections in the direction of the airborne radar. Since the scatterers are spatially distributed, the radar system observes TSI energy in a large portion of the angular spectrum. As a result, target detection is severely hampered in these regions. The interference is distributed throughout the mainbeam and is therefore spatially coherent with the target. In addition, the terrain reflections tend to decorrelate in time, so that the TSI is approximately uncorrelated from one pulse to the next. However, the mainbeam interference is produced by several multipath reflections of the original jammer signal impinging on the radar receiver. Each multipath reflection is due to a different scatterer and has a different path length from the jammer source to the receiver. Therefore, each received TSI signal is a weighted delayed version of the source, and the mainbeam interference is simply the summation of

these delayed replicas. As a result, mainbeam TSI contains a significant amount of temporal or range correlation, often over large time spans because of the differences in the propagation paths of the various signals.

Adaptive TSI cancellation methods focus on exploiting temporal correlation in the returns. A number of analog adaptive methods have been proposed, starting with Morgan and Athanasios, who were the first to consider the mitigation of TSI, although in the form of wideband sidelobe interference [50]. Fante proposed a bandwidth partitioning method using tapped delay lines within the individual subbands [17, 33]. More recently, Fante and Torres proposed a 3-D adaptive method [19] based on a TSI model for which the ideal covariance statistics were derived in order to find the adaptive weights. However, this method becomes computationally intensive for the number of elements and pulses typically used in real-time systems. In addition, this technique, as with all of the other analog methods, requires the a priori estimation of covariance statistics and fails to address the rapid decorrelation of TSI, even from pulse to pulse. For this reason, the adaptive weights need to be recursively computed and applied within a short time period, preferably from the same set of returns. A discrete-time method proposed by Doherty uses an adaptive filter, matched to the transmitted waveform, for single-channel TSI mitigation [16]. However, this method assumes a narrowband TSI model which is inconsistent with actual TSI returns [40].

The only TSI cancellation method that has been successfully demonstrated on experimental data is the single-reference beam (SRB) canceler [5, 21, 22]. This canceler predicts the mainbeam TSI from the jammer direct-path signal that is acquired by steering a reference beam toward the jammer location. Unfortunately, the large correlation time spans typically present in the returns necessitate a large number of temporal taps on the reference beam for this method. As a result, a large blind interval exists at the beginning of each processing interval over which target detection performance is degraded. In addition, the SRB canceler requires the use of Doppler compensation channels for the mitigation of TSI produced by airborne

jammers. However, Doppler compensation requires a large increase in the adaptive degrees of freedom, as well as the a priori estimation of each Doppler component, making its use undesirable.

In this thesis, a new beamspace TSI canceler is proposed that makes use of TSI returns present in the spatial sidelobes of the mainbeam. Auxiliary beams are used to collect this sidelobe TSI energy. These TSI signals contain significant correlation with the mainbeam interference and can be used for cancellation purposes instead of the direct-path signal used by the SRB canceler. The proposed method is shown to achieve a significant improvement in the cancellation of TSI produced by airborne jammers without the use of Doppler compensation channels. Also, the exploitation of the additional spatial information diminishes the size of the temporal window and, consequently, the blind interval. The canceler is implemented using the sample matrix inversion (SMI) technique. Diagonal loading of the sample covariance matrix is shown to provide robustness for the SMI adaptive weights.

An important issue with the beamspace TSI canceler is its integration into an actual airborne radar system. Computational and sample support limitations motivate the use of rank reduction methods to decrease the degrees of freedom necessary for the adaptive processor. A variety of existing methods are studied as part of this thesis. Another important consideration is the fact that TSI is seldom the only type of interference present. For the airborne scenario monostatic clutter returns are also present when the radar is in search mode since the receiver is transmitting energy in order to detect targets. Therefore, the mitigation of combinations of TSI and monostatic clutter is the more likely problem that needs to be addressed. A factored approach is proposed, performing TSI mitigation followed by monostatic clutter nulling. The factoring of the processing is necessary due to the limited sample support imposed by the non-stationary nature of monostatic clutter returns. The proposed method performs full beamspace mitigation of TSI in order to preserve the spatial dimension. A complete TSI-filtered CPI data-cube is passed on to the monostatic clutter nulling

stage which enables the use of STAP techniques. The proposed method is compared to single-beam TSI mitigation with moving target indicator (MTI) clutter nulling on experimental returns, also collected as part of the DARPA/Navy Mountaintop program.

The last portion of this thesis proposes the extension of the beamspace canceler to another problem: mainbeam jammer cancellation. In this problem, the jammer is so close to the target that the two essentially share the same spatial location. As a result, spatial only processing is not an option, since it forces an adaptive null in the direction of the jammer and the target. However, the beamspace canceler can be employed to collect incidental jammer multipath returns. The multipath signals from the auxiliary beams of the canceler are used to estimate and remove the mainbeam direct-path jammer signal. The method is demonstrated on experimental returns for which it is shown to achieve greater than 10 dB of suppression of the mainbeam jammer signal.

CHAPTER 2

Background

Background material pertaining to terrain scattered interference mitigation is presented in this chapter. The chapter begins with some fundamental concepts of both radar and array signal processing. Then, surveillance airborne radar systems are discussed, including operation in pulsed mode, sampling of the individual pulses, and the structure in which the data is collected. Next, the target signal is described along with the different types of traditional interference and their mitigation using space-time adaptive processing. The chapter concludes with an overview of terrain scattered interference and the mitigation method currently used for its suppression.

2.1 Fundamentals

This section addresses some of the fundamental concepts in radar and array signal processing. In addition, assumptions and notation to be used throughout the thesis are stated at this time. Several detailed textbooks exist in both the areas of radar [41, 51, 57, 58] and array processing [15, 30, 32, 48]. The interested reader should consult these references for a more detailed treatment of these topics.

2.1.1 Radar Fundamentals

A radar signal is produced by a transmitter. The signal propagates through the atmosphere until it experiences an object from which it is reflected. The portion of

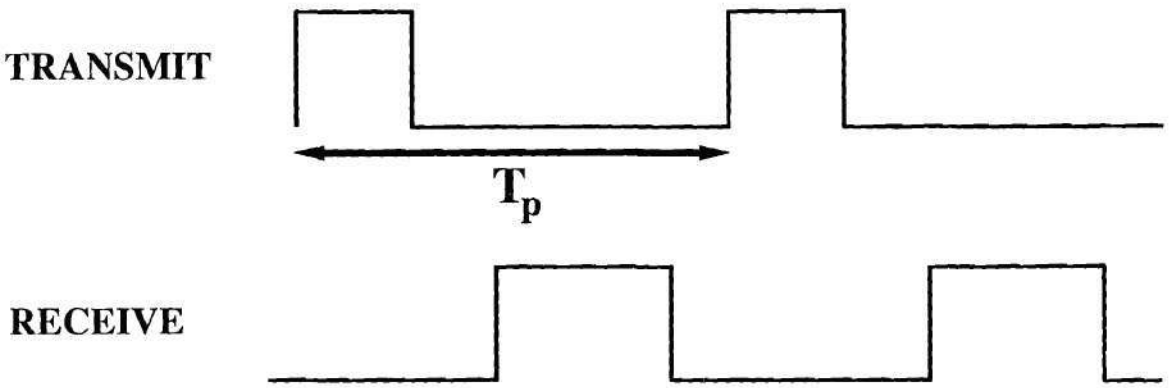

Figure 2.1: Radar operation in pulsed transmit/receive mode.

the signal reflected back in the direction of the radar, known as the radar echo, is then measured by the radar receiver. The changes in the returned radar signal yield important information about potential targets, such as their distance and relative velocity with respect to the radar. Many radar systems have an antenna that performs both the transmit and receive functions. Since both operations cannot occur simultaneously, the radar operates in pulsed mode, transmitting for a period of time (the pulse) and then receiving for a period of time. Fig. 2.1 shows the transmit and receive periods for a pair of pulses. Note that transmit and receive periods do not necessarily have equal time durations. Assuming the pulses are transmitted at a constant frequency, f_p, known as the pulse repetition frequency (PRF), the inter-pulse period is

$$T_p = \frac{1}{f_p} \, . \tag{2.1}$$

The antenna is also characterized by its transmit and receive responses that determine the strength at which the radar signal is transmitted or received as a function of direction. For the purposes of this thesis, the antenna is assumed to be omnidirectional, meaning that it has an equal response in all directions for both transmit and receive operations.

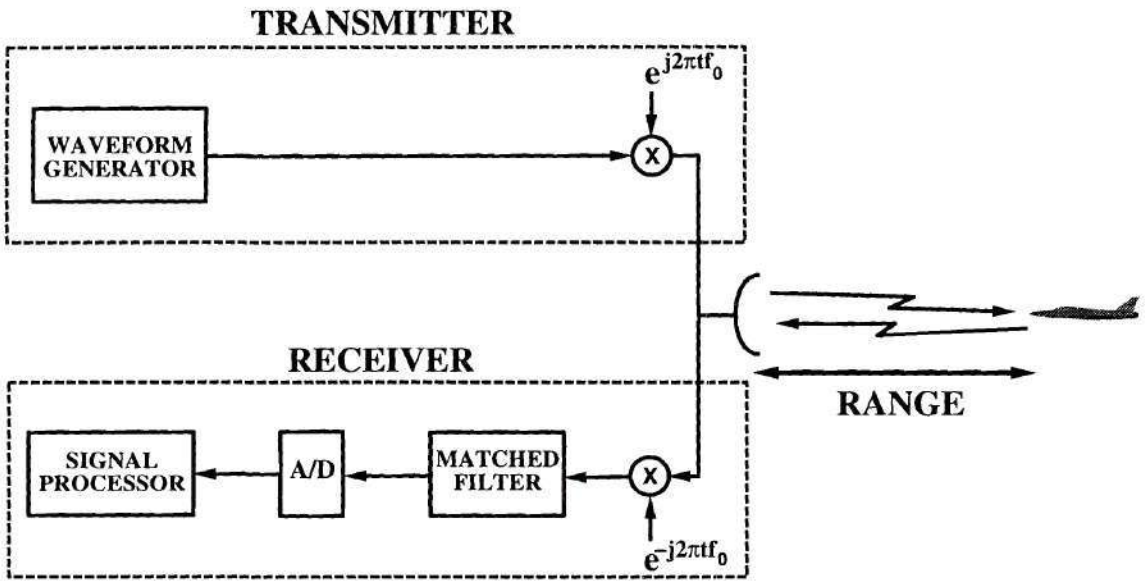

Figure 2.2: Radar receiver/transmitter block diagram.

The actual transmitted signal consists of a radar signal modulated by a carrier waveform as shown in Fig. 2.2. The carrier waveform usually consists of a complex sinusoid whose frequency is the operating frequency of the radar system. Assuming the radar signal propagates through the atmosphere at the speed of light in a vacuum ($c \cong 3 \times 10^8$ m/sec), the wavelength of the radar waveform is

$$\lambda = \frac{c}{f_0}\,, \tag{2.2}$$

where f_0 is the radar operating frequency. A large variety of radar signals are employed for different applications, the two most common of which are the linear frequency modulated (LFM) pulse and the continuous-wave (CW) pulse.

Once the propagating signal encounters a scattering object, it is reflected back to the receiver. The amount of reflected energy is related to the cross-sectional area of the object and its electro-magnetic properties. The effective radar cross-sectional (RCS) area is determined by the attenuation experienced on the reflection [51, 57]. The reflected signal travels back to the radar receiver along the same path as shown

in Fig. 2.2. Therefore, the time needed for the signal to propagate back and forth between the receiver and the scatterer determines their relative distance. This distance, known as the range, is given by

$$r = \frac{c\tau}{2} , \tag{2.3}$$

where τ is the time delay between transmission and reception of the signal.

Upon reception, the carrier waveform is removed via demodulation or down-conversion. In the case of an LFM pulse, the radar signal is then matched filtered in order to localize the signal energy to a specific range delay in an operation known as pulse compression [51, 57]. Matched filtering is performed by convolving the received signal with a time-reversed replica of the transmitted signal. In this way, the output of the matched filter approximates an impulse at the delay at which the beginning of the reflected pulse was received. A block diagram of the radar receiver is shown in Fig. 2.2. The output of the matched filter is sampled using an analog-to-digital (A/D) converter and passed on to the radar signal processor. Ideally, each scatterer is localized to an individual sample known as a range gate or cell. Of course, the desired target is not the only scatterer present in the environment. The radar receiver must contend with radar echos from undesired objects such as terrain, buildings, vegetation, and bodies of water. These returns are referred to as monostatic clutter which are discussed in Section 2.2.3. The suppression of monostatic clutter signals is addressed in Section 2.2.4.

2.1.2 Array Fundamentals

An antenna array refers to a number of antenna elements, also known as sensors, at distinct locations. By simultaneously broadcasting the same signal from each element with proper phase weighting, it is possible to transmit in a particular direction. The return signals impinging on the array are spatially sampled by the sensors. Likewise, the proper phase weighting and combination of the return signals from the array elements serves to emphasize a particular direction of interest. Arrays with the ability

to self-direct or steer themselves using phase weighting are called *phased arrays*. In the discussion that follows, we focus on the reception of radar signals by an array, having in mind that the same principles apply to the transmission of the signals.

The radar echo produced by a reflection propagates radially from the scatterer. However, the separation between the radar receiver and the scatterer is assumed to be large enough that the spherically propagating radar signal can be approximated by a plane wave [32]. As the radar signal traverses across the array of sensor elements, the signal waveform experiences a delay as it arrives at each successive sensor. This delay is related to the angle between the propagation path of the radar signal and the broadside of the array.

The layout of the array elements can have several configurations. A two-dimensional array with all of its elements in a common plane is known as a planar array. On the other hand, a one-dimensional array with all elements on one axis is referred to as a linear array. When the elements of the linear array are horizontally aligned, the inter-element delays reveal the azimuth angle of arrival. On the other hand, vertically aligned elements determine the elevation angle of the returns. The signal delay between two antenna elements is given by

$$\tau = \frac{d \sin \phi}{c} , \tag{2.4}$$

where d is the spacing between the two elements, ϕ is the angle at which the propagating wave arrives, and c is the speed of light. Throughout this thesis, a horizontally aligned, linear array with uniform inter-element spacing is assumed. Such an array is known as a *uniform linear array* (ULA). Fig. 2.3 shows a plane wave impinging on a ULA.

The sensor array signals are combined in such a way that emphasizes a particular direction of arrival in an operation known as *beamforming*. This operation can take place either prior to or after analog-to-digital (A/D) sampling. The resulting beamformers are then either analog or digital, respectively. In order to avoid spatial aliasing of the impinging signals that results in directional ambiguities, the maximum

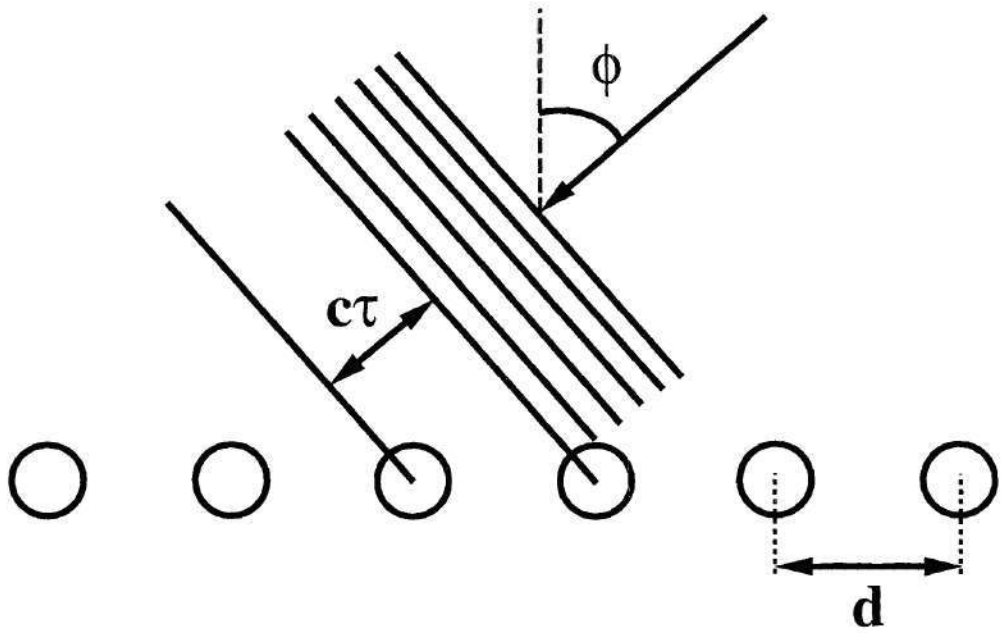

Figure 2.3: Propagating wave impinging on a uniform linear sensor array.

value of the array element spacing is limited to

$$d \leq \frac{\lambda}{2} \, . \tag{2.5}$$

For a ULA, the inter-element delay, τ, is constant between neighboring elements. Thus, the angle of the propagation path of the signal, ϕ, can be characterized by a spatial frequency

$$u = \frac{d}{\lambda} \sin \phi \, , \tag{2.6}$$

that gives the rate at which the signal waveform arrives at the different elements. Recall that the wavelength of the radar operating frequency is λ and is given by (2.2). The signals can be coherently combined by applying weights with proper phase weighting prior to summing the sensor array outputs. In this way, spatial filtering of the received array signals is performed, emphasizing returns from a certain azimuth angle. The spatial filter is implemented by applying an array weight vector to the

sampled outputs of the sensor array. A weight vector with elements of equal gain (magnitude) with phases to compensate for the delays between elements is known as a spatial steering vector [32]. In this case, the weight vector steers the array in a particular direction. The steering vector is a function of the spatial frequency u and is given by

$$\mathbf{a}(u) = \frac{1}{\sqrt{M}} \left[e^{-j2\pi \frac{M-1}{2} u} \ \cdots \ e^{-j2\pi \left(\frac{M-1}{2} - (m-1) \right) u} \ \cdots \ e^{j2\pi \frac{M-1}{2} u} \right]^T \tag{2.7}$$

for $m = 1, 2, \ldots, M$. The superscript $(\cdot)^T$ denotes the transpose operator and M is the number of elements in the ULA. Note that the spatial steering vector is phase-centered and normalized to have unit norm.

At this point, it is useful to define the terms mainbeam and sidelobes. Fig. 2.4 shows the response in decibels (dB) of a spatial steering vector at $\phi = 0°$ as a function of angle. Such a plot is often referred to as a beampattern. The mainbeam consists of the lobe surrounding the angle corresponding to the steering vector direction-of-look, i.e., $\phi = 0°$. Sidelobes are the other lobes in the remainder of the spectrum. Although the gain in the sidelobes is lower than within the mainbeam, strong signals may leak into the beamformer output through these sidelobes.

2.2 Surveillance Airborne Radar

The function of a surveillance airborne radar is to detect targets in severe interference environments. A target is any scattering object that the radar receiver is attempting to detect and is typically airborne, having a relative velocity with respect to the aircraft carrying the radar receiver. On the other hand, interference consists of any undesired radar returns that impede the ability of the receiver to detect targets. The different types of interferers must be filtered out of the radar returns in order to be able to extract targets.

The radar receiver consists of a ULA of sensor elements with inter-element spacing no more than half the wavelength of the radar operating frequency, f_0. The

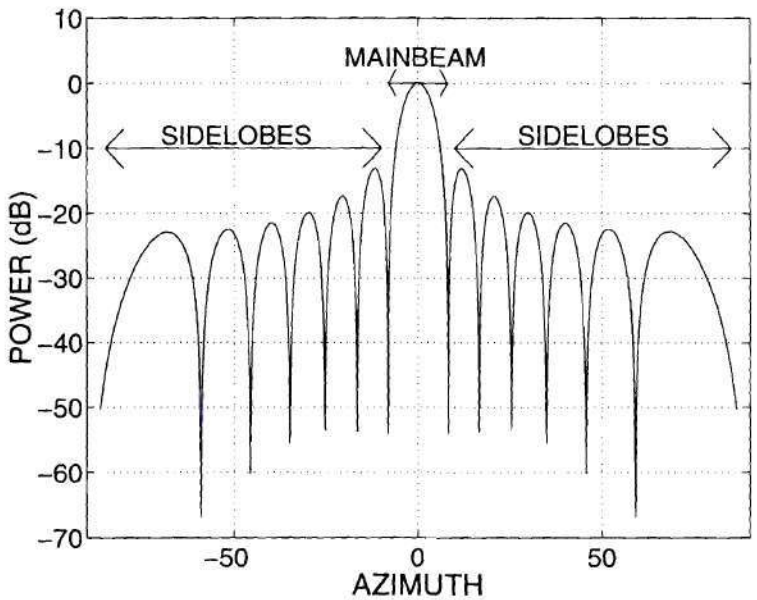

Figure 2.4: Beampattern (in decibels (dB)) for a spatial steering vector at azimuth $\phi = 0°$. The mainbeam and sidelobe regions are labeled.

ULA has M elements. A series or burst of pulses is transmitted at the PRF, f_p. Each pulse is sampled over a period of time known as the *pulse repetition interval* (PRI). The number of range samples collected in each PRI is N. The collection of sampled returns for a burst of pulses makes up a *coherent processing interval* (CPI). The number of pulses transmitted in a CPI is L. This data collection process is illustrated in Fig. 2.5. The assumption is made that the sampling frequency of the returns is greater than the bandwidth of the transmitted radar signal to prevent range aliasing [48].

Note that a scatterer with a velocity with respect to the radar receiver changes position from one pulse to the next. The relative movement of the scatterer results in a slight difference in propagation times of the radar waveform for consecutive pulses producing a phase shift between their respective returns. The imposition of phase shifts as a function of velocity is known as the Doppler effect [32, 41, 51, 57]. For the

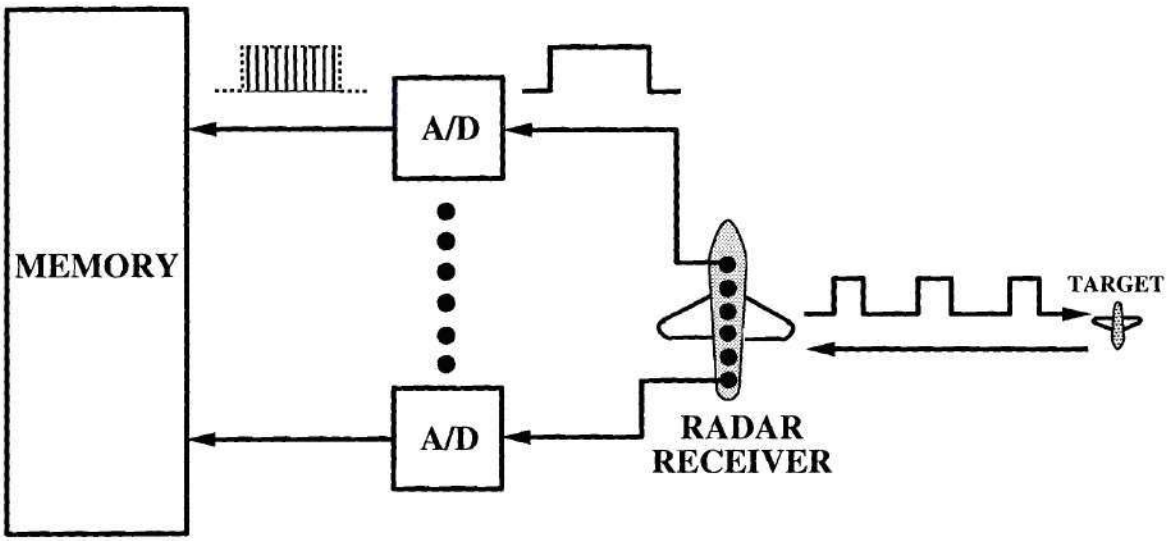

Figure 2.5: Surveillance airborne radar data collection with a coherent processing interval.

collection of L pulses, the phase shifts in the returns results in a Doppler frequency across the pulses that is related to the velocity of the scatterer v as

$$f = \frac{2v}{\lambda} . \tag{2.8}$$

The Doppler frequency is divided by the PRF, f_p, to obtain the normalized Doppler frequency

$$\bar{f} = \frac{f}{f_p} . \tag{2.9}$$

Similar to the spatial steering vector in (2.7), a unit-norm, phase-centered Doppler steering vector is defined as

$$\mathbf{b}\left(\bar{f}\right) = \frac{1}{\sqrt{L}}\left[e^{-j2\pi\frac{L-1}{2}\bar{f}} \ \cdots \ e^{-j2\pi\left(\frac{L-1}{2}-(l-1)\right)\bar{f}} \ \cdots \ e^{j2\pi\frac{L-1}{2}\bar{f}}\right]^T \tag{2.10}$$

for $l = 1, 2, \ldots, L$. The Doppler steering vector extracts scatterers with a certain Doppler frequency and, consequently, serves as a velocity filter for the set of collected pulses.

Data collection for a burst of pulses is performed in three dimensions: element, pulse or PRI, and range. The overall set of returns forms a 3-D data structure

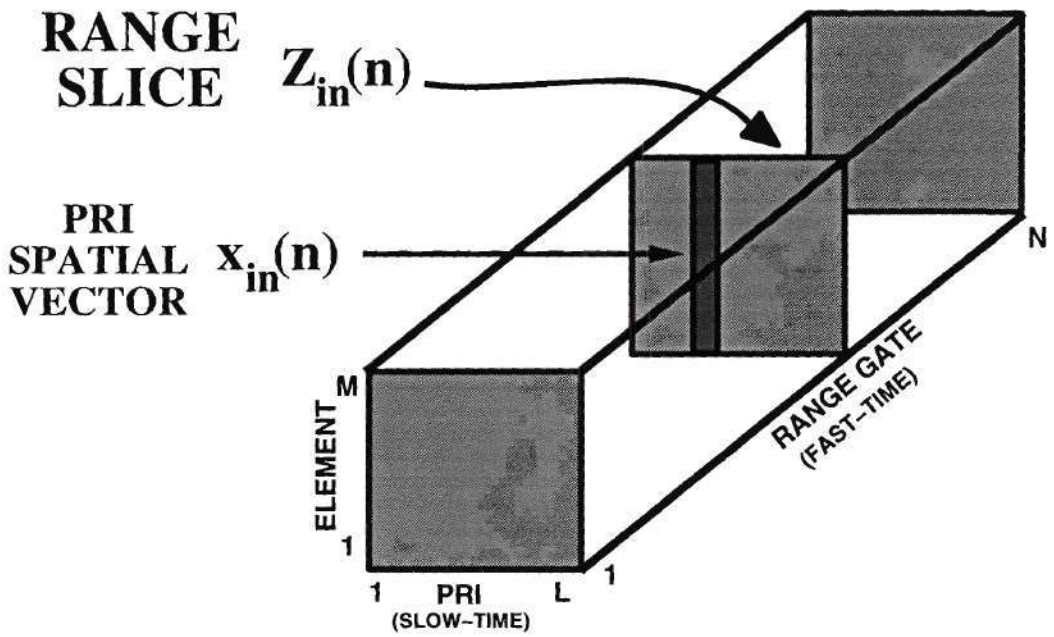

Figure 2.6: CPI data-cube with a range slice and a PRI spatial vector.

known as the CPI data-cube, shown in Fig. 2.6, whose dimensions are $M \times L \times N$. Since both PRI and range are time indices, the two are commonly differentiated as slow-time and fast-time, respectively. These two temporal dimensions have frequency domain counterparts of Doppler and instantaneous (range) frequency. On the other hand, the frequency domain of element space is beamspace. The notation throughout this thesis is to use vectors indexed by the range dimension. Therefore, as shown in Fig. 2.6, the spatial signal vector of array element signals for each PRI is

$$\mathbf{x_{in}}(n) \qquad \text{for } n = 1, 2, \ldots, N \ , \tag{2.11}$$

where the subscript "in" denotes the fact the PRI signal is to be input to the digital processor for target extraction and interference suppression.

Fig. 2.6 also shows the CPI data-cube with a range slice. The range slice is the collection of the data from the M sensor elements for all of the L PRIs at range gate

n. The slice is an $M \times L$ matrix function indexed by range

$$\mathbf{Z_{in}}(n) = \left[\mathbf{x}_{\mathbf{in}}^{(1)}(n) \;\; \mathbf{x}_{\mathbf{in}}^{(2)}(n) \;\; \cdots \;\; \mathbf{x}_{\mathbf{in}}^{(l)}(n) \;\; \cdots \;\; \mathbf{x}_{\mathbf{in}}^{(L)}(n)\right] . \tag{2.12}$$

The superscript $(\cdot)^{(l)}$ indicates the PRI number. Although it may be intuitive to look at a CPI as a collection of range slices, the data is processed by applying a set of weights to each range slice. For notational convenience, the application of the weights is performed using vector products. Therefore, the range slice must be converted to a space-time vector of element and PRI data. The $ML \times 1$ space-time vector is formed by concatenating the spatial vectors of the L PRIs in the following manner

$$\mathbf{z_{in}}(n) = \begin{bmatrix} \mathbf{x}_{\mathbf{in}}^{(1)}(n) \\ \vdots \\ \mathbf{x}_{\mathbf{in}}^{(l)}(n) \\ \vdots \\ \mathbf{x}_{\mathbf{in}}^{(L)}(n) \end{bmatrix} . \tag{2.13}$$

2.2.1 Target Signal

Recall that a target is any scattering object the surveillance airborne radar is attempting to detect. Targets can be either airborne or ground-based, both of which have a velocity relative to the airborne radar. Assuming pulse compression (matched filtering) has already been performed, the target signal is theoretically localized to one range gate or sample. Therefore, the ideal target signal is an impulse function in range

$$\alpha_t(n) = \sigma_t \delta(n - r_t) = \begin{cases} \sigma_t & \text{for } n = r_t \\ 0 & \text{for } n \neq r_t \end{cases} , \tag{2.14}$$

where r_t is the target range gate (integer) and σ_t is the complex target amplitude. Note that, in practice, the target is never only present in one range cell. Sampling effects lead to range sidelobes producing a certain amount of target spreading in range. The target power is usually measured with respect to the thermal noise floor.

The thermal noise in the sensor elements is temporally and spatially uncorrelated, and the noise floor is its space-time average power, σ_n^2. The target signal-to-noise ratio (SNR) is then

$$\text{SNR} = \frac{\sigma_t^2}{\sigma_n^2} \tag{2.15}$$

and is usually reported in decibels (dB).

A target at an azimuth angle, ϕ_t, and with a relative velocity, v_t, has a target spatial frequency

$$u_t = \frac{d}{\lambda} \sin \phi_t \ , \tag{2.16}$$

and a normalized Doppler frequency

$$\begin{aligned} \bar{f}_t &= \frac{f}{f_p} \\ &= \frac{2v_t}{\lambda f_p} \ . \end{aligned} \tag{2.17}$$

Recall that f_p is the PRF defined by (2.1). The spatial and Doppler steering vectors associated with the target are given by (2.7) and (2.10), respectively, with

$$\mathbf{a_t} = \mathbf{a}(u_t) \qquad \mathbf{b_t} = \mathbf{b}(\bar{f}_t) \ . \tag{2.18}$$

The target space-time steering vector is then given by the Kronecker product of $\mathbf{a_t}$ and $\mathbf{b_t}$

$$\begin{aligned} \mathbf{s_t} &= \mathbf{b}(\bar{f}_t) \otimes \mathbf{a}(u_t) \\ &= \mathbf{b_t} \otimes \mathbf{a_t} \ , \end{aligned} \tag{2.19}$$

where $\otimes$ denotes a Kronecker product [27].

The model of the PRI spatial target signal vector is found by projecting the target signal onto the array manifold with the target spatial steering vector $\mathbf{a_t}$

$$\mathbf{x_t}(n) = \alpha_t(n)\mathbf{a}(u_t) \ . \tag{2.20}$$

The CPI target space-time signal vector is obtained by projecting the target signal

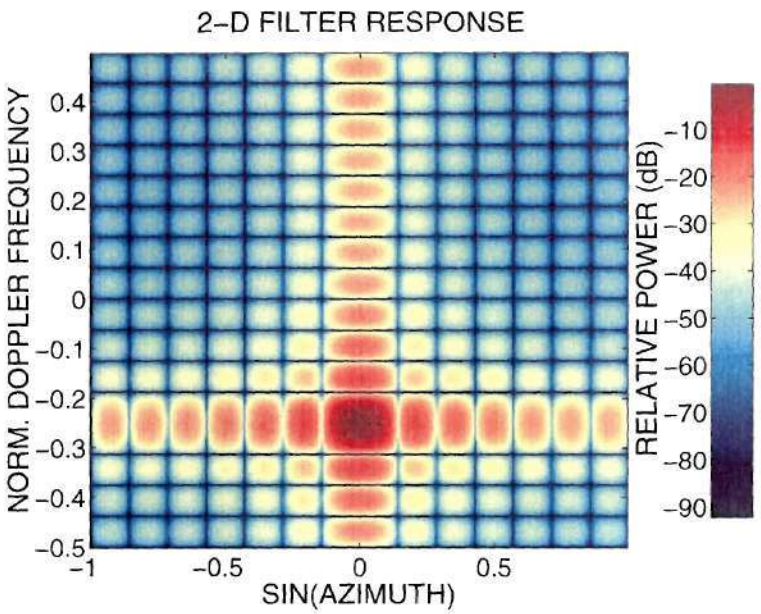

Figure 2.7: Target space-time conventional filter response.

onto the space-time steering vector $\mathbf{s_t} = \mathbf{s}(u_t, \bar{f}_t)$

$$\begin{aligned} \mathbf{z_t}(n) &= \alpha_t(n)\mathbf{s}(u_t, \bar{f}_t) \\ &= \alpha_t(n)\left(\mathbf{b}(\bar{f}_t) \otimes \mathbf{a}(u_t)\right) \\ &= \alpha_t(n)\left(\mathbf{b_t} \otimes \mathbf{a_t}\right) . \end{aligned} \tag{2.21}$$

In the absence of interference, the only thing the target has to contend with is the thermal noise in the antenna elements. In this case, the target can be extracted from the returns using a non-adaptive space-time filter. This filter is the target space-time steering vector $\mathbf{s_t}$ from (2.21). Fig. 2.7 shows the response of a space-time filter with $u_t = 0$, $\bar{f}_t = -0.25$. The filter has the gain on the target (0 dB) but also has high sidelobes (approximately 14 dB below the peak of the mainbeam) in both spatial and Doppler frequencies.

2.2.2 Jammer Signal

Typically, hostile jamming interference is produced by stand-off, barrage noise jammers. Other types of jammers are possible but are not considered. A barrage noise jammer broadcasts a strong broadband signal with a bandwidth substantially greater than the radar bandwidth. Therefore, the jammer signal is approximately uncorrelated from sample to sample as well as from PRI to PRI. In addition, the jamming energy is substantially greater than the target signal. The power of the jammer interference is also measured with respect to the thermal noise floor as the jammer-to-noise ratio (JNR), similar to (2.15) for the target SNR. Even though the conventional target space-time filter from Fig. 2.21 emphasizes the target at the desired azimuth angle and Doppler frequency, the jamming interference is so powerful that it leaks through the sidelobes of this space-time filter. This non-adaptive space-time filter can only achieve about 15 dB of suppression on the jammer signal in the spatial sidelobes which is not enough in the case of a strong jammer (e.g., JNR $>$ 50 dB). However, jammer interference can be mitigated using spatial nulling techniques.

Like the target, the jammer signal is spatially correlated, i.e., it has a distinct azimuth angle, and its waveform propagates from the jammer location to the radar receiver. Therefore, the PRI jammer signal at the radar receiver array is

$$\mathbf{x_j}(n) = \alpha_j(n)\mathbf{a_j} \ . \tag{2.22}$$

The jammer signal $\alpha_j(n)$ is modeled as a white, Gaussian signal with power σ_j^2. The term $\mathbf{a_j} = \mathbf{a}(u_j)$ is the jammer spatial steering vector from (2.7), determined by the jammer azimuth angle ϕ_j. By exploiting the spatial correlation in the jammer returns, jamming interference can be easily mitigated using spatially adaptive methods [11, 28].

Recall that the jamming signal is uncorrelated from PRI to PRI. Therefore, the CPI jammer space-time signal vector is

$$\mathbf{z_j}(n) = \boldsymbol{\alpha_j}(n) \otimes \mathbf{a_j} \tag{2.23}$$

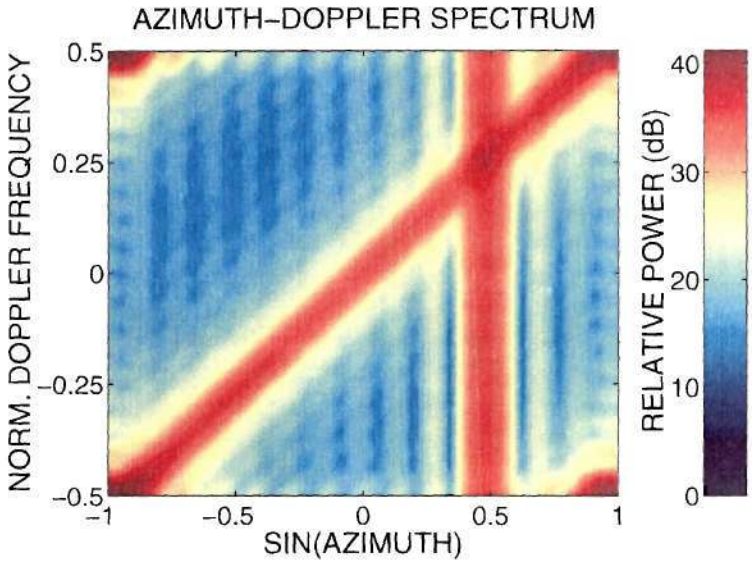

Figure 2.8: Azimuth-Doppler spectrum of combined direct-path jammer and monostatic clutter interference.

---

where $\boldsymbol{\alpha}_{\mathrm{j}}(n)$ is a white Gaussian noise vector and again $\otimes$ denotes a Kronecker product. Each component of the vector has a power of σ_j^2. Fig. 2.8 shows an azimuth-Doppler spectrum of returns containing a jammer at $\phi_j = 30°$ ($\sin\phi_j = 0.5$). Note that the power of the returns is spread across all Doppler frequencies, since the jammer signal lacks any significant temporal correlation.

2.2.3 Monostatic Clutter Signal

Monostatic clutter interference consists of the radar echos from stationary scatterers found in the environment surrounding the radar receiver that are of no tactical interest. For an airborne surveillance radar, the primary source of clutter is the reflected energy from the surface of the earth. Clutter interference is more complicated than jamming interference because it is not limited to one azimuth angle and tends to be non-stationary in range. The property of monostatic clutter that is exploited for mit-

igation purposes is the fact that scatterers are not moving. Therefore, the velocity of each scatterer relative to the airborne radar is a function of the aircraft velocity and the relative position of the scatterer. A simple method of cancelling ground clutter is moving target indicator (MTI) processing [41, 51, 57] that filters the returns based on Doppler frequency. However, MTI processing is not effective in removing clutter with the same relative velocity as the target returns.

More sophisticated cancellation methods seek to exploit both spatial and temporal characteristics of monostatic clutter. The clutter returns for each range sample are due to a ring on the earth's surface of equal distance from the radar and spanning all azimuth angles. However, the relative velocity of each clutter return can be shown to be a function of its azimuth angle [67]. Therefore, the normalized Doppler frequency of the clutter, $\bar{f}_c$, is related to its spatial frequency u_c by

$$\bar{f}_c = \left(\frac{2v_r}{f_p d}\right) u_c \ , \tag{2.24}$$

where v_r is the velocity of the radar receiver. Recall that f_p is the PRF and d is the inter-element spacing of the array. The energy of the clutter returns is restricted to a locus in the azimuth-Doppler spectrum consisting of a line with a slope of

$$\beta = \frac{2v_r}{f_p d} \ . \tag{2.25}$$

This line is commonly referred to as the clutter ridge. The assumption is made that the velocity vector of the aircraft is aligned with the array. Otherwise, misalignment causes aircraft "crab" which results in an elliptical expansion of the clutter ridge [67]. Fig. 2.8 shows an azimuth-Doppler spectrum of returns containing monostatic clutter with a clutter ridge slope of $\beta = 1$.

As with the target discussed in Section 2.2.1, the PRI clutter spatial signal vector for each azimuth angle ϕ_c (or spatial frequency u_c) is

$$\mathbf{x_c}(n, u_c) = \alpha_c(n, u_c)\mathbf{a}(u_c) \tag{2.26}$$

where $\alpha_c(n, u)$ is the clutter return signal as a function of range and spatial frequency (angle). Exploiting the relationship between the Doppler and spatial frequencies from

(2.24), the CPI clutter space-time signal vector for each azimuth angle is

$$\begin{aligned} \mathbf{z_c}(n,u) &= \alpha_c(n,u)\mathbf{s}(u,\bar{f}) \\ &= \alpha_c(n,u)\mathbf{s}(u,\beta u) \ , \end{aligned} \tag{2.27}$$

where $\mathbf{s}(u,\bar{f}) = \mathbf{b}(\bar{f}) \otimes \mathbf{a}(u)$ is the space-time steering vector. The overall PRI and CPI clutter signals are obtained by integrating over all angles (or spatial frequencies) [67].

2.2.4 Space-time Adaptive Processing

Space-time adaptive processing (STAP) combines spatial and temporal samples in an adaptive manner in order to emphasize certain characteristics. In the case of airborne surveillance radar, the STAP algorithm adaptively combines radar returns from the CPI data-cube. Target signals should be enhanced while interference sources are suppressed. The outputs of the space-time adaptive processor are passed on to the detector to determine the presence or absence of an actual target at a specific range gate. A block diagram of such a STAP architecture is shown in Fig. 2.9. The adaptive weight vector is found by applying a target constraint within a minimum variance processor [67]. The adaptive weights are

$$\mathbf{w} = \mathbf{R_z}^{-1}\mathbf{s}(u,\bar{f}) \tag{2.28}$$

where $\mathbf{s}(u,\bar{f})$ is the azimuth-Doppler steering vector constraint from (2.19). The covariance matrix $\mathbf{R_z}$ is

$$\mathbf{R_z} = \mathrm{E}\left\{\mathbf{z_{in}}(n)\mathbf{z_{in}}^H(n)\right\} \tag{2.29}$$

where the superscript $(\cdot)^H$ denotes the Hermitian or complex conjugate transpose operator. Recall that $\mathbf{z_{in}}(n)$ is the space-time data vector at range n of the CPI data-cube. The operator $\mathrm{E}\{\cdot\}$ denotes the mathematical expectation. The specific training strategy employed selects a subset of the CPI that does not contain the target range gate under consideration to estimate the adaptive weights [67]. The

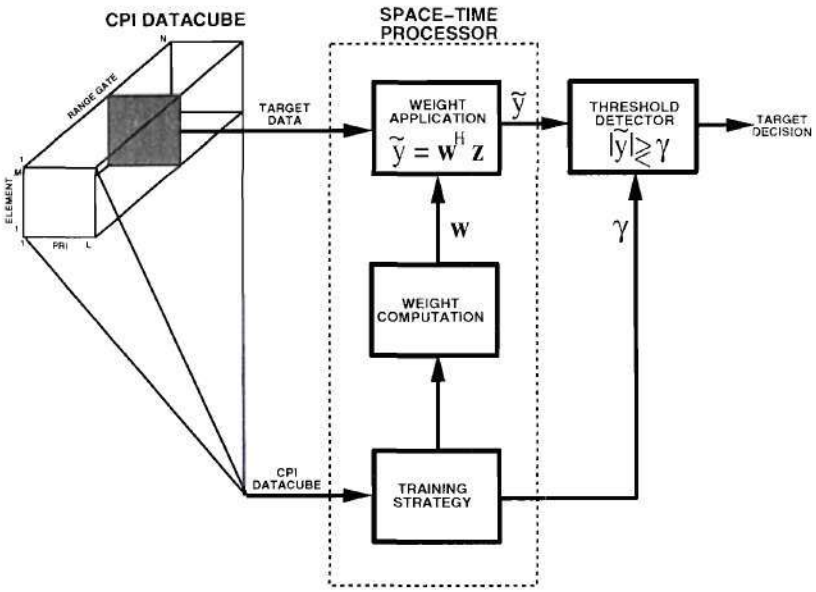

Figure 2.9: The architecture of a space-time adaptive processor along with the target detector.

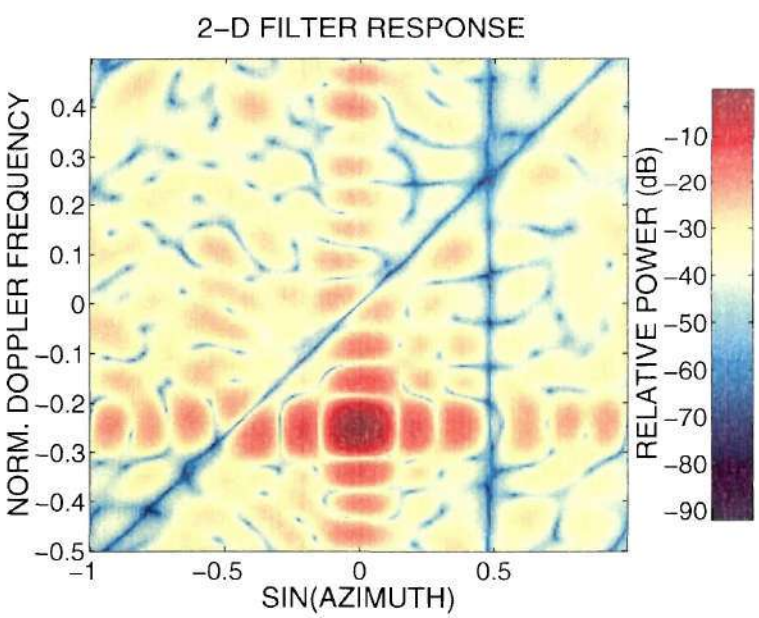

Figure 2.10: Space-time adaptive filter response. STAP filter for combined jammer and monostatic clutter interference from Fig. 2.8

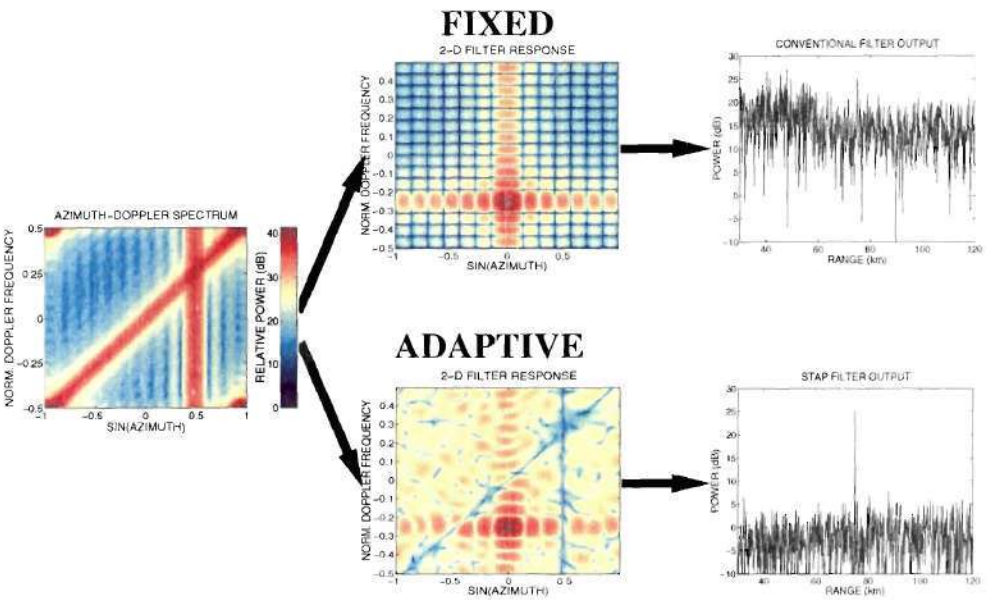

Figure 2.11: Example of space-time adaptive processing versus non-adaptive space-time processing. Injected target is present at 75 kilometers.

resulting minimum variance STAP filter forms nulls in the azimuth-Doppler spectrum at the locations of strong interference returns, while maintaining a gain on the target location. The 2-D frequency response of the STAP filter for the interference scenario from Fig. 2.8 is shown in Fig. 2.10. For this example, the assumed target azimuth angle is $\phi_t = 0°$ and the assumed normalized Doppler frequency is $\bar{f}_t = -0.25$. Fig. 2.11 illustrates the performance gains associated with STAP over conventional non-adaptive processing. A target is injected at 75 kilometers in the same interference scenario. The STAP filter is able to reduce the interference to the thermal noise floor and easily extract the 25 dB target. On the other hand, the non-adaptive space-time filter is unable to effectively remove the interference. Since the high sidelobe levels of the filter coincide with regions of strong interference from both the jammer and the clutter, a large amount of interference energy is still present in the output of the 2-D filter.

2.3 Terrain Scattered Interference

Terrain scattered interference (TSI) is produced by the multipath reflections of a stand-off barrage noise jammer. The mitigation of TSI presents a unique multi-dimensional adaptive filtering problem that contains significant coupling between space and time. Exploitation of the TSI characteristics aid in the development of efficient cancellation methods. This section contains background material on TSI as well as the currently employed method for TSI mitigation: the single-reference beam (SRB) canceler.

2.3.1 TSI Signal Model

Terrain scattered interference (TSI) is produced by either intentional or incidental jammer multipath [17]. The jammer signal is reflected by various surface scatterers, whose reflections are incident on the radar receiver from a large number of azimuth angles, often throughout the mainbeam. The jammer signal is assumed to be an uncorrelated (white), Gaussian noise signal, so that TSI returns are uncorrelated from one PRI to the next. Fig. 2.12 depicts a typical TSI scenario. TSI presents a particularly strenuous and unique problem to the airborne radar system. Since mainbeam interference is spatially correlated with the target, spatial nulling is not an option for mitigation purposes. Therefore, cancellation methods must seek to exploit the temporal correlation present within the TSI. Consider that each reflection of the original jammer signal traverses a different path length from the jammer to the scatterer to the radar receiver, as shown in Fig. 2.12. Consequently, the mainbeam TSI signal is made up of delayed replicas of the original continuous-time jammer signal. The TSI signal for each azimuth angle ϕ $(-\pi \leq \phi < \pi)$ is

$$x_{tsi}(t,u) = \int_0^{T_{tsi}} h(\tau,u)\, x_j(t-\tau)d\tau \tag{2.30}$$

where u is the spatial frequency related to azimuth by (2.6). T_{tsi} is the maximum delay in the TSI returns and is often referred to as the temporal or range extent of the TSI. Recall that the jammer source signal, $x_j(t)$, is assumed to be white, Gaussian noise. The function $h(t, \phi)$ is the complex weighting of the TSI at each delay t and azimuth angle ϕ. This TSI weighting function incorporates both the antenna pattern of the jammer transmitter and the reflection characteristics of the terrain that produces the scattering [47]. In general, this function is unknown to the radar receiver. The spatial TSI signal seen by the ULA of the radar receiver, $\mathbf{x_{tsi}}(t)$, is the result of the TSI signals from each azimuth angle projected onto the array manifold using the phase-centered spatial steering vector $\mathbf{a}(\cdot)$ from (2.7)

$$\mathbf{x_{tsi}}(t) = \int_{-\pi}^{\pi} x_{tsi}(t, u)\, \mathbf{a}(u) du \; . \tag{2.31}$$

The discrete-time TSI spatial signal vector $\mathbf{x_{tsi}}(n)$ for one PRI is obtained by sampling its continuous-time counterpart from (2.31). Recall that a total of N samples are collected for each PRI. The TSI space-time signal for an entire CPI is found by concatenating the TSI signals for the individual PRIs

$$\mathbf{z_{tsi}}(n) = \begin{bmatrix} \mathbf{x}_{\mathbf{tsi}}^{(1)}(n) \\ \vdots \\ \mathbf{x}_{\mathbf{tsi}}^{(l)}(n) \\ \vdots \\ \mathbf{x}_{\mathbf{tsi}}^{(L)}(n) \end{bmatrix} \tag{2.32}$$

where $\mathbf{x}_{\mathbf{tsi}}^{(l)}(n)$ is the TSI signal of the lth PRI.

In the case of airborne jammers and/or radar receivers, a relative motion exists with respect to each patch of terrain producing the jammer multipath reflections. The result is the modulation by a relative Doppler frequency for each scatterer contributing to the TSI signal. The frequency varies as a function of geometry. Therefore, the overall TSI signal contains many Doppler components due to the various scatterers. Each Doppler component produces a copy of the original jammer signal modulated

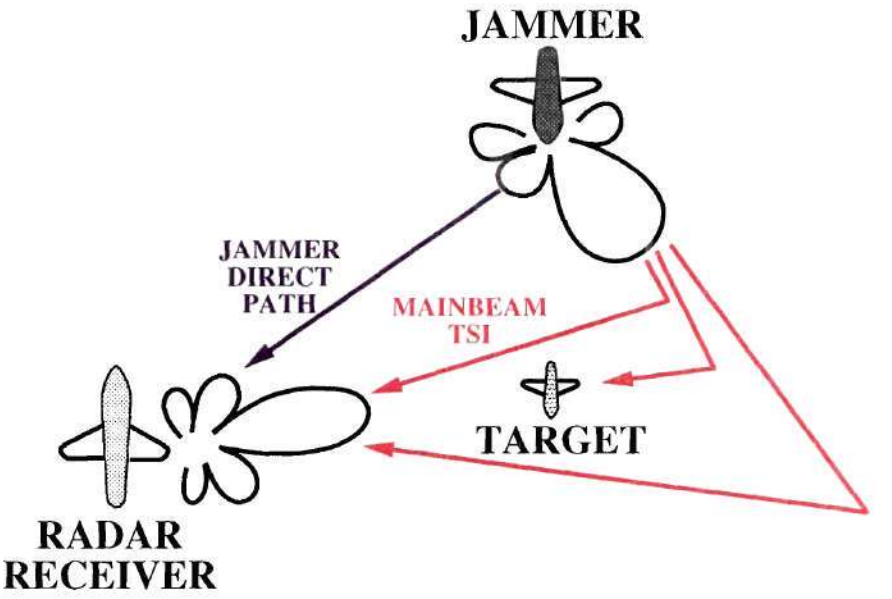

Figure 2.12: Scenario with mainbeam and sidelobe terrain scattered interference.

by a different Doppler frequency. The TSI signal contains many of these Doppler components further complicating its mitigation. Any cancellation method must compensate for the Doppler frequencies in the adaptive prediction of the TSI signal in order to independently weight each Doppler frequency component.

An alternate view of TSI is that of a white, Gaussian noise input (jammer signal) passed through a linear system (terrain reflections). The successful canceler is able to predict the TSI signal by acquiring the input signal (i.e., the jammer signal), either via the direct-path signal or by deconvolving the sidelobe TSI signals. Then, the linear system that models the terrain reflections is approximated with a convolution operation. For each time instant, the mainbeam TSI signal has contributions from the jammer waveform $x_j(t)$ over the interval depicted in Fig. 2.13. The delay, T_{tsi}, corresponds to the maximum path delay in (2.30) which is the temporal or range extent of the TSI. Complete TSI suppression requires the canceler to observe the entire interval of the jammer waveform that contributed to the interference.

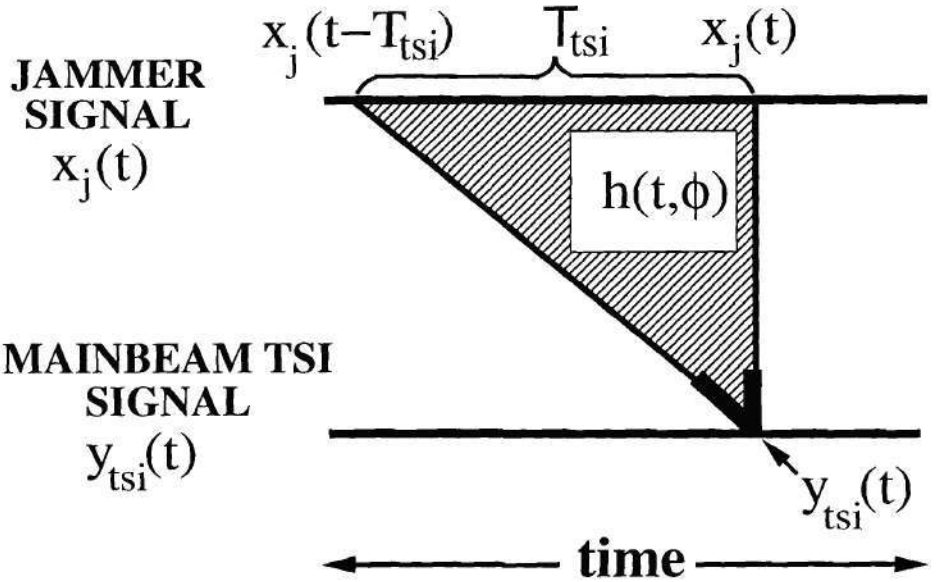

Figure 2.13: Mainbeam TSI time-line.

2.3.2 The Single-reference Beam Canceler

The single-reference beam (SRB) canceler is the most widely used TSI mitigation method [5, 21, 22]. This technique uses a reference beam, typically directed at the jammer, to predict and subsequently remove the TSI present in the mainbeam. A block diagram of the SRB canceler is shown in Fig. 2.14. The array snapshots of each PRI, $\mathbf{x_{in}}(n)$, are spatially filtered in both the desired target and reference beam directions, corresponding to azimuth angles ϕ_t and ϕ_r, respectively. Recall that n is the snapshot index corresponding to range. The spatial filters employed for this task are the phase-centered steering vectors from (2.7) given by

$$\mathbf{a}(u) = \frac{1}{\sqrt{M}} \left[e^{-j2\pi \frac{M-1}{2} u} \ \cdots \ e^{-j2\pi \left(\frac{M-1}{2} - (m-1) \right) u} \ \cdots \ e^{j2\pi \frac{M-1}{2} u} \right]^T \tag{2.33}$$

for $m = 1, 2, \ldots, M$. Recall that M is the number of elements in the ULA and u is the spatial frequency corresponding to azimuth angle ϕ and is given by

$$u = \frac{d}{\lambda} \sin \phi \ . \tag{2.34}$$

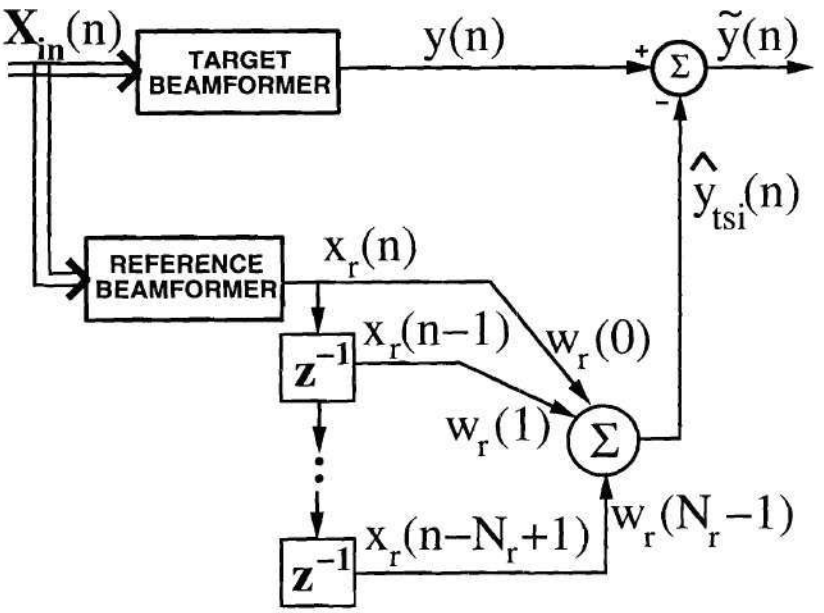

Figure 2.14: Single-reference beam TSI canceler.

The inter-element spacing and wavelength of the radar operating frequency are d and λ, respectively. Note that spatial filters with low sidelobe levels can also be employed through the use of a tapered window [67]. However, the cost incurred for the low sidelobes is an increase in the width of the mainbeam, resulting in diminished resolution and an increase in mainbeam interference for the TSI scenario. The choice of the spatial filters is therefore a trade-off between sidelobe performance and resolution. In our case, the spatial filters used are the steering vectors, given by (2.33), to avoid the leakage of excess TSI into the mainbeam.

The mainbeam signal is obtained by applying the target spatial steering vector $\mathbf{a_t} = \mathbf{a}(u_t)$ to the PRI signal from (2.11)

$$\begin{aligned} y(n) &= \mathbf{a}_t^H \mathbf{x_{in}}(n) \\ &= \mathbf{a}_t^H \mathbf{x_t}(n) + \mathbf{a}_t^H \mathbf{x_{tsi}}(n) + \mathbf{a}_t^H \mathbf{x_n}(n) \\ &= y_t(n) + y_{tsi}(n) + y_n(n) \end{aligned} \tag{2.35}$$

where $y_t(n)$, $y_{tsi}(n)$, and $y_n(n)$ are the target, TSI, and thermal noise components of the mainbeam signal, respectively. The assumption has been made that monostatic clutter returns are not present. The goal of the canceler is to filter the mainbeam signal $y(n)$ in order to reduce the contribution of the TSI to below the thermal noise floor. The reference beam signal is obtained by applying the reference beam spatial steering vector $\mathbf{a_r} = \mathbf{a}(u_r)$ to the PRI signal

$$x_r(n) = \mathbf{a_r}^H \mathbf{x_{in}}(n) \ . \tag{2.36}$$

Since the reference beam signal provides a look at the jammer signal $x_j(t)$, the single source of the mainbeam interference, it can be used to estimate the mainbeam TSI signal $y_{tsi}(n)$. Recall that the TSI signal is produced by weighted delayed replicas of $x_j(t)$ from the various terrain reflections. Therefore, the TSI present in each time sample has contributions from an interval on the original jammer waveform as shown in Fig. 2.13. As stated earlier, the TSI signal is the output of an unknown linear system, corresponding to the terrain reflections, whose input is the jammer signal. The task of the canceler is to acquire the source signal and attempt to find the coefficients of the linear system that produced the mainbeam interference. The direct-path reference beam signal provides an estimate of the jammer signal that produced the TSI. When using the direct-path signal, the canceler must have a temporal window that spans the contributing interval of the jammer signal. The samples used in the canceler are contained in the temporal window, whose span T_r must be greater than the range or temporal extent of the mainbeam TSI, i.e., $T_r > T_{tsi}$. The number of samples in the temporal window is

$$N_r = T_r \cdot F_s \tag{2.37}$$

where F_s is the radar sampling frequency of the A/D converters. From a systems point of view, the approximation of the TSI-producing linear system, i.e., the canceler, must have the same temporal length as the actual TSI-producing system.

The SRB canceler estimates the mainbeam TSI, $y_{tsi}(n)$, from the direct-path reference-beam signal $x_r(n)$. First, the signal prediction vector is formed with the components to be used for estimating the mainbeam TSI, i.e., the reference beam signal at the various tap delays of the SRB canceler

$$\mathbf{x_r}(n) = \begin{bmatrix} x_r(n) \\ x_r(n-1) \\ \cdots \\ x_r(n-N_r+1) \end{bmatrix}^{*} . \tag{2.38}$$

The $N_r \times 1$ adaptive weight vector for the SRB canceler ,$\mathbf{w_r}$, is found from the Wiener-Hopf equation by invoking the minimum mean-square error (MMSE) criterion [48]

$$\mathbf{w_r} = \mathbf{R_r^{-1}}\,\mathbf{r_r} \ . \tag{2.39}$$

The covariance matrix of the reference beam signal prediction vector is given by

$$\mathbf{R_r} = \mathrm{E}\left\{\mathbf{x_r}(n)\mathbf{x_r}^H(n)\right\} \tag{2.40}$$

where $(\cdot)^H$ denotes the Hermitian or complex conjugate transpose operation. The cross-covariance vector between the reference beam signal prediction vector and the mainbeam signal is

$$\mathbf{r_r} = \mathrm{E}\left\{\mathbf{x_r}(n)y^*(n)\right\} \ . \tag{2.41}$$

$\mathrm{E}\{\cdot\}$ is the mathematical expectation operator [53] and * denotes complex conjugation. The estimate of the mainbeam TSI is

$$\begin{aligned} \hat{y}_{tsi}(n) &= \mathbf{w_r}^H \mathbf{x_r}(n) \\ &= \sum_{k=0}^{N_r-1} w_r^*(k)\, x_r(n-k) \end{aligned} \tag{2.42}$$

and the output of the canceler is

$$\tilde{y}(n) = y(n) - \hat{y}_{tsi}(n) \ . \tag{2.43}$$

In practice, the covariance matrix, $\mathbf{R_r}$, and cross-covariance vector, $\mathbf{r_r}$, are unknown but can be estimated from the collected data returns. Substitution of the

maximum-likelihood (ML) estimates of the covariance matrix and cross-covariance vector into the Wiener-Hopf equation (2.39) results in a technique known as the sample matrix inversion (SMI) method [54]. Dynamic, adaptive methods, such as the least mean-squares (LMS) algorithm [68], are not usually considered since the amount of time required for convergence to the optimal weight vector is, in general, unacceptable. To find the SMI weights, first compute the sample covariance matrix

$$\hat{\mathbf{R}}_{\mathbf{r}} = \frac{1}{N_t} \sum_{k=1}^{N_t} \mathbf{x}_{\mathbf{r}}(n_t(k)) \mathbf{x}_{\mathbf{r}}^H(n_t(k)) \tag{2.44}$$

and the sample cross-covariance vector

$$\hat{\mathbf{r}}_{\mathbf{r}} = \frac{1}{N_t} \sum_{k=1}^{N_t} \mathbf{x}_{\mathbf{r}}(n_t(k)) y^*(n_t(k)) \ . \tag{2.45}$$

The number of training samples is N_t and $n_t(k)$ are the PRI snapshot indices that define the training interval. The training interval is a subset of the entire PRI of range samples ($n = 1, 2, \ldots, N$). In the presence of monostatic clutter, a dedicated training interval from a "clutter-free" region of the PRI, typically at far-field ranges, should be reserved for TSI weight training [22]. Otherwise, clutter returns may degrade TSI cancellation performance. Substituting (2.44) and (2.45) into the Wiener-Hopf equation (2.39) yields the SMI adaptive weight vector

$$\hat{\mathbf{w}}_{\mathbf{r}} = \hat{\mathbf{R}}_{\mathbf{r}}^{-1} \hat{\mathbf{r}}_{\mathbf{r}} \ . \tag{2.46}$$

The SMI weight vector should be computed from the same PRI to which it is applied because of the non-stationarity of TSI from one PRI to the next. The assumption of a stationary environment over an entire PRI is generally made. Should this not hold, smaller processing blocks must be used within a PRI.

As mentioned previously, a major shortcoming of the SRB canceler is the requirement of a large temporal window for acceptable performance. At the start of each PRI, the canceler is empty and fills up with samples, one at a time. The limited number of samples available to the canceler at the beginning of each PRI leads to

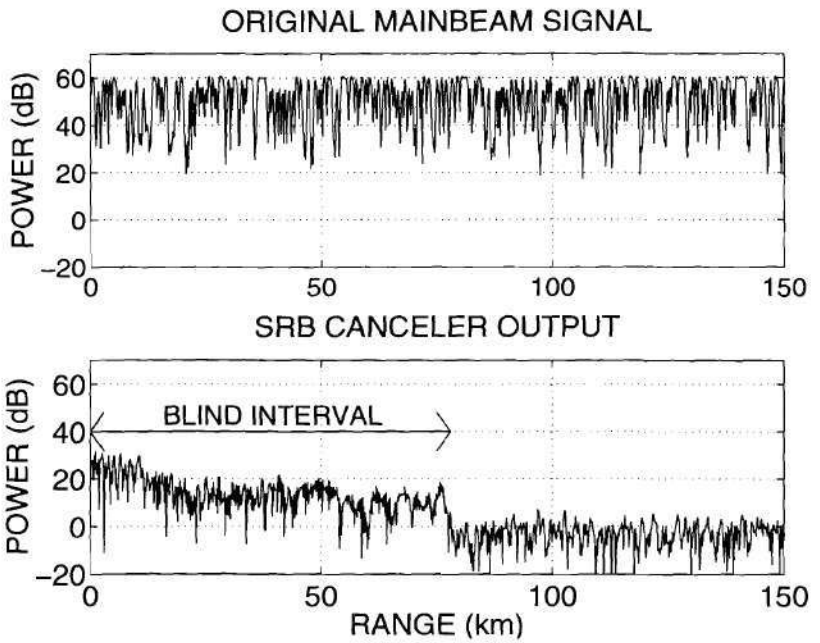

Figure 2.15: Blind interval of the SRB canceler.

poor cancellation performance until the canceler is full. This degradation in cancellation performance leads to a loss in target detection while the receiver is essentially "blind." Therefore, the interval over which the canceler fills up with samples is commonly referred to as the blind interval. The effects of the blind interval are shown in Fig. 2.15, where the top signal is the mainbeam TSI prior to cancellation and the bottom signal is the output of the SRB canceler using 520 temporal taps or degrees of freedom. Note that although the TSI has been cancelled to the noise floor (0 dB), full suppression does not occur until after the canceler has accumulated enough reference beam samples to form the MMSE estimate of the interference. In the case of the canceler in Fig. 2.15, the number of samples needed for the TSI estimate is 520 samples corresponding to 78 km in range. Such a large blind interval is in general unacceptable. Note that diagonal loading of the covariance matrix [12] has been shown to alleviate the effects of the blind interval [22].

The SRB canceler has a few other shortcomings. First, a priori knowledge of the jammer location is required, so that an additional direction-of-arrival estimate is necessary before TSI cancellation. In addition, airborne jammers make it necessary for the SRB canceler to continually update the jammer location estimate in order to maintain a proper direct-path reference beam. Consequently, the SRB canceler is vulnerable to a rapidly changing interference environment. When additional jamming sources are in use, multiple reference beams must be used, all with the same shortcomings of the SRB canceler. The last consideration is the Doppler frequency shift in the mainbeam TSI imposed by the motion of an airborne TSI-producing jammer. The simple SRB canceler is not able to accurately estimate the interference present at the various Doppler frequencies simultaneously and Doppler compensation channels must be employed [21, 22]. A SRB canceler with Doppler compensation channels is shown in Fig. 2.16. However, the cost of additional Doppler compensation channels is a drastic increase in adaptive degrees of freedom. Also, the Doppler frequency content of the TSI is not known a priori and must be estimated prior to TSI mitigation.

2.4 Summary

This chapter has covered some of the fundamental concepts of radar systems and array processing. Again, see [41, 51, 57, 58] and [15, 30, 32, 48] for some radar and array processing references, respectively. In addition, a description of TSI was given along with the currently used mitigation method, the SRB canceler. The proposed TSI mitigation method covered in Chapter 3 will be compared to the SRB canceler.

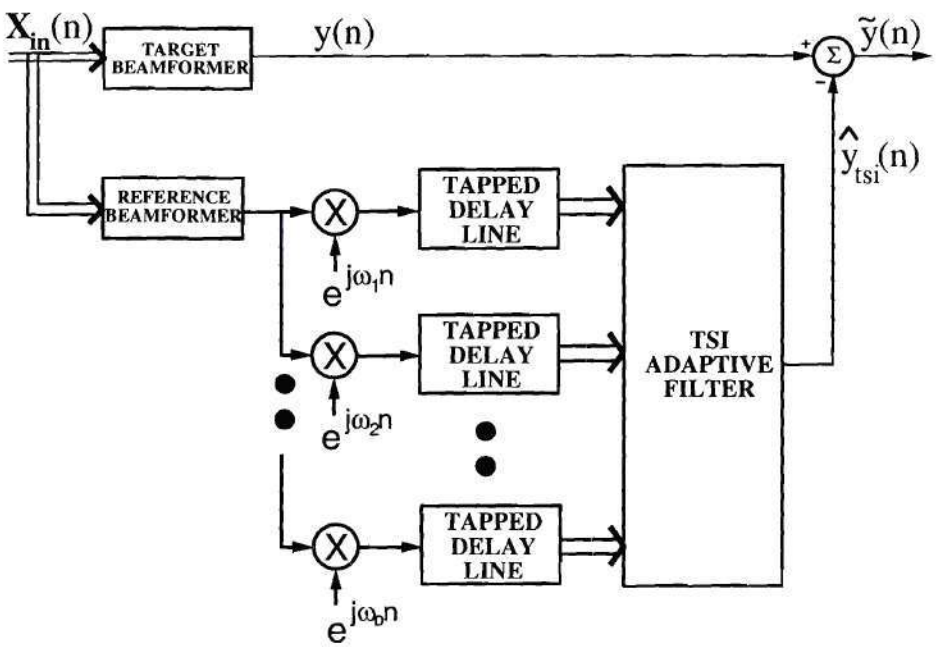

Figure 2.16: SRB canceler with Doppler compensation channels.

CHAPTER 3

Beamspace TSI Mitigation

The TSI signal model and the most commonly used mitigation technique, the single-reference beam (SRB) canceler, have been discussed in Chapter 2. In addition, the specific shortcomings of the SRB canceler have been outlined in Section 2.3.2. In this chapter we introduce a new mitigation method based on a beamspace transform that fully exploits all of the spatial degrees of freedom available to improve cancellation performance. Namely, the new method is shown to have the following important advantages over the SRB canceler:

- effective cancellation of TSI produced by airborne jammers without the requirement of Doppler compensation channels,
- no requirement of a priori knowledge of the jammer location,
- significant reduction of the blind interval of the canceler,
- prevention of potential signal cancellation.

The chapter begins with a discussion of the trade-off between spatial and temporal degrees of freedom. Next, the new *beamspace TSI canceler* is derived followed by an analysis of its cancellation performance. The chapter concludes with a performance comparison between the beamspace canceler and the SRB canceler using experimental data collected as part of the DARPA/Navy Mountaintop program [40, 61] followed by a discussion of robustness issues related to TSI mitigation.

3.1 Spatial versus Temporal Information

Recall that each sample of TSI is produced by an interval on the waveform transmitted by the jammer. In the absence of significant temporal correlation within the waveform, e.g., a broadband jammer, effective mitigation requires the observation of the entire interval on the jammer waveform contributing to the interference. The interval that produced the TSI, i.e., the jammer signal between $x_j(t)$ and $x_j(t-T)$, is depicted in Fig. 2.13. Once the cancellation method has acquired the source waveform, it must estimate the TSI using covariance statistics. In the case of the SRB canceler, an attempt is made to acquire the jammer source signal through the direct-path to the receiver. Therefore, the temporal window of the canceler must be as large as the interval on the source waveform that produced the TSI. Note that the rank of the mainbeam interference, the number of independent contributing terms, is equal to the number of samples from this interval.

However, TSI is not only received in the assumed target direction mainbeam but is typically also found in the sidelobes of the mainbeam as illustrated in Fig. 3.1. These additional sidelobe TSI signals can be used to estimate the mainbeam interference [19, 36, 37]. Fig. 3.2 shows a timing diagram of the original jammer signal that is the source of both the mainbeam and the two sidelobe TSI signals. Each of the TSI signals, though due to different terrain reflections, is produced by a similar interval on the jammer waveform. Therefore, the two sidelobe TSI signals are cross-correlated with their mainbeam counterpart. As opposed to the direct-path jammer signal whose auto-correlation is approximately white, each sample of the sidelobe TSI signal is produced by many samples of the jammer source. Each sidelobe signal has significant correlation with, and therefore information about, an interval of the jammer waveform. If enough sidelobe TSI signals are collected by the radar receiver, an accurate estimate of the jammer waveform can be found by deconvolving the various TSI signals from the spatial sidelobes of the mainbeam. Therefore, the additional spatial information translates directly into temporal information that can be used for

cancellation purposes.

A result of the use of this additional spatial information is a drastic reduction in the size of the temporal window required for cancellation. Whereas the SRB canceler used a tapped delay line to produce the various delays of the jammer source signal, the use of sidelobe TSI gives the canceler access to the source at various delays. In a sense, the terrain reflections act as an extended tapped delay line with each reflection inducing a different delay on the jammer source waveform. The TSI signals in the spatial sidelobes are a result of the same jammer source with different reflection coefficients. In order to incorporate the sidelobe TSI into the estimate of the mainbeam TSI, the canceler must simultaneously perform a deconvolution operation to recover the jammer source from the sidelobe TSI and convolve the estimated source with the model of the terrain reflections producing the mainbeam interference. Both operations are inherent in the adaptive predictor. However, since the sidelobe TSI provides access to the source waveform at many delays, short and long, the incorporation of spatial degrees of freedom reduces the number of temporal delays necessary. This trade-off between spatial and temporal degrees of freedom results in a drastic reduction in the size of the temporal window of the canceler. Another important characteristic of the TSI received in the sidelobes of the array is that it is modulated by various Doppler shifts depending on the geometry associated with the propagation of the signal. The TSI at different Doppler frequencies proves to be very useful for the mitigation of TSI produced by an airborne jammer, which can contain many Doppler components.

3.2 A Beamspace TSI Canceler

Recall that TSI mitigation is performed by adaptively processing the returns from each PRI separately. The first concern when designing a canceler is to ensure that the MMSE predictor does not cancel any portion of the target signal. Consider the gen-

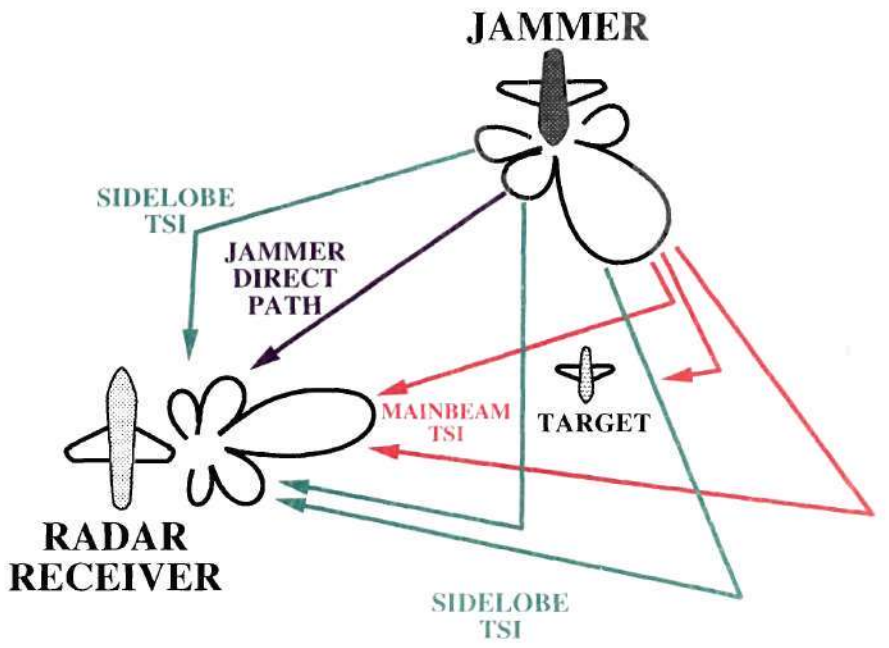

Figure 3.1: TSI scenario with both mainbeam and sidelobe interference.

eralized sidelobe canceler (GSC) structure [28] shown in Fig. 3.3. The upper branch consists of the mainbeam signal $y(n)$ obtained by non-adaptive, spatial filtering of the array input signal from one PRI

$$y(n) = \mathbf{a}_\mathbf{t}^H \mathbf{x}_\mathbf{in}(n) \ . \tag{3.1}$$

The spatial filter $\mathbf{a_t} = \mathbf{a}(u_t)$ is the phase-centered spatial steering vector from (2.7) at the spatial frequency of the target

$$u_t = \frac{d}{\lambda} \sin \phi_t \ , \tag{3.2}$$

where ϕ_t is the target azimuth angle. The lower branch of the GSC computes an estimate, $\hat{y}_{tsi}(n)$, of the TSI present in the mainbeam signal $y(n)$. To prevent target signal cancellation, the lower branch of the GSC has an $M \times (M-1)$ spatial blocking matrix $\mathbf{B_s}$ that is orthogonal to the mainbeam spatial filter

$$\mathbf{B}_\mathbf{s}^H \mathbf{a}_\mathbf{t} = 0 \ . \tag{3.3}$$

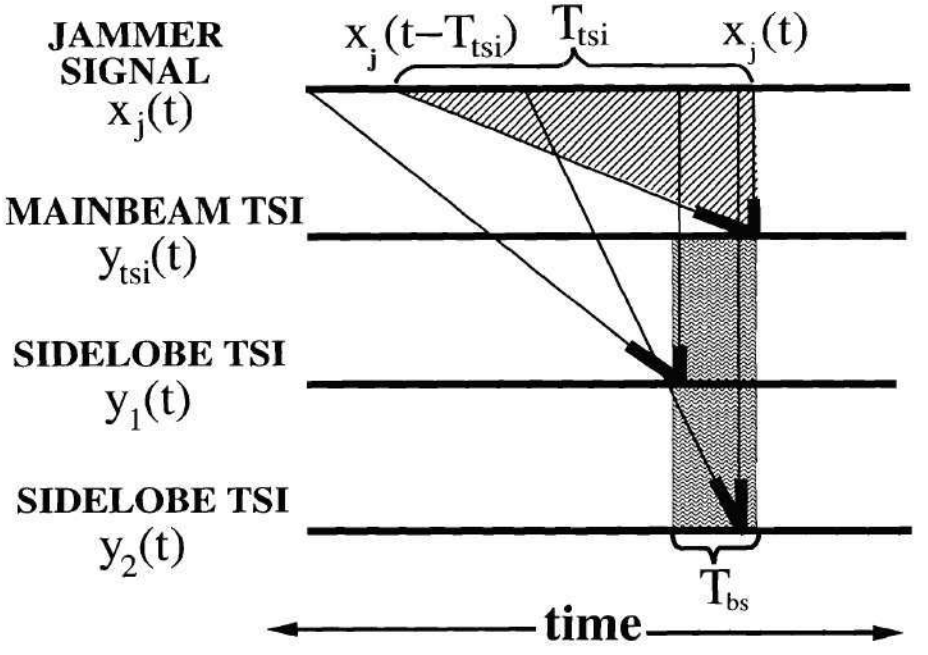

Figure 3.2: Mainbeam and sidelobe TSI time-lines.

Therefore, target returns cannot leak into the interference predictor in the lower branch. Note that with the SRB canceler there is no guarantee of orthogonality between the mainbeam and reference beam spatial filters.

The design of the blocking matrix requires its columns to span the null-space of $\mathbf{a_t}$, allowing for an infinite number of choices for $\mathbf{B_s}$. However, steering vectors at spatial frequencies separated from the target spatial frequency by integer multiples of $\frac{1}{M}$ are guaranteed to be orthogonal to the target steering vector, i.e.,

$$\mathbf{a}^H(u_m)\ \mathbf{a_t} = 0 \tag{3.4}$$

for spatial frequencies

$$u_m = u_t + \frac{1}{M}\,,\ \cdots\ ,\ u_t + \frac{m-1}{M}\,,\ \cdots\ ,\ u_t + \frac{M-1}{M} \tag{3.5}$$

for $m = 2, 3, \ldots, M$. Note that for notational convenience, the subscript 1 has been reserved for the spatial frequency of the target signal, $u_1 = u_t$, and its corresponding

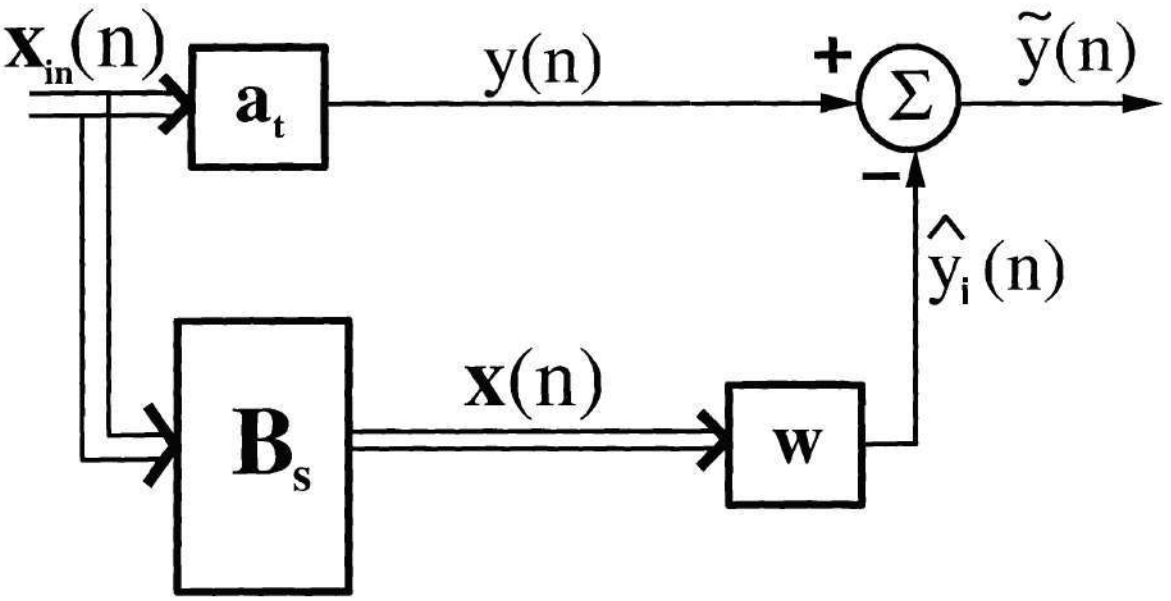

Figure 3.3: Generalized sidelobe canceler (GSC).

steering vector $\mathbf{a_1} = \mathbf{a_t}$. Therefore, a blocking matrix orthogonal to the target steering vector is found by filling its columns with these $(M-1)$ steering vectors

$$\mathbf{B_s} = [\mathbf{a}(u_2) \ \cdots \ \mathbf{a}(u_m) \ \cdots \ \mathbf{a}(u_M)] \ . \tag{3.6}$$

The lower branch signal is

$$\begin{aligned} \mathbf{x_{aux}}(n) &= \mathbf{B_s}^H \mathbf{x_{in}}(n) \\ &= \begin{bmatrix} x_2(n) \\ x_3(n) \\ \vdots \\ x_M(n) \end{bmatrix} \end{aligned} \tag{3.7}$$

where the signals $x_m(n)$ for $m = 2, 3, \ldots, M$ are auxiliary beam signals since the columns of $\mathbf{B_s}$ are spatial steering vectors at different azimuth angles.

The collection of the target steering vector and the steering vectors constituting

the columns of $\mathbf{B_s}$ forms an orthogonal transform from element space to beamspace

$$\mathbf{T} = [\mathbf{a_t} \ \mathbf{B_s}] \ . \tag{3.8}$$

The beamspace transform performs a spatial discrete Fourier transform (DFT) on the array snapshots at frequencies determined by the assumed target azimuth. The beamspace signal is

$$\begin{aligned} \mathbf{x_{bs}}(n) &= \mathbf{T}^H \mathbf{x_{in}}(n) \\ &= \begin{bmatrix} x_1(n) \\ x_2(n) \\ \vdots \\ x_M(n) \end{bmatrix} \\ &= \begin{bmatrix} y(n) \\ \mathbf{x_{aux}}(n) \end{bmatrix} . \end{aligned} \tag{3.9}$$

The entire structure is known as the beamspace GSC [36, 37].

The mainbeam TSI has significant temporal correlation, as noted earlier. Therefore, the beamspace TSI canceler requires temporal taps within the individual beams as shown in Fig. 3.4. We choose to restrict the beamspace TSI canceler to have an equal number of taps in each beam so that the temporal window of the canceler is simply the number of temporal taps per beam. Recall that the mainbeam TSI has a rank that is determined by the number of samples from the jammer waveform contributing to the interference. This rank is equal to the degrees of freedom necessary for the SRB canceler to achieve suppression to the thermal noise floor. However, the beamspace GSC has $(M-1)$ spatial degrees of freedom, all potentially containing temporal information for cancellation. If the TSI has significant angular spread, TSI signals highly correlated with the mainbeam interference can be found in the multiple auxiliary beams of the beamspace TSI canceler. These additional TSI signals help to reduce the size of the temporal window. However, if the TSI is mostly confined to the mainbeam, then little gain in the reduction of the temporal window can be ex-

pected, as the significant information is limited to the direct-path. The length of the temporal window required is therefore data dependent. As a rule of thumb supported by the experimental results reported in Section 3.6, we suggest setting the size of the temporal window of the beamspace TSI canceler, T_{bs} to be

$$T_{bs} > \frac{T_{tsi}}{M-1} , \tag{3.10}$$

where T_{tsi} is the temporal extent of the mainbeam TSI. Therefore, T_{bs} can in general be significantly smaller than T_{tsi} as the number of elements M is increased. The number of temporal taps required is

$$N_{bs} = T_{bs} \cdot F_s , \tag{3.11}$$

determined by the radar sampling frequency, F_s, and the size of the temporal window of the beamspace TSI canceler, T_{bs}. Note that for $N_{bs} = \frac{N_r}{M-1}$ (N_r is the number of temporal taps in the SRB canceler), the SRB and the beamspace TSI cancelers have the same total number of adaptive degrees of freedom.

The next task is to compute the adaptive weights $\mathbf{w_{bs}}$ for the beamspace TSI canceler. Let the signal from each of the $(M-1)$ auxiliary beams be $x_m(n)$ for $m = 2, 3, \ldots, M$. The beamspace signal prediction vector is made up of the components used to estimate the mainbeam TSI. First, constructing the $N_{bs} \times 1$ sub-vectors made up of the mth auxiliary beam signal at the different integer delays

$$\mathbf{x_m}(n) = [x_m(n) \;\; x_m(n-1) \;\; \cdots \;\; x_m(n-N_{bs}-1)]^T . \tag{3.12}$$

where N_{bs} is the number of temporal taps per beam, the complete beamspace signal prediction vector, $\mathbf{x}(n)$ is then obtained by concatenating the individual beamspace signal vectors from (3.12) as

$$\mathbf{x}(n) = \begin{bmatrix} \mathbf{x_2}(n) \\ \mathbf{x_3}(n) \\ \vdots \\ \mathbf{x_M}(n) \end{bmatrix} . \tag{3.13}$$

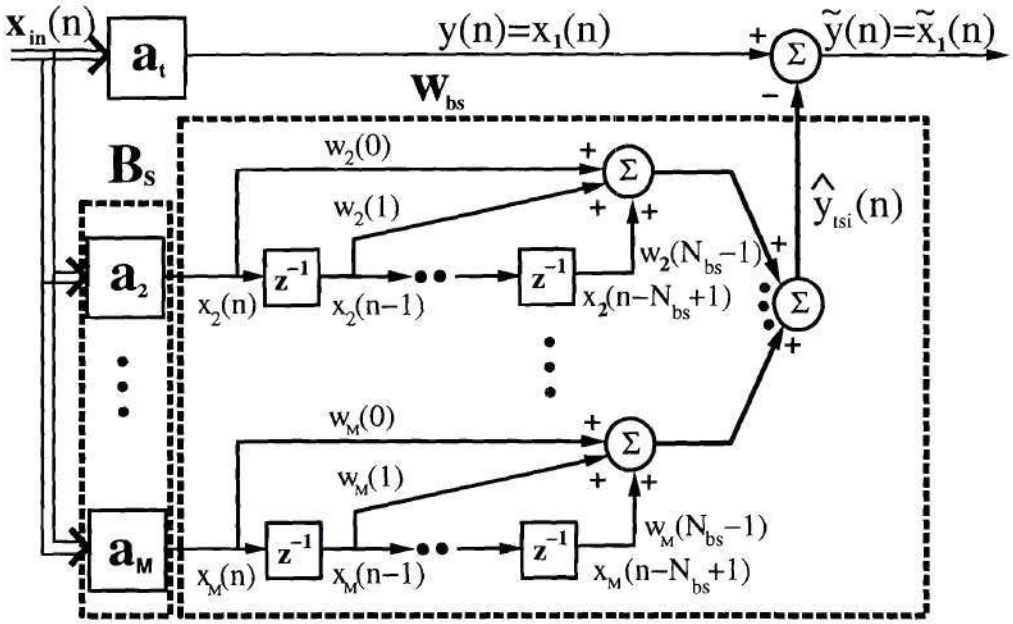

Figure 3.4: Beamspace TSI canceler.

Therefore, the total degrees of freedom for the canceler, K_F, is the product of the number of temporal samples and the number of auxiliary beams, i.e.,

$$K_F = N_{bs} \cdot (M-1) \ . \tag{3.14}$$

The adaptive canceler predicts the mainbeam TSI signal from the $(M-1)$ mutually orthogonal beamspace signals at the N_{bs} taps as shown in Fig. 3.4. The adaptive weight vector $\mathbf{w_{bs}}$ is found using the MMSE criterion and the multi-channel Wiener-Hopf equation [67], which requires knowledge of the covariance matrix of the signal prediction vector and the cross-covariance vector between the beamspace signal prediction vector in (3.13) and the mainbeam signal in the upper branch (3.1). The $K_F \times K_F$ beamspace covariance matrix is

$$\mathbf{R_x} = E\left\{\mathbf{x}(n)\mathbf{x}^H(n)\right\} \ , \tag{3.15}$$

and the $K_F \times 1$ cross-covariance vector is

$$\mathbf{r_{xy}} = E\left\{\mathbf{x}(n)y^*(n)\right\} \ . \tag{3.16}$$

The beamspace adaptive weight vector is found from the Wiener-Hopf equation

$$\mathbf{w_{bs}} = \begin{bmatrix} \mathbf{w_2} \\ \vdots \\ \mathbf{w_m} \\ \vdots \\ \mathbf{w_M} \end{bmatrix} = \mathbf{R_x^{-1}}\,\mathbf{r_{xy}} \ , \tag{3.17}$$

where each of the MMSE weight vectors $\mathbf{w_m}$ is an $N_{bs} \times 1$ vector for the mth beamspace signal given by

$$\mathbf{w_m} = [w_m(0)\ w_m(1)\ \cdots\ w_m(N_{bs}-1)]^T \ . \tag{3.18}$$

The estimate of the mainbeam TSI signal is

$$\begin{aligned} \hat{y}_{tsi}(n) &= \mathbf{w_{bs}^H}\,\mathbf{x}(n) \\ &= \sum_{m=2}^{M}\sum_{k=0}^{N_{bs}-1} w_m^*(k)\,x_m(n-k) \ , \end{aligned} \tag{3.19}$$

and the output of the beamspace canceler is

$$\tilde{y}(n) = y(n) - \hat{y}_{tsi}(n) \ . \tag{3.20}$$

3.3 Performance Analysis

The standard measure of performance for TSI mitigation is the amount of interference energy remaining after cancellation. The energy is measured with respect to the thermal noise floor as the residual interference-to-noise ratio (INR). In the absence of a target signal, the residual INR is simply the power of the output from the canceler,

$\tilde{y}(n)$, normalized by the thermal noise power. The output power of the canceler is

$$\begin{aligned}
\sigma_{\tilde{y}}^2 &= \mathrm{E}\left\{|\tilde{y}(n)|^2\right\} \\
&= \mathrm{E}\left\{|y(n) - \hat{y}_{tsi}(n)|^2\right\} \\
&= \mathrm{E}\left\{|y_t(n)|^2\right\} + \mathrm{E}\left\{|y_i(n)|^2\right\} - \mathrm{E}\left\{|\hat{y}_{tsi}(n)|^2\right\} \\
&= \sigma_t^2 + \sigma_i^2 - \mathrm{E}\left\{|\hat{y}_{tsi}(n)|^2\right\} \ .
\end{aligned} \tag{3.21}$$

$y_t(n)$ and $y_i(n)$ are the target and interference signals in the upper branch of the canceler with respective powers of σ_t^2 and σ_i^2. Note that the interference consists of both TSI and thermal noise. The residual interference signal is given by

$$\begin{aligned}
\tilde{\sigma}_i^2 &= \sigma_i^2 - \mathrm{E}\left\{|\hat{y}_{tsi}(n)|^2\right\} \\
&= \sigma_i^2 - \mathrm{E}\left\{\left|\mathbf{w}_{\mathbf{bs}}^H \mathbf{x}(n)\right|^2\right\} \\
&= \sigma_i^2 - \mathbf{w}_{\mathbf{bs}}^H \mathbf{R}_{\mathbf{x}} \mathbf{w}_{\mathbf{bs}} \\
&= \sigma_i^2 - \mathbf{r}_{\mathbf{xy}}^H \mathbf{R}_{\mathbf{x}}^{-1} \mathbf{r}_{\mathbf{xy}} \ .
\end{aligned} \tag{3.22}$$

Therefore, the amount of residual INR is determined by the mainbeam interference contained in the cross-covariance vector and covariance matrix. The amount of residual interference is a function of the size of the temporal window in the beamspace canceler (or the SRB canceler) and the spatio-temporal characteristics of the TSI. One common method of analyzing TSI is by examining the cross-covariance vector, $\mathbf{r}_{\mathbf{xy}}$, as a function of the assumed target direction. In the case of the beamspace canceler, the mainbeam is cross-correlated with the remaining auxiliary beams, whereas the SRB canceler uses the direct-path jammer auxiliary beam.

Others have reported their results in terms of the cancellation ratio which is a measure of the amount of TSI energy removed by the canceler [5, 17] and is simply the difference in TSI energy before and after cancellation. However, the amount of TSI energy cancelled is a function of the original amount of TSI present and does not indicate how much interference remains after cancellation. Since the ultimate goal of the processor is to improve detection performance which is directly related to the signal-to-interference-plus-noise ratio (SINR), the residual INR seems to be a more

appropriate figure of merit. Note that if no signal cancellation occurs, the SNR is fixed, and SINR and residual INR are equivalent figures of merit.

3.4 Implementation with Sample Matrix Inversion

As with the SRB canceler, the beamspace TSI canceler is implemented with the sample matrix inversion (SMI) technique [54]. For this method, the covariance matrix and the cross-covariance vector, $\mathbf{R_x}$ and $\mathbf{r_{xy}}$, are estimated from the data under consideration. The sample covariance matrix, $\hat{\mathbf{R}}_\mathbf{x}$, is

$$\hat{\mathbf{R}}_\mathbf{x} = \frac{1}{N_t} \sum_{k=1}^{N_t} \mathbf{x}(n_t(k))\mathbf{x}^H(n_t(k)) \ , \tag{3.23}$$

and the sample cross-covariance vector, $\hat{\mathbf{r}}_\mathbf{xy}$, between the signal prediction vector, $\mathbf{x}(n)$, and the mainbeam signal, $y(n)$, is

$$\hat{\mathbf{r}}_\mathbf{xy} = \frac{1}{N_t} \sum_{k=1}^{N_t} \mathbf{x}(n_t(k))y^*(n_t(k)) \ . \tag{3.24}$$

The number of training samples available is N_t, and $n_t(k)$ are the snapshot indices that define the training interval. The training interval can be either the entire PRI or some subset of the range samples ($n = 1, 2, \ldots, N$). In the presence of monostatic clutter, a dedicated training interval from a "clutter-free" region of the PRI, typically at far-field ranges, should be reserved for TSI weight training. Otherwise, clutter returns degrade the performance of the adaptive weights. Although the clutter and TSI signals are uncorrelated

$$\mathrm{E}\left\{\mathbf{x_c}(n)\mathbf{x}_\mathbf{tsi}^H(n)\right\} = \mathbf{0} \ , \tag{3.25}$$

a finite number of samples results in non-zero estimated cross-covariances. The leakage of these non-zero covariances into the adaptive weights causes a drop-off in TSI mitigation performance [22].

The SMI adaptive weight vector is an ML estimate of the theoretical weight vector. Although the SMI weight vector is optimal in terms of MMSE for the sample

data from the training interval, the same is not true of data elsewhere in the PRI. However, all signals are assumed to be approximately stationary over the PRI, and the SMI weight vector approaches the desired MMSE weight vector of the PRI as the number of samples is increased.

The sample covariance matrix and cross-covariance vector are used as estimates of their theoretical counterparts in (3.15) and (3.16) and are substituted into (3.17) to obtain the SMI adaptive weight vector

$$\hat{\mathbf{w}}_{\mathbf{bs}} = \hat{\mathbf{R}}_{\mathbf{x}}^{-1}\, \hat{\mathbf{r}}_{\mathbf{xy}} \ . \tag{3.26}$$

The SMI weights are applied to the signal prediction vector $\mathbf{x}(n)$, i.e., the auxiliary beam signals at the various delays of the canceler, as in (3.19), to obtain an estimate of the interference. This estimate is subtracted from the mainbeam signal.

The sample covariance statistics, i.e., the sample covariance matrix and the sample cross-covariance vector, are ML estimates of their true counterparts. As the number of snapshots N_t increases, the performance of the adaptive weights approaches those of the optimum processor. Reed, Mallet, and Brennan [54] have proposed the use of the ratio of output SINRs of the SMI and optimum processors given by

$$\rho = \frac{\mathrm{SINR}_{\mathrm{SMI}}}{\mathrm{SINR}_{\mathrm{O}}} \tag{3.27}$$

as a metric of the performance of the SMI adaptive processor. The expected value of the metric is [54]

$$\mathrm{E}(\rho) = \frac{N_t + 2 - K_F}{N_t + 1} \ , \tag{3.28}$$

where K_F is the number of degrees of freedom of the beamspace TSI canceler given by (3.14). In order to achieve performance within 3 dB of the optimum, the minimum number of snapshots needed is [54]

$$N_t \geq 2K_F - 3 \ . \tag{3.29}$$

In addition, the variance of the metric was shown to be [4]

$$var(\rho) = \frac{(N_t - K_F + 2)(K_F - 1)}{(N_t + 1)^2(N_t + 2)} \ , \tag{3.30}$$

provided the sample covariance matrix is of full rank, i.e., $N_t > K_F$. A method of reducing this variance and improving the performance of the beamspace canceler by diagonal loading the sample covariance matrix is discussed in Section 3.7.

3.5 Constrained Element Space Processor Formulation

The beamspace TSI canceler is implemented using a GSC architecture which is an alternative realization of the linearly constrained minimum variance (LCMV) processor [28]. The beamspace GSC has the appealing interpretation of an adaptive canceler that predicts the mainbeam interference with auxiliary beam signals. However, the lower and upper branch signals, $y(n)$ and $\mathbf{x_{aux}}(n)$, vary according to the assumed target direction. Therefore, the solution of the adaptive weights $\mathbf{w_{bs}}$ requires that the sample covariance matrix, the cross-covariance vector, and the inverse of the sample covariance matrix be recomputed for all possible target directions. However, this shortcoming can be overcome using the original LCMV formulation that has a common element space sample covariance matrix that is independent of the assumed target direction. As will be shown, the element space covariance matrix and its inverse need to be computed only once. The resulting inverse sample covariance matrix is stored in memory for the solution of the adaptive weights for arbitrary target directions. This realization is known as the *constrained element space processor* (CESP) and is equivalent to the beamspace GSC from Fig. 3.4.

The CESP adaptive weights $\mathbf{w_e}$ operate on the element space signal vector,

$\mathbf{x_e}(n)$, that is made up of the input signal at various delays

$$\mathbf{x_e}(n) = \begin{bmatrix} x_{in}^{(1)}(n) \\ x_{in}^{(1)}(n-1) \\ \vdots \\ x_{in}^{(1)}(n-N_{bs}-1) \\ \vdots \\ x_{in}^{(m)}(n) \\ x_{in}^{(m)}(n-1) \\ \vdots \\ x_{in}^{(m)}(n-N_{bs}-1) \\ \vdots \\ x_{in}^{(M)}(n) \\ x_{in}^{(M)}(n-1) \\ \vdots \\ x_{in}^{(M)}(n-N_{bs}-1) \end{bmatrix} . \tag{3.31}$$

The subscript e indicates that the signal prediction vector is formed in element space. The notation for this column vector is that the element $x_{in}^{(m)}(n)$ denotes the mth element of the original input signal vector $\mathbf{x_{in}}(n)$ for $m = 1, 2, \ldots, M$. The output of the processor is

$$\tilde{y}(n) = \mathbf{w_e}^H \mathbf{x_e}(n) \ . \tag{3.32}$$

The CESP weight vector $\mathbf{w_e}$ is found by minimizing the output power subject to a set of constraints, i.e.,

$$\min_{\mathbf{w_e}} \left| \mathbf{w_e}^H \mathbf{x_e}(n) \right|^2 \quad \text{subject to} \quad \mathbf{C}^H \mathbf{w_e} = \mathbf{d} \ , \tag{3.33}$$

where $\mathbf{C}$ is the constraint matrix and $\mathbf{d}$ is the vector of the desired responses to the various constraints. The columns of $\mathbf{C}$ describe the constraint conditions (usually space-time steering vectors), and $\mathbf{d}$ is the set of responses to the conditions. The

covariance matrix of the element space constraint signal vector is

$$\mathbf{R_e} = \mathrm{E}\left\{\mathbf{x_e}(n)\mathbf{x_e}^H(n)\right\} \ . \tag{3.34}$$

Recall that the beamspace TSI canceler has a distortionless response in the assumed target direction at zero lag. Since no temporal taps are contained in the upper branch in Fig. 3.4, the response to non-zero lags must be zero. Therefore, the constraints for the TSI canceler are

$$\left(\mathbf{a_t} \otimes \mathbf{e_n}\right)^H \mathbf{w_e} = \begin{cases} 1, & \text{for} \quad n = 1; \\ 0, & \text{for} \quad n > 1; \end{cases} \tag{3.35}$$

where $\mathbf{e_n}$ is the $N_{bs} \times 1$ unit vector with only one non-zero value for the nth element, which is equal to one. This unit vector selects the nth temporal tap at a delay of $n-1$. The CESP constraint matrix can then be written as

$$\mathbf{C} = \mathbf{a_t} \otimes \mathbf{I} \ , \tag{3.36}$$

where $\mathbf{I}$ is the $N_{bs} \times N_{bs}$ identity matrix. The corresponding desired constraint response vector is

$$\mathbf{d} = [1 \ 0 \ \cdots \ 0]^T = \mathbf{e_1} \ . \tag{3.37}$$

The constrained optimization problem from (3.33) is solved using Lagrange multipliers to find the CESP weight vector [32]

$$\mathbf{w_e} = \mathbf{R_e}^{-1}\mathbf{C}\left(\mathbf{C}^H\mathbf{R_e}^{-1}\mathbf{C}\right)^{-1}\mathbf{d} \ . \tag{3.38}$$

The relation between the CESP adaptive weight vector and the beamspace GSC adaptive weight vector $\mathbf{w_{bs}}$ is

$$\begin{aligned} \mathbf{w_e} &= \mathbf{a_t} \otimes \mathbf{e_1} - \mathbf{B_{st}}\mathbf{w_{bs}} \\ &= \mathbf{a_t} \otimes \mathbf{e_1} - \left(\mathbf{B_s} \otimes \mathbf{I}\right)\mathbf{w_{bs}} \end{aligned} \tag{3.39}$$

where $\mathbf{I}$ is a $N_{bs} \times N_{bs}$ identity matrix that models the tapped delay line network in the lower branch of the beamspace canceler. The spatio-temporal blocking matrix $\mathbf{B_{st}}$ consists of the spatial blocking matrix $\mathbf{B_s}$ for the N_{bs} tapped delays.

3.6 Mitigation Results with Experimental Data

The performance of the full beamspace and the single-reference beam (SRB) cancelers are compared for a variety of experiments. In all cases, the data used was collected as part of the DARPA/Navy Mountaintop experiment [40, 61]. The array used had $M = 14$ elements uniformly spaced at $d = 0.33$ meters. The radar carrier frequency was 435 MHz, the sampling frequency was 1 MHz, and the returns were collected in bursts of 16 pulses. The experiment was performed with the radar receiver positioned on top of a mountain to simulate an airborne environment. The data files used contain returns from both a ground-based and an airborne TSI-producing jammer. In all cases, the radar receiver was in passive mode (i.e., receiving only, not transmitting) so that no monostatic clutter is present in the returns.

3.6.1 Blind Interval Results

The adaptive weights were computed for each individual PRI with the SMI technique using returns from the entire PRI to compute the sample covariance matrix and sample cross-covariance vector. When processing the data, the canceler is empty at the beginning of the PRI and begins to fill up with samples as the data propagates through the tapped delay lines. During this period, full cancellation cannot be achieved because the canceler does not have access to the entire interval on the jammer waveform that produced the TSI. Detection performance suffers as a result, and the processor is unable to resolve weaker targets. During this period, the canceler is said to be "blind" and is consequently known as the blind interval of the canceler. One of the motivations behind the beamspace TSI canceler is the desire to reduce the size of the temporal window of the canceler which leads to a shorter blind interval. Fig. 3.5 shows the outputs of the SRB and the beamspace TSI cancelers chosen to have similar performance in terms of residual INR, where the TSI has been driven down close to the thermal noise floor (INR = 0 dB). The two cancelers

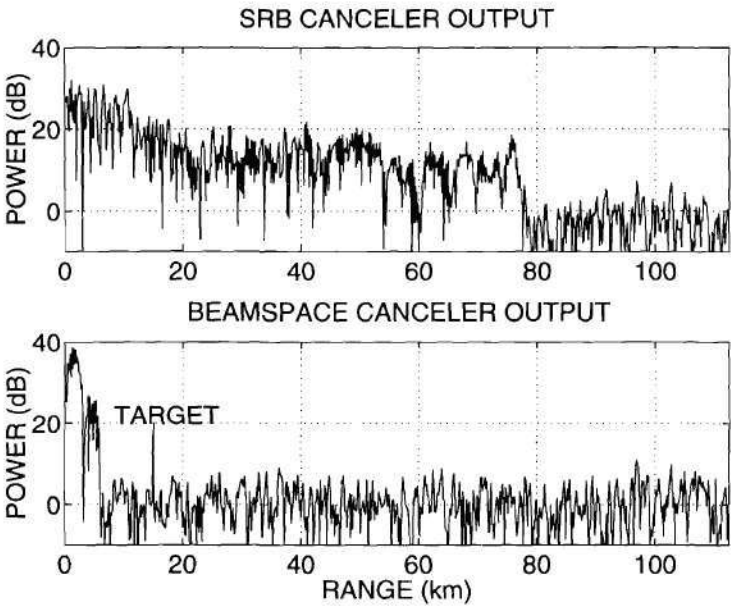

Figure 3.5: Comparison of blind intervals for SRB and beamspace cancelers. Target (SNR = 20 dB) injected at a range of 15 kilometers (range cell 100).

---

are implemented with an equivalent number of degrees of freedom (520), so that the temporal window of the SRB canceler has 520 samples, while its beamspace counterpart has only 40 samples (per beam). The data set used contains TSI produced by a ground-based jammer with broadside at 270° in azimuth (Mountaintop data file = `mmit004v1.mat`). A point target has been injected at range cell 100 (range = 15 kilometers) with SNR = 20 dB. Since the blind interval is equal to the length of the temporal window, the SRB canceler does not achieve full cancellation until after 520 range cells (range = 78 kilometers). Clearly, the target cannot be extracted. On the other hand, the beamspace canceler achieves full cancellation after 40 range cells (6 kilometers) so that the target is easily detected.

In a second set of experiments, the performance of the two cancelers is compared for equivalent temporal windows using the same data set. The results are shown in Fig. 3.6 in terms of residual INR versus the length of the temporal window. Clearly,

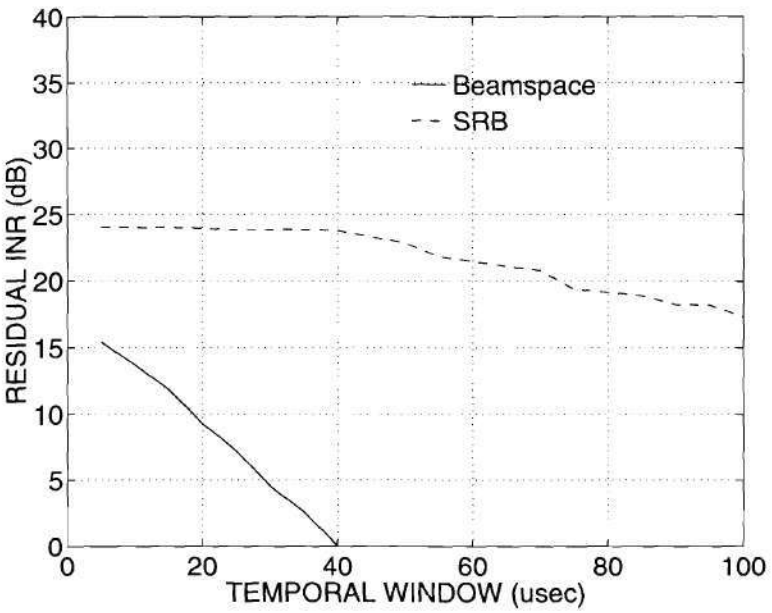

Figure 3.6: Residual INR versus temporal window size (Mountaintop data file = `mmit004v1.mat`).

the beamspace canceler outperforms the SRB canceler by a wide margin in terms of temporal window size. Note that this comparison of the two cancelers is not entirely fair because the number of degrees of freedom used by the beamspace canceler is greater by a factor of $(M-1)$ for equally sized temporal windows. However, it does serve to illustrate that TSI cancellation can be achieved with a substantial savings in the size of the temporal window and, therefore, with a diminished blind interval.

3.6.2 Ground-based TSI Jammer

The two cancelers were used to mitigate TSI produced by a ground-based jammer, first with broadside at 270° (Mountaintop data file = `mmit004v1.mat`) and then with broadside at 230° (Mountaintop data file = `mmit013v1.mat`). In both cases, the jammer has the same location (303° azimuth). Here, the results are reported in terms of residual INR versus the complexity of the canceler, i.e., the number of degrees of

freedom, a somewhat less biased means of comparing the two cancelers. However, recall that the size of the temporal window of the beamspace canceler is always a multiplicative factor of $(M-1)$ smaller than the temporal window of the SRB canceler. Fig. 3.7 shows the residual INR versus adaptive degrees of freedom for the first data experiment. Both cancelers have very similar performance, with one or the other having slightly better performance for the different degrees of freedom. The differences in performance relate to the information collected by the canceler as the temporal window is opened (i.e., the number of taps is increased). As critical information, e.g., a temporal sample highly correlated with the mainbeam interference, enters the temporal window of the canceler, a large improvement in interference suppression is achieved. The results for the second data file are shown in Fig. 3.8. In this case, the beamspace canceler has better performance for almost all degrees of freedom. Only for the largest number of degrees of freedom do the two cancelers have equivalent performance. Also, notice the decreased overall cancellation for both cancelers in this experiment which can be attributed to the jammer location. In the first experiment, the jammer is 33° off broadside, whereas in this experiment the jammer is 73° off broadside. Because of the non-linear relationship between spatial frequency u and azimuth ϕ ($u = \frac{d}{\lambda}\sin\phi$), a drastic loss in resolution occurs at larger azimuth angles.

3.6.3 Airborne TSI Jammer

Next the two cancelers were compared on experimental data with an airborne TSI-producing jammer (Mountaintop data file = `rio043v1.mat`). The airborne jammer differs from the ground-based jammer because of the imposed Doppler frequency from the relative aircraft motion [51, 57]. TSI incident on the radar receiver from the different azimuth angles contains different Doppler frequencies determined by both the receiver and jammer velocities. To cancel TSI at these different Doppler frequencies, the SRB canceler requires the reference beam signal to be modulated by the different Doppler shifts present in the TSI returns. The different modulation channels, known

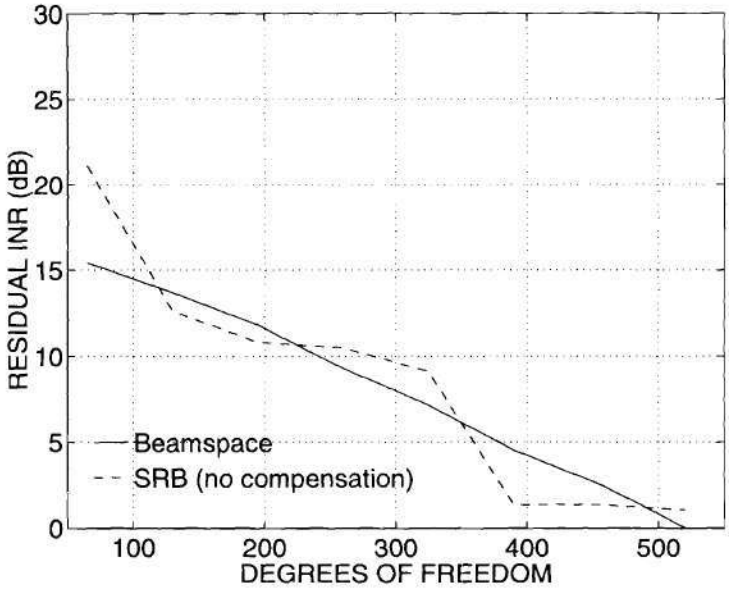

Figure 3.7: Residual INR versus degrees of freedom for a ground-based jammer. Broadside is 270° (Mountaintop data file = `mmit004v1.mat`).

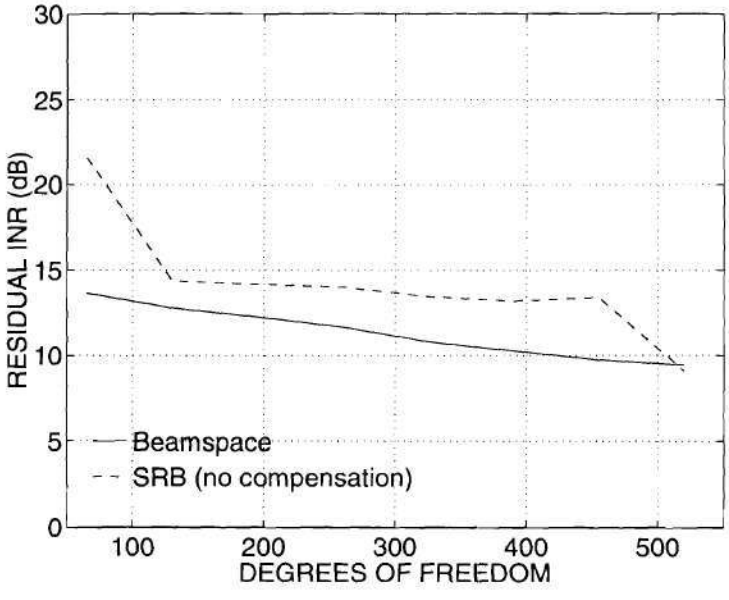

Figure 3.8: Residual INR versus degrees of freedom for a ground-based jammer. Broadside is 230° (Mountaintop data file = `mmit013v1.mat`).

as Doppler compensation channels, are then input into the adaptive canceler. However, the actual modulation frequencies are not known a priori and must be estimated from the sample data. Also, the imposition of Doppler compensation multiplies the number of adaptive degrees of freedom, which are already very large, by the number of compensation channels. Therefore, the beamspace canceler was compared with the SRB canceler without compensation channels. Note that the beamspace TSI canceler is capable of automatic Doppler compensation because the observed sidelobe TSI signals arrive with different Doppler shifts determined by the geometry of the airborne scenario. The adaptive canceler weights the sidelobe TSI signals according to their cross-correlation with the different Doppler frequencies present in the mainbeam interference. Cancellation results are shown in Fig. 3.9 in terms of residual INR versus adaptive degrees of freedom. The SRB canceler is unable to effectively cancel the interference, as the residual INR is still above 20 dB even for the most degrees of freedom used (520). The beamspace canceler is able to achieve a level of cancellation below 15 dB for almost all degrees of freedom used with a minimum of about 12 dB for 520 degrees of freedom. Since the beamspace canceler is able to exploit the Doppler components present in the sidelobe TSI, i.e., automatically perform Doppler compensation, it is able to achieve a larger amount of interference suppression.

3.7 Robust TSI Mitigation

As will be shown in Chapter 5, TSI mitigation is typically performed prior to monostatic clutter cancellation within a factored processor. Clutter nulling is then performed using space-time adaptive processing (STAP). The STAP algorithm exploits the special relationship between Doppler and azimuth in the clutter returns that manifests itself in a locus of energy in the azimuth-Doppler spectrum known as the clutter ridge [67]. Since the TSI canceler is unable to null the monostatic clutter, it should pass it with as little distortion as possible. Amplification and phase distortion must

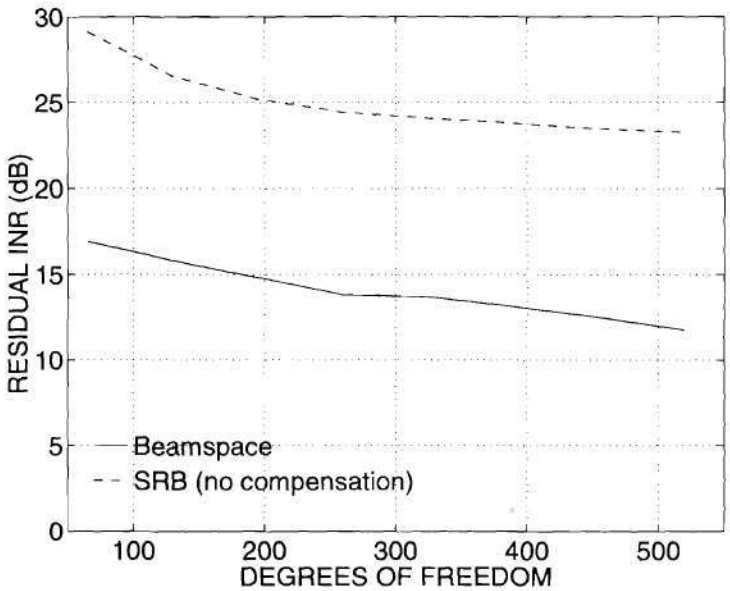

Figure 3.9: Residual INR versus degrees of freedom for an airborne jammer (Mountaintop data file = `rio043v1.mat`).

be kept to a minimum in order to preserve the spatio-temporal structure of the mono-static clutter returns. In order to make the SMI implementation of the beamspace TSI canceler more robust to limited sample size effects, we examine diagonal loading of the sample covariance matrix. The resulting adaptive processor is shown to have a better space-time frequency response with almost equivalent interference suppression performance. In addition, diagonal loading is shown to be equivalent to minimizing the white noise gain or the weight vector magnitude of the adaptive processor.

3.7.1 Adaptive Weight Vector Decomposition

The beamspace TSI canceler was implemented with a beamspace GSC. The TSI in the upper branch signal, $y(n)$, was estimated from the auxiliary beam signal vector in the lower branch, $\mathbf{x_{aux}}(n)$, at the delays within the range window of the canceler. Recall from (3.39) that the overall adaptive weight vector, $\mathbf{w}$, is equivalent to the

CESP weight vector

$$\begin{aligned} \mathbf{w} &= \mathbf{w_e} \\ &= \mathbf{w_q} - \mathbf{B_{st}}\mathbf{w_{bs}} \\ &= \mathbf{a_t} \otimes \mathbf{e_1} - (\mathbf{B_s} \otimes \mathbf{I})\mathbf{w_{bs}} \ , \end{aligned} \tag{3.40}$$

where $\mathbf{w_q}$ is the quiescent weight vector. The only quantity in (3.40) that is influenced by the actual radar returns is the adaptive weight vector from the lower branch, $\mathbf{w_{bs}}$. Assuming correct steering in the beamspace GSC, no target signal is present in the lower branch. Consequently, the signal prediction vector from (3.13) consists of TSI and sensor thermal noise only

$$\mathbf{x}(n) = \mathbf{x_{tsi}}(n) + \mathbf{x_n}(n) \ , \tag{3.41}$$

where $\mathbf{x_{tsi}}(n)$ and $\mathbf{x_n}(n)$ are the TSI and noise components, respectively. Therefore the covariance matrix can be written as

$$\mathbf{R_x} = \mathbf{R_{tsi}} + \mathbf{R_n} = \sum_{k=1}^{K_F} \lambda_k \mathbf{v_k} \mathbf{v_k}^H \tag{3.42}$$

where $\mathbf{v_k}$ and λ_k are the eigenvectors and eigenvalues of $\mathbf{R_x}$, in descending order of the eigenvalue magnitudes. Recall that K_F is the adaptive degrees of freedom of the beamspace canceler from (3.14). Assuming that the rank of the interference is R and the thermal noise is statistically independent in both space and time, the covariance matrix can be split into components representing its interference and noise subspaces [32]. The covariance matrix is rewritten as

$$\begin{aligned} \mathbf{R_x} &= \sum_{k=1}^{R} \lambda_k \mathbf{v_k} \mathbf{v_k}^H + \sum_{k=R+1}^{K_F} \sigma_n^2 \mathbf{v_k} \mathbf{v_k}^H \\ &= \sum_{k=1}^{R} (\beta_k + \sigma_n^2) \mathbf{v_k} \mathbf{v_k}^H + \sum_{k=R+1}^{K_F} \sigma_n^2 \mathbf{v_k} \mathbf{v_k}^H \end{aligned} \tag{3.43}$$

where σ_n^2 is the thermal noise power and β_k is the power of the kth strongest interference component. The interference power β_k is zero for $k > R$. Therefore, interference eigenvalues are the sum of the noise and interference powers, while the noise eigenvalues are simply the noise power. The associated noise eigenvectors span the subspace orthogonal to the interference subspace, but are otherwise arbitrary.

The adaptive weight vector, $\mathbf{w_{bs}}$, can be reformulated using the expression for the covariance matrix in (3.43). With further manipulation, the weight vector is

$$\begin{aligned}
\mathbf{w_{bs}} &= \mathbf{R_x}^{-1}\,\mathbf{r_{xy}} \\
&= \sum_{k=1}^{K_F} \frac{1}{\lambda_k}\mathbf{v_k}\mathbf{v_k}^H\mathbf{r_{xy}} \\
&= \frac{1}{\sigma_n^2}\mathbf{r_{xy}} - \left(\frac{1}{\sigma_n^2}\mathbf{r_{xy}} - \sum_{k=1}^{K_F}\frac{\langle \mathbf{r_{xy}}, \mathbf{v_k}\rangle}{\lambda_k}\mathbf{v_k}\right) \\
&= \frac{1}{\sigma_n^2}\mathbf{r_{xy}} - \sum_{k=1}^{K_F}\left(\frac{1}{\sigma_n^2} - \frac{1}{\lambda_k}\right)\langle \mathbf{r_{xy}}, \mathbf{v_k}\rangle\,\mathbf{v_k} \\
&= \frac{1}{\sigma_n^2}\left(\mathbf{r_{xy}} - \sum_{k=1}^{K_F}\frac{\lambda_k - \sigma_n^2}{\lambda_k}\langle \mathbf{r_{xy}}, \mathbf{v_k}\rangle\,\mathbf{v_k}\right)
\end{aligned} \tag{3.44}$$

where $\langle\cdot,\cdot\rangle$ denotes the inner product of two column vectors. Therefore, the weight vector, $\mathbf{w_{bs}}$, is the weighted sum of eigenvectors subtracted from the cross-covariance vector $\mathbf{r_{xy}}$, normalized by the noise power. The weighting of the eigenvectors is a function of the eigenvalues, the thermal noise power, and the energy shared by the individual eigenvectors and the cross-covariance vector, i.e., $\langle \mathbf{r_{xy}}, \mathbf{v_k}\rangle$. Note that the factor $\frac{\lambda_k - \sigma_n^2}{\lambda_k}$ is very close to 1 for large eigenvalues and equal to 0 for the noise eigenvalues ($\lambda_k = \sigma_n^2$). Thus, the adaptive weight vector, $\mathbf{w_{bs}}$, places deep nulls in the spatio-temporal spectrum with the eigenvectors corresponding to large eigenvalues, yet remains unaffected by the noise eigenvectors.

In practice, the adaptive weights are found using the SMI technique [54]. Recall that the SMI adaptive weight vector is

$$\hat{\mathbf{w}}_{\mathbf{bs}} = \hat{\mathbf{R}}_{\mathbf{x}}^{-1}\,\hat{\mathbf{r}}_{\mathbf{xy}}\ , \tag{3.45}$$

which can similarly be decomposed as (3.44) by replacing the eigenvalues, eigenvectors, and cross-covariance vectors with their estimates from the sample data. The accuracy of the estimates is determined by the number of samples used to compute the sample covariance statistics, N_t. As shown in (3.29), the number of snapshots

needed for performance within 3 dB of the optimum (i.e., using the true covariances) is $N_t = 2K_F - 3$. The drop-off in performance can be attributed to errors in the eigenvalue estimates, which have pronounced effects for the smaller eigenvalues. The errors in the noise eigenvalue estimates cause the factor $\frac{\hat{\lambda}_k - \sigma_n^2}{\hat{\lambda}_k}$ to be non-zero. The result is the addition of a random noise eigenvector to the overall weight vector for each noise eigenvalue. In turn, the space-time frequency response of the adaptive weights has elevated sidelobes due to the addition of the 2-D frequency responses of these random noise eigenvectors. Kelly found that the average sidelobe level is related to the number of snapshots used for the SMI estimates [34] by

$$\mathrm{E}\{\mathrm{SL}\} = \frac{1}{N_t + 1} \ . \tag{3.46}$$

For returns containing monostatic clutter with TSI, the elevated sidelobe levels will cause distortion of monostatic clutter returns. Therefore, the adaptive processor must seek to minimize the estimation errors in the SMI adaptive weight solution.

3.7.2 Sample Covariance Matrix Diagonal Loading

A common technique used to make the SMI adaptive weight computation more robust for limited sample sizes is the diagonal loading of the sample covariance matrix [12]. Diagonal loading refers to the addition of an identity matrix weighted by a loading factor σ_l^2. Note that the concept of diagonal loading is similar to noise injection, which has been suggested by Jablon [31] and Zahm [69] to help make adaptive processors more robust. If noise with power σ_l^2 is injected into the system, the true covariance matrix will have a diagonal matrix added to it as well. However, the injected noise sample covariance matrix is only approximately diagonal for finite sample sizes. However, direct diagonal loading of the sample covariance matrix in the SMI adaptive weight computation adds the true noise sample covariance matrix

$$\hat{\mathbf{w}}_{\mathbf{bs}} = \left(\hat{\mathbf{R}}_{\mathbf{x}} + \sigma_l^2 \, \mathbf{I}\right)^{-1} \hat{\mathbf{r}}_{\mathbf{xy}} \ , \tag{3.47}$$

where $\mathbf{I}$ is the $K_F \times K_F$ identity matrix. The result of diagonal loading is the addition of the loading power to all of the eigenvalue estimates without altering the eigenvectors. In addition, no actual noise is added for diagonal loading.

The effects of incorporating diagonal loading into the beamspace TSI canceler were studied using experimental data (`mmit004v1.mat` file). The loading power was set to the thermal noise floor ($\sigma_l^2 = \sigma_n^2$). Fig. 3.10 shows the eigenvalue distributions of the sample covariance matrix with and without diagonal loading. Using diagonal loading, the smallest eigenvalues level off at the noise floor. On the other hand, the sample covariance matrix without diagonal loading has noise eigenvalues that are significantly above and below the noise floor. Their offsets with respect to the thermal noise floor are the magnitudes of the random error vectors that are added to the adaptive weight vector. In this case, the errors ($\hat{\lambda}_k - \sigma_n^2$) are as high as -20 dB for the smallest eigenvalues. In addition, the resulting adaptive weights of the beamspace canceler are shown in Fig. 3.11 with and without diagonal loading. The effect of diagonal loading is to decrease the amplitude of the adaptive weights. As a result, monostatic clutter experiences less gain through the lower branch, decreasing the amount of distortion in the overall output. Recall that, ideally, the clutter is passed undistorted through the canceler during TSI mitigation. Next, the frequency response of the adaptive weights in one of the lower branch auxiliary beams is shown in Fig. 3.12. Without diagonal loading, the filter on the auxiliary beam amplifies the larger frequencies by as much as 10 dB. However, the beamspace TSI canceler with diagonal loading has greatly reduced sidelobe levels at these larger frequencies. Note that the effect on the response is negligible at lower frequencies, where most of the TSI is found. As a result, the cancellation performance remains almost unchanged. Fig. 3.13 shows the output of the canceler with and without diagonal loading. Their overall performances are virtually indistinguishable. Note that cancellation in the blind interval improved using diagonal loading, a result also reported by Gabel [22].

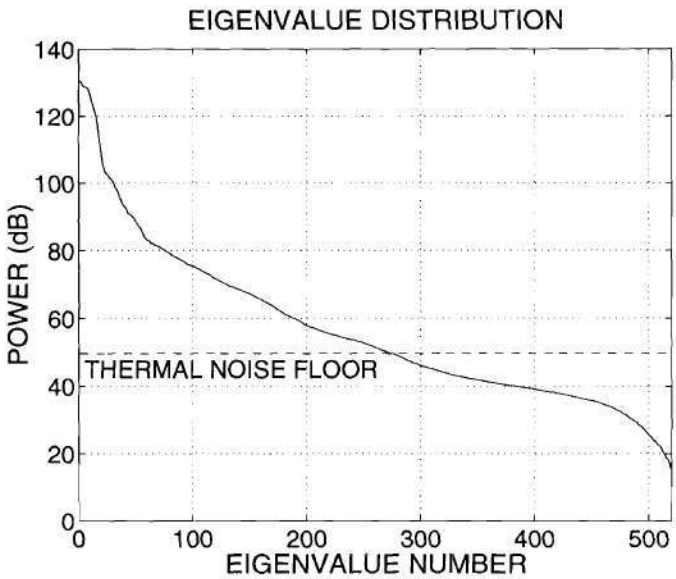

(a) No diagonal loading.

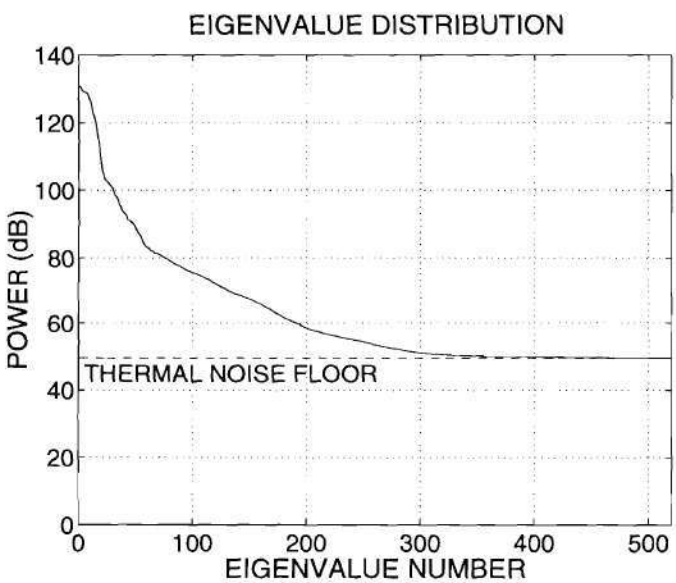

(b) Diagonal loading to the thermal noise floor.

Figure 3.10: Eigenvalue distributions of sample covariance matrices with and without diagonal loading. The diagonal loading power was set to the thermal noise floor (0 dB). The beamspace TSI canceler was implemented with 40 temporal taps per beam for a total of $K_F = 520$ degrees of freedom. The file used was `mmit004v1.mat`.

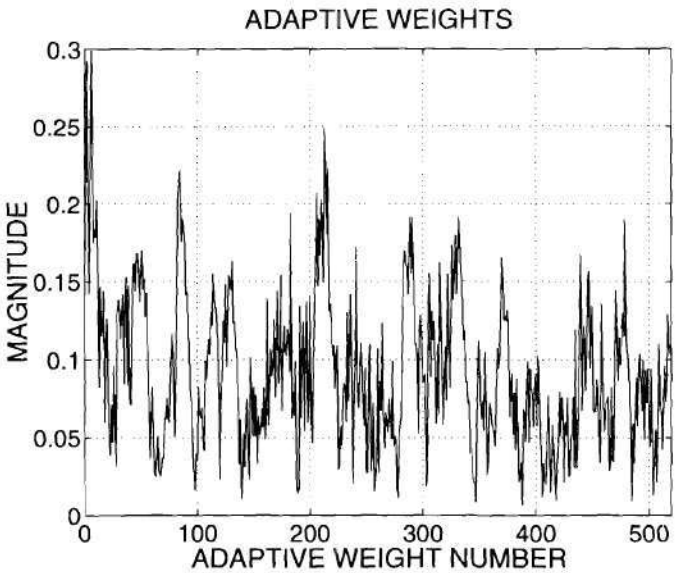

(a) No diagonal loading.

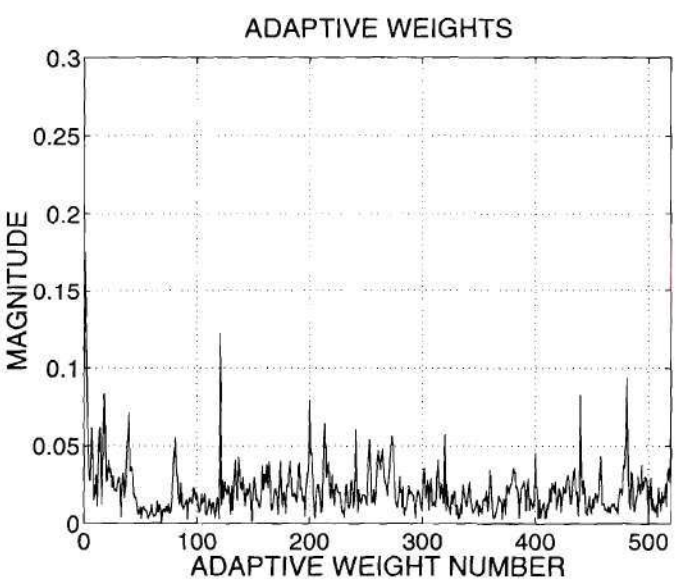

(b) Diagonal loading to the thermal noise floor.

Figure 3.11: Magnitude of the adaptive weights of the beamspace TSI canceler with and without diagonal loading of the covariance matrix. The diagonal loading power was set to the thermal noise floor (0 dB). The beamspace TSI canceler was implemented with 40 temporal taps per beam for a total of $K_F = 520$ degrees of freedom. The file used was `mmit004v1.mat`.

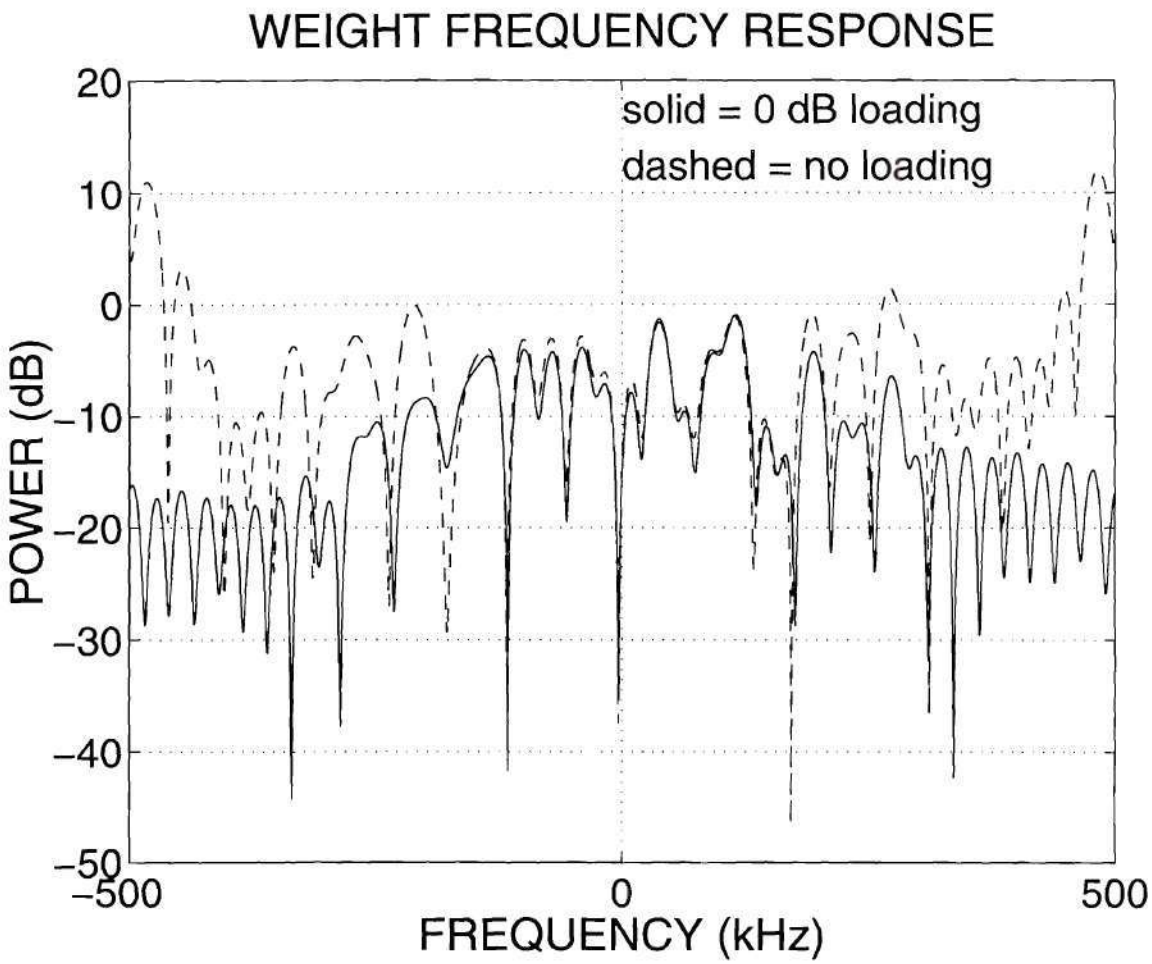

Figure 3.12: Frequency response of adaptive weights of beamspace TSI canceler with (solid line) and without (dashed line) diagonal loading of the covariance matrix. The diagonal loading power was set to the thermal noise floor (0 dB). The beamspace TSI canceler was implemented with 40 temporal taps per beam for a total of $K_F = 520$ degrees of freedom. The file used was `mmit004v1.mat`.

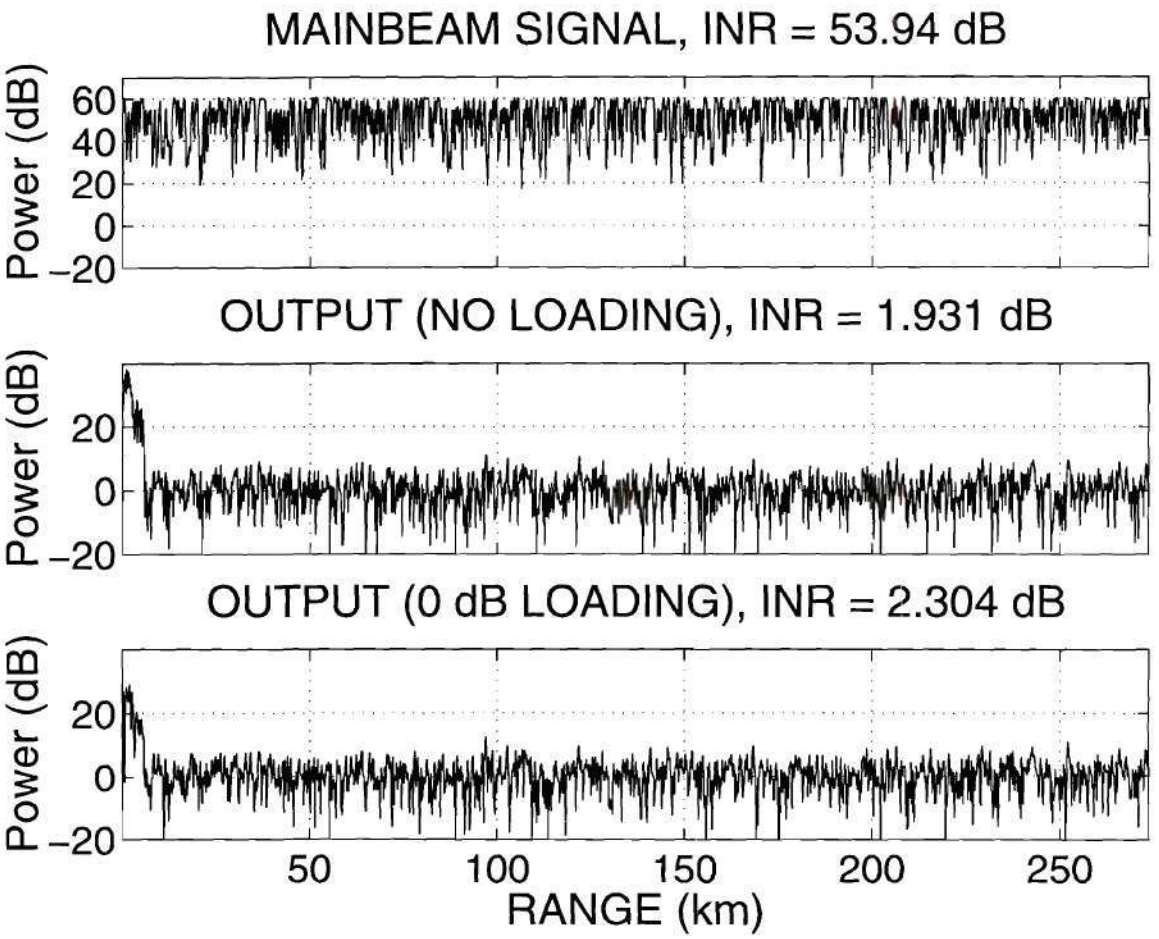

Figure 3.13: Performance of the beamspace TSI canceler with and without diagonal loading.The diagonal loading power was set to the thermal noise floor (0 dB). The beamspace TSI canceler was implemented with 40 temporal taps per beam for a total of $K_F = 520$ degrees of freedom. The file used was `mmit004v1.mat`.

3.7.3 White Noise Gain Minimization

Diagonal loading of the sample covariance matrix is a technique intended to make the SMI adaptive weights more robust to limited sample size effects. In the previous section, the method was demonstrated as a means of reducing the magnitude of the adaptive weight vector without adversely affecting its cancellation performance. The minimization of the weight vector magnitude can be attributed to the imposition of a lower bound on the sample covariance matrix eigenvalues [32]. As a result, the contribution of the noise eigenvectors to the adaptive weight vector from (3.44), set to zero in the theoretical case, was reduced. Note that diagonal loading is also a commonly used technique in mathematical statistics, where it is known as *ridge regression* or *regularization* [29, 44]. The motivation for its use in these applications is also the minimization of the weight vector.

Recall that in the GSC formulation, the beamspace canceler estimates the TSI in the upper branch signal, $y(n)$, from the signal prediction vector, $\mathbf{x}(n)$, made up of the auxiliary beam signals in the lower branch at the various time delays. The estimate of the mainbeam interference is

$$\hat{y}(n) = \mathbf{w}_{\mathbf{bs}}^H \, \mathbf{x}(n) \tag{3.48}$$

where $\mathbf{w_{bs}}$ is the adaptive weight vector. The white noise gain of the adaptive weight vector is found by measuring the output power when the input vector is a white noise vector, $\mathbf{x_n}(n)$, with unit variance ($\sigma_n^2 = 1$) and, therefore, a covariance matrix equal to the identity matrix, $\mathbf{I}$. The output power is

$$\begin{aligned} \mathrm{E}\left\{|\hat{y}(n)|^2\right\} &= \left\{\mathbf{w}_{\mathbf{bs}}^H \, \mathbf{x_n}(n) \, \mathbf{x_n}^H(n) \, \mathbf{w_{bs}}\right\} \\ &= \mathbf{w}_{\mathbf{bs}}^H \, \mathbf{I} \, \mathbf{w_{bs}} \\ &= \|\mathbf{w_{bs}}\|^2 \ . \end{aligned} \tag{3.49}$$

Therefore, minimization of the white noise gain is equivalent to minimizing the adaptive weight vector magnitude.

For the beamspace TSI canceler, the adaptive weights are found using the the MMSE criterion

$$\min_{\mathbf{w_{bs}}} \left| y(n) - \mathbf{w}_{\mathbf{bs}}^H \mathbf{x}(n) \right|^2 \ . \tag{3.50}$$

Although the problem is actually a constrained optimization problem, as shown in Section 3.5, this unconstrained formulation is made possible with the GSC architecture which maintains orthogonality between the upper branch constraint and the lower branch blocking matrix.

Since the covariance statistics are unknown, the adaptive weights are estimated using the SMI technique from (3.26). This equation can be rewritten in terms of data matrices and vectors. First, the sample covariance matrix from (3.23) is written as

$$\hat{\mathbf{R}}_{\mathbf{x}} = \frac{1}{N_t} \mathbf{X}\mathbf{X}^H \ . \tag{3.51}$$

The signal prediction data matrix, $\mathbf{X}$, is specified by filling its columns with the signal prediction vector, $\mathbf{x}(n)$, at the indices of the training interval

$$\mathbf{X} = [\, \mathbf{x}(n_t(1)) \ \mathbf{x}(n_t(2)) \ \cdots \ \mathbf{x}(n_t(N_t)) \,] \ . \tag{3.52}$$

Similarly, the sample cross-covariance vector from (3.24) is

$$\hat{\mathbf{r}}_{\mathbf{xy}} = \frac{1}{N_t} \mathbf{X}\mathbf{y}^H \tag{3.53}$$

where the upper branch data vector is given by

$$\mathbf{y} = [\, y(n_t(1)) \ \ y(n_t(2)) \ \cdots \ y(n_t(N_t)) \,] \ . \tag{3.54}$$

The solution of the SMI adaptive weights, $\hat{\mathbf{w}}_{\mathbf{bs}}$, is equivalent to satisfying (3.50) over the predetermined training interval used to estimate the covariance statistics, i.e.,

$$\min_{\hat{\mathbf{w}}_{\mathbf{bs}}} \left\| \mathbf{y} - \hat{\mathbf{w}}_{\mathbf{bs}}^H \mathbf{X} \right\|^2 \ , \tag{3.55}$$

and results in the solution

$$\begin{aligned} \hat{\mathbf{w}}_{\mathbf{bs}} &= \hat{\mathbf{R}}_{\mathbf{x}}^{-1} \hat{\mathbf{r}}_{\mathbf{xy}} \\ &= \left(\mathbf{X}\mathbf{X}^H \right)^{-1} \mathbf{X}\mathbf{y}^H \ . \end{aligned} \tag{3.56}$$

The SMI method yields an unbiased estimate of the adaptive weight vector, $\mathbf{w_{bs}}$, with a variance inversely proportional to the number of training samples available [54].

Recall that the adaptive weight vector was found from (3.47), using the SMI technique with the diagonal loading of $\hat{\mathbf{R}}_{\mathbf{x}}$. This equation can also be rewritten in terms of the signal prediction data matrix, $\mathbf{X}$, and the upper branch data vector, $\mathbf{y}$,

$$\begin{aligned} \hat{\mathbf{w}}_{\mathbf{bs}} &= \left(\hat{\mathbf{R}}_{\mathbf{x}} + \sigma_l^2 \mathbf{I}\right)^{-1} \hat{\mathbf{r}}_{\mathbf{xy}} \\ &= \left(\frac{1}{N_t}\mathbf{X}\mathbf{X}^H + \sigma_l^2 \mathbf{I}\right)^{-1} \frac{1}{N_t}\mathbf{X}\mathbf{y}^H \\ &= \left(\mathbf{X}\mathbf{X}^H + N_t\sigma_l^2 \mathbf{I}\right)^{-1} \mathbf{X}\mathbf{y}^H \ . \end{aligned} \tag{3.57}$$

The SMI weight vector is also the solution of the constrained optimization [29, 44]

$$\min_{\hat{\mathbf{w}}_{\mathbf{bs}}} \left\| \mathbf{y} - \hat{\mathbf{w}}_{\mathbf{bs}}^H \mathbf{X} \right\|^2 \quad \text{subject to} \quad \|\hat{\mathbf{w}}_{\mathbf{bs}}\|^2 \leq \kappa \tag{3.58}$$

where κ is a prespecified upper bound on the white noise gain that determines the diagonal loading power, σ_l^2. This constrained minimization also has an unconstrained formulation, found by augmenting the signal prediction data matrix with an identity matrix, $\mathbf{I}$, and the upper branch data vector with zeros [27]

$$\min_{\hat{\mathbf{w}}_{\mathbf{bs}}} \left\| [\mathbf{y} \ \ \mathbf{0}] - \hat{\mathbf{w}}_{\mathbf{bs}}^H [\mathbf{X} \ \ \sigma_l \mathbf{I}] \right\|^2 = \min_{\hat{\mathbf{w}}_{\mathbf{bs}}} \left\{ \left\| \mathbf{y} - \hat{\mathbf{w}}_{\mathbf{bs}}^H \mathbf{X} \right\|^2 + \sigma_l^2 \|\hat{\mathbf{w}}_{\mathbf{bs}}\|^2 \right\} . \tag{3.59}$$

Another interpretation of diagonal loading is as a means of introducing a slight bias in order to reduce the variance of the estimator and, thus, the white noise gain [29]. Thus, this biased estimator is a better estimate of the true adaptive weight vector in terms of its MSE

$$\|\hat{\mathbf{w}}_{\mathbf{bs}} - \mathbf{w}_{\mathbf{bs}}\|^2 \ . \tag{3.60}$$

The upper bound on the white noise gain of the adaptive weight vector found using SMI with diagonal loading is [29]

$$\|\hat{\mathbf{w}}_{\mathbf{bs}}\|^2 < \frac{K_F \sigma_n^2}{\sigma_l^2} = \kappa \ . \tag{3.61}$$

This bound can be used as a rule of thumb for the selection of the diagonal loading power, σ_l^2. In fact, it can also be shown that since $\sigma_l^2 > 0$, the use of diagonal loading

will always result in a reduction in the white noise gain of the adaptive weight vector [44]. Note that if diagonal loading of the sample covariance matrix is not used, i.e., $\sigma_l^2 = 0$, the white noise gain is unbounded.

3.8 Conclusions

In this chapter, the beamspace TSI canceler has been introduced and its performance demonstrated on experimental data. In addition, a robust implementation using the SMI technique with diagonal loading of the sample covariance matrix was presented. The canceler uses $(M-1)$ auxiliary beams, as opposed to the one jammer direct-path beam for the SRB canceler, to estimate and remove mainbeam TSI. Therefore, the TSI signal is predicted from both the direct-path jammer signal and TSI signals in the sidelobes of the mainbeam, i.e., any energy found in the other beams orthogonal to the mainbeam. In this manner, the temporal window of the canceler can be significantly decreased. In addition, the beamspace canceler has the advantage of requiring no a priori knowledge of the jammer location, making it robust to changing interference environments.

The other major advantage of the beamspace TSI canceler is that in the case of airborne TSI-producing jammers the sidelobe TSI signals collected in the auxiliary beams already contain components that have been Doppler shifted. Therefore, the collection of sidelobe TSI signals makes up a set of reference signals with different Doppler frequencies that can be used to estimate the different Doppler components of the mainbeam TSI. On the other hand, the SRB canceler requires modulation of the jammer direct-path signal at the Doppler frequencies of the interference to create Doppler compensation channels. Note that since the Doppler frequencies are not known a priori, they must be estimated first. However, the beamspace canceler requires no such a priori information and performs automatic Doppler compensation through the use of the sidelobe TSI signals. Therefore, the various sidelobe TSI signals

can be adaptively weighted to predict the different Doppler frequency components found in the mainbeam interference.

CHAPTER 4

Rank Reduction Techniques for TSI Mitigation

Rank reduction or weight thinning are terms used to describe the process of reducing the degrees of freedom of an adaptive algorithm. One of the primary motivations for reduced rank processors is the need for implementation in a real-time environment. Weight, power, and physical size limitations restrict the available computational resources, which in turn dictate a reduced dimension processor. In addition, the sample support for adaptive processing should contain a number of samples greater than twice the rank of the processor [54], which necessitates rank reduction. Since the number of samples available for adaptive weight training is limited by both the sampling frequency and non-stationarities in the interference environment, a large number of degrees of freedom, either spatial or temporal, is usually not available for adaptive processing. The rank reduction problem becomes one of determining the transformation into a lower dimensional subspace where the adaptive processing can be performed with performance nearly equal to that of the full rank processor.

Some of the first research on rank reduction in the context of adaptive arrays was reported by Chapman [14] and Morgan [49]. Chapman [14] looked at the use of several non-adaptive transforms to perform rank reduction. On the other hand, Morgan [49] used array partitioning methods and the subsequent processing of the sub-array outputs. Since the sub-array outputs consist of a mainbeam signal and its corresponding sidelobe signals, this method can be viewed as a beamspace method.

In general, beamspace techniques attempt to spatially isolate interference sources while discarding the other beams, i.e. spatial degrees of freedom, that do not contain interference sources. Several other beamspace rank reduction methods have been considered [9, 23, 59]. Although sources can be isolated very well with large arrays, the number of interference sources is often unknown and may not always be apparent in beamspace, due to significant energy leakage between beams. In contrast, decorrelating data-adaptive transforms isolate the individual interferers, making it much easier to determine the number of interference sources. Decorrelation of the signal requires application of the Karhunen-Loève transform, which is found via the eigendecomposition of the signal covariance matrix. Rank reduction based on eigendecompositions has been proposed using a transform made up of a subset of the eigenvectors corresponding to the largest eigenvalues, known as the principal components [52, 62, 64]. Another eigenvector transform has been proposed that uses the eigenvectors corresponding to an alternate metric [10, 25]. The Karhunen-Loève transform may also be approximated using several non-adaptive transforms [63] which can be used in place of the eigenvectors for the purposes of rank reduction [26, 56]. The use of data-adaptive transforms has also been considered in terms of an output power minimization method [66] for a set of predetermined scenarios. Also, linear constraints can be used to reduce the adaptive degrees of freedom [43]. For a simulation study into the performance of several of these methods see [65].

In the TSI problem, a large number of spatial and temporal degrees of freedom are available for the adaptive canceler [38]. Here, the rank reduction method looks to identify the most important spatial/temporal information in terms of its contribution to the mainbeam interference. In this chapter, a common framework for rank reduction within the beamspace TSI canceler is given. We also give an alternate interpretation of the MMSE Wiener filter in terms of the eigenvectors of the covariance matrix in order to gain insight into the rank reduction problem. A discussion on the application of several rank reduction strategies applied to the TSI problem is followed

by some results with experimental data.

4.1 The Reduced Rank Beamspace TSI Canceler

The beamspace TSI canceler takes the M element input signal $\mathbf{x_{in}}(n)$ and forms the mainbeam signal, $y(n)$, and $(M-1)$ auxiliary beams, denoted by the vector $\mathbf{x_{aux}}(n)$. An estimate of the mainbeam interference is obtained using equal length temporal windows on each of the auxiliary beams with N_{bs} taps per beam. The linearly constrained minimum variance canceler is implemented in a GSC structure as shown in Fig. 4.1. The MMSE estimate of the mainbeam interference is

$$\hat{y}_{tsi} = \mathbf{w}_{\mathbf{bs}}^H \mathbf{x}(n) \ , \tag{4.1}$$

where $\mathbf{x}(n)$ is the $K_F \times 1$ signal prediction vector from (3.13), formed with the auxiliary beam signals at the various delays in the temporal window as in (3.12). The $K_F \times 1$ adaptive weight vector $\mathbf{w_{bs}}$ is found from the MMSE Wiener-Hopf equation

$$\mathbf{w_{bs}} = \mathbf{R}_{\mathbf{x}}^{-1} \mathbf{r_{xy}} \ . \tag{4.2}$$

The terms $\mathbf{R_x} = \mathrm{E}\left\{\mathbf{x}(n)\mathbf{x}^H(n)\right\}$ and $\mathbf{r_{xy}} = \mathrm{E}\left\{\mathbf{x}(n)y^*(n)\right\}$ are the signal prediction vector covariance matrix and the cross-covariance vector between the signal prediction vector and the mainbeam signal $y(n)$, respectively. K_F is the number of adaptive degrees of freedom of the full rank beamspace canceler and is the product of the number of auxiliary beams and the temporal taps per beam

$$K_F = (M-1) \cdot N_{bs} \ . \tag{4.3}$$

For more details on the beamspace TSI canceler, see Chapter 3. The goal in this chapter is to look at methods of decreasing the number of adaptive degrees of freedom from the full rank, K_F, to some reduced rank, K_R. Therefore, the rank reduction problem becomes one of finding a $K_F \times K_R$ matrix $\mathbf{P_R}$ that projects the $K_F \times 1$

full rank signal prediction vector $\mathbf{x}(n)$ onto a K_R-dimensional subspace. The $K_R \times 1$ reduced rank signal prediction vector is

$$\mathbf{x_R}(n) = \mathbf{P_R^H}\,\mathbf{x}(n) \tag{4.4}$$

and the resulting reduced rank MMSE estimate of the mainbeam interference is

$$\hat{y}_{tsi}(n) = \mathbf{w_R^H}\,\mathbf{x_R}(n)\ , \tag{4.5}$$

where $\mathbf{w_R}$ is the reduced rank MMSE adaptive weight vector given by

$$\mathbf{w_R} = \mathbf{R_R^{-1}}\,\mathbf{r_{x_R y}}\ . \tag{4.6}$$

The covariance matrix of the reduced rank signal prediction vector is

$$\mathbf{R_R} = \mathrm{E}\left\{\mathbf{x_R}(n)\mathbf{x_R^H}(n)\right\} \tag{4.7}$$

and its cross-covariance vector with the mainbeam signal $y(n)$ is

$$\mathbf{r_{x_R y}} = \mathrm{E}\left\{\mathbf{x_R}(n)y^*(n)\right\}\ . \tag{4.8}$$

The reduced rank beamspace TSI canceler is shown in Fig. 4.2. The rank reduction problem becomes one of designing the projection matrix $\mathbf{P_R}$ that best preserves the performance of the full rank processor. An optimal projection matrix in the MMSE sense is elusive as has been noted by Van Veen [66]. Note that in the case of a reduced rank of one, the MMSE optimization of $\mathbf{P_R}$ leads directly to the solution of the MMSE Wiener-Hopf equation in (4.2) so that $\mathbf{P_R} \propto \mathbf{w_{bs}}$, the full rank weight vector. In general, using the MMSE criterion leads to the preservation of full rank performance. However, the MMSE criterion provides no savings in computation or sample support requirements. In essence, such a criterion is not reducing the adaptive degrees of freedom, it is actually preserving them. Therefore, we turn to eigenanalysis methods and their approximations to find the rank reduction projection matrix. However, before considering the design of the projection matrix, an alternate realization of the MMSE filter is derived in terms of an eigenvector filter bank.

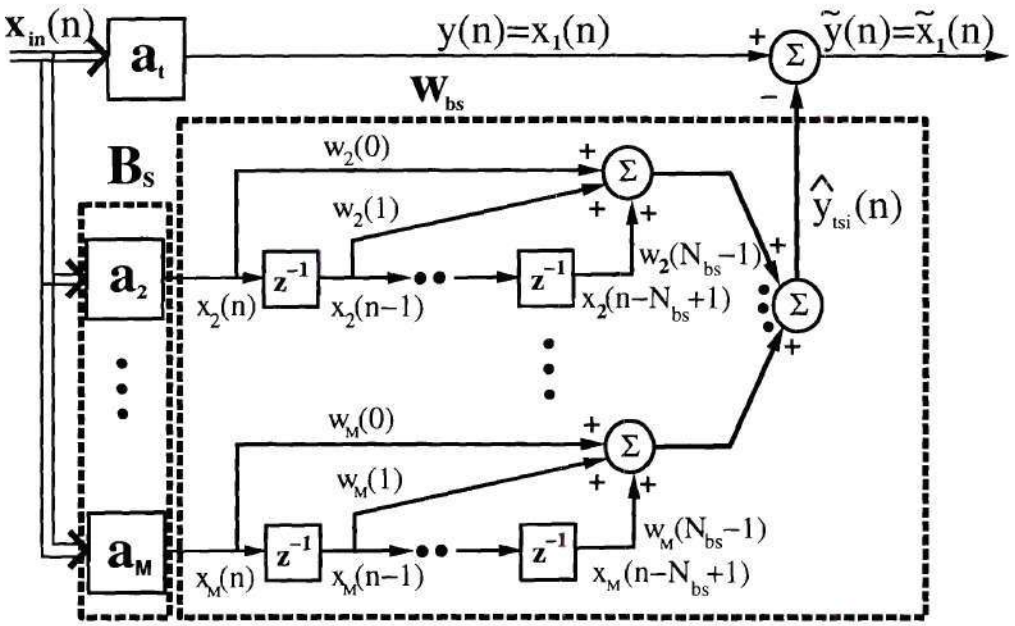

Figure 4.1: Full rank beamspace TSI canceler.

4.1.1 An Alternate Interpretation of MMSE Filtering

The full rank beamspace TSI canceler, shown in Fig. 4.1, has an adaptive weight vector given by

$$\mathbf{w_{bs}} = \mathbf{R_x^{-1}}\,\mathbf{r_{xy}} \ . \tag{4.9}$$

The covariance matrix in (4.7) can be written as the sum of the TSI and thermal noise covariance matrices or as the sum of two orthogonal subspaces

$$\begin{aligned} \mathbf{R_x} &= \mathbf{R_{tsi}} + \mathbf{R_n} \\ &= \sum_{k=1}^{K_F} \lambda_k \mathbf{v_k} \mathbf{v_k^H} \\ &= \sum_{k=1}^{R} \lambda_k \mathbf{v_k} \mathbf{v_k^H} + \sum_{k=R+1}^{K_F} \lambda_k \mathbf{v_k} \mathbf{v_k^H} \end{aligned} \tag{4.10}$$

where R is the rank of the interference (TSI). The eigenvalue and eigenvector pairs, λ_k and $\mathbf{v_k}$, are in descending order of the eigenvalues (λ_1 is the greatest, λ_{K_F} is the

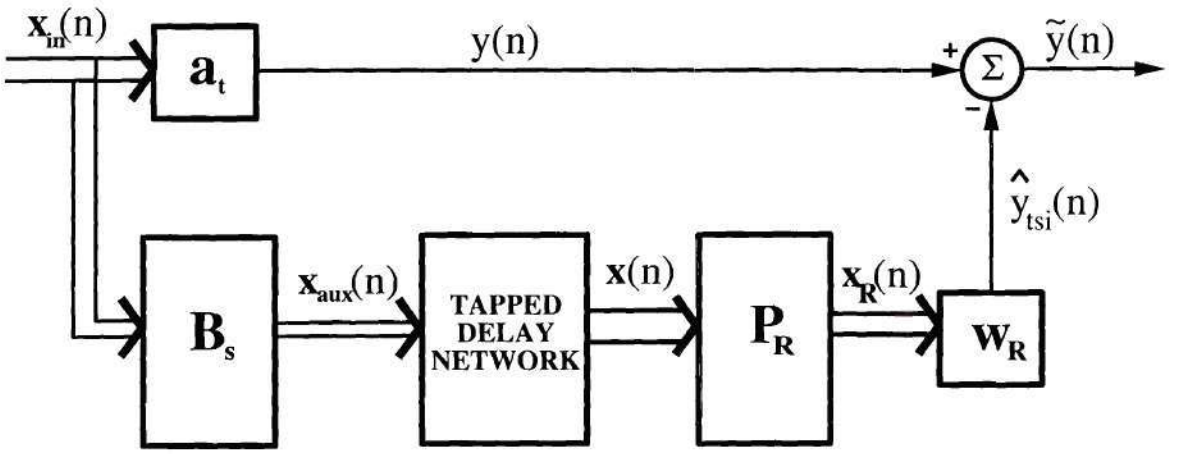

Figure 4.2: Reduced rank beamspace TSI canceler.

smallest). Recall that the thermal sensor noise is assumed to be uncorrelated in both space and time. The eigenvalues contain both interference and noise contributions. If σ_n^2 is the thermal noise power and β_k are the eigenvalues of $\mathbf{R_{tsi}}$ in descending order, then

$$\begin{aligned} \lambda_k &= \beta_k + \sigma_n^2 \\ &= \begin{cases} \beta_k + \sigma_n^2 & k \leq R \\ \sigma_n^2 & k > R \end{cases} \end{aligned} \tag{4.11}$$

since $\beta_k = 0$ for $k > R$, i.e. for the noise eigenvalues. The inverse of the covariance matrix is

$$\mathbf{R_x^{-1}} = \sum_{k=1}^{K_F} \frac{1}{\lambda_k} \mathbf{v_k} \mathbf{v_k^H} \tag{4.12}$$

and the resulting prediction of the mainbeam TSI signal is found by applying the adaptive weights to the signal prediction vector

$$\begin{aligned}
\hat{y}_{tsi}(n) &= \mathbf{w}_{\mathbf{bs}}^H \mathbf{x}(n) \\
&= \left(\mathbf{R}_{\mathbf{x}}^{-1} \mathbf{r}_{\mathbf{xy}}\right)^H \mathbf{x}(n) \\
&= \left(\sum_{k=1}^{K_F} \frac{1}{\lambda_k} \mathbf{v_k} \mathbf{v_k}^H \mathbf{r}_{\mathbf{xy}}\right)^H \mathbf{x}(n) \\
&= \sum_{k=1}^{K_F} \frac{\mathbf{r}_{\mathbf{xy}}^H \mathbf{v_k}}{\lambda_k} \mathbf{v_k}^H \mathbf{x}(n) \ .
\end{aligned} \tag{4.13}$$

Consequently, the MMSE interference prediction filter is seen to contain a filter bank comprised of filters equal to the eigenvectors $\mathbf{v_k}$ of the signal prediction vector covariance matrix $\mathbf{R_x}$. The filter bank of eigenvectors interpretation of the MMSE Wiener filter is shown in Fig. 4.3. The outputs of the eigenvector filters, or eigenfilters, are weighted by the constants

$$c_k = \frac{\mathbf{r}_{\mathbf{xy}}^H \mathbf{v_k}}{\lambda_k} \tag{4.14}$$

and the resulting MMSE estimate of the interference is subtracted from the upper branch signal

$$\begin{aligned}
\tilde{y}(n) &= y(n) - \hat{y}_{tsi}(n) \\
&= y(n) - \sum_{k=1}^{K_F} c_k \mathbf{v_k}^H \mathbf{x}(n) \ .
\end{aligned} \tag{4.15}$$

The reason the outputs of each eigenvector filter can be simply added, rather than taking cross-correlation terms into account as in the Wiener-Hopf equation in (4.9), is that the outputs of the eigenfilter bank are uncorrelated. This bank of eigenfilters can be thought of as a decorrelating transform that isolates the individual sources of interference. The coefficients, $\{c_k\}$, normalize the outputs of each eigenfilter to have a power of one and weight them by the amount of cross-correlated energy from the mainbeam signal projected onto the respective eigenvector ($\mathbf{r}_{\mathbf{xy}}^H \mathbf{v_k}$). Since the set of eigenvectors $\{\mathbf{v_k}\}$ forms a basis for the K_F dimensional space, the dot product with the cross-covariance vector $\mathbf{r_{xy}}$ is simply its representation using the normalized

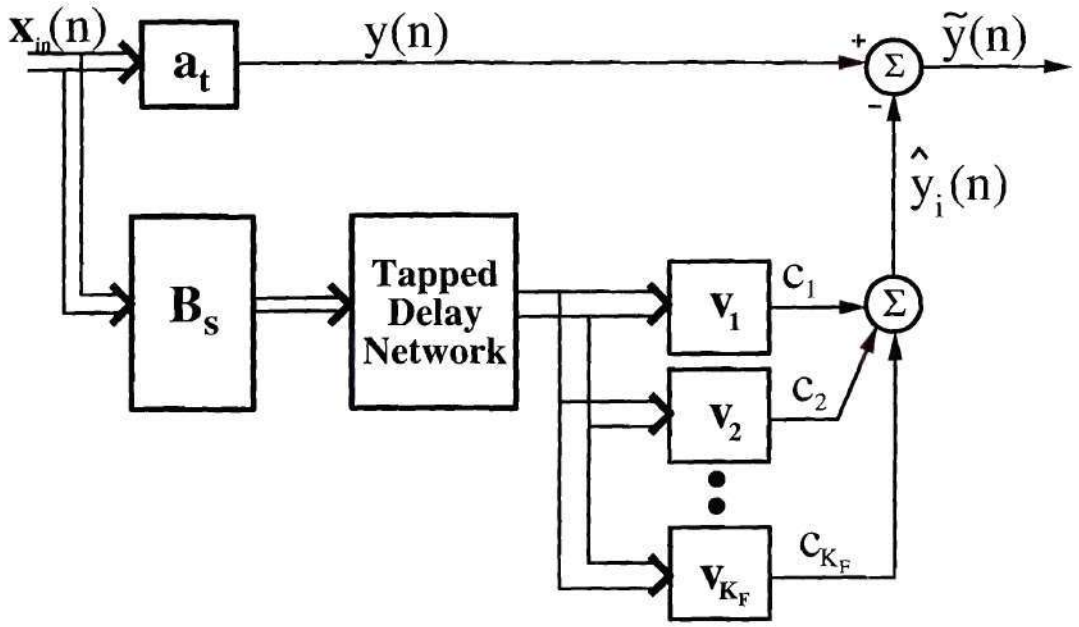

Figure 4.3: Beamspace TSI canceler with filter bank of eigenvectors.

eigenvector basis, i.e.,

$$\mathbf{r_{xy}} = \sum_{k=1}^{K_F} \left(\mathbf{v_k^H r_{xy}}\right) \mathbf{v_k} \ . \tag{4.16}$$

4.1.2 Eigenvector Based Rank Reduction Methods

The eigendecomposition of the signal prediction vector covariance matrix in (4.10) isolates all of the sources contributing to the mainbeam interference into individual eigenvectors $\mathbf{v_k}$ with their associated power levels (i.e., eigenvalues λ_k). Applying a transform equal to the matrix of eigenvectors decorrelates the components of the adaptive filter and allows the weights of the individual components to be computed independently of one another as was shown in the previous section and in Fig. 4.3. In the full rank case, this operation combined with the proper weighting of each component from (4.14) provides the solution to the Wiener-Hopf MMSE equation. However,

rank reduction strategies can be devised by choosing a subset of the eigenvectors of the covariance matrix which equates to the zero weighting of certain branches in the filter bank of eigenvectors in Fig. 4.3. Note that, computationally speaking, such rank reduction strategies achieve little, if any, savings since the solution of the full rank Wiener-Hopf equation requires the same order of computation as the full eigendecomposition. However, these methods are still viable means of reducing the required sample support in reasonably stationary environments in which the rank reduction subspace projection does not have to be continually updated. In the case where the rank of the canceler exceeds the rank of the interference, the eigendecomposition provides a means of separating the interference subspace from the thermal noise subspace.

Principal Components

Recall from (4.11) that the eigenvalues λ_k of $\mathbf{R_x}$ are made up of the sum of the power of the associated interference source β_k and the sensor thermal noise σ_n^2. Therefore, the R largest eigenvalues identify the sources of interference and their corresponding eigenvectors span the associated subspace. The remaining eigenvectors identify a thermal noise subspace containing no relevant information for mainbeam TSI cancellation. One proposed rank reduction strategy suggests retaining the eigenvectors corresponding to the largest eigenvalues and is sometimes referred to as principal components rank reduction [52, 62, 64]. The principal components rank reduction projection matrix is

$$\mathbf{P_R} = [\mathbf{v_1}\ \mathbf{v_2}\ \cdots\ \mathbf{v_{K_R}}]\ . \tag{4.17}$$

Recall that the eigenvector-eigenvalue pairs $\{\mathbf{v_k}, \lambda_k\}$ are ordered in terms of decreasing eigenvalues. If the reduced rank K_R exceeds the rank of the interference, i.e., $K_R \geq R$, the reduced rank processor will have the same performance as its full rank counterpart [52].

Cross-Spectral Metric

Instead of choosing the largest eigenvalues corresponding to the strongest interference sources, consider the sources that produce the most interference energy in the mainbeam signal $y(n)$. By choosing the eigenvectors associated with these eigenvalues for the rank reduction projection matrix, the processor removes the largest contributors to the mainbeam interference. For example, the strongest interference source might actually fall in a null of the beampattern for the non-adaptive mainbeam steering vector $\mathbf{a_t}$ and therefore produces no mainbeam interference and serves no use to the adaptive canceler. Consider the MMSE output of the beamspace TSI canceler

$$\sigma_{\tilde{y}}^2 = \sigma_y^2 - \mathrm{E}\left\{|\hat{y}_{tsi}(n)|^2\right\} \tag{4.18}$$

where $\sigma_{\tilde{y}}^2 = \mathrm{E}\left\{|\tilde{y}(n)|^2\right\}$ is the canceler output power and $\sigma_y^2 = \mathrm{E}\left\{|y(n)|^2\right\}$ is the power of the mainbeam signal prior to cancellation. Since the adaptive predictor finds the MMSE estimate of the mainbeam interference, the associated power removed is

$$\begin{aligned} \mathrm{E}\left\{|\hat{y}_{tsi}(n)|^2\right\} &= \mathbf{r}_{\mathbf{xy}}^H \, \mathbf{R}_{\mathbf{x}}^{-1} \, \mathbf{r}_{\mathbf{xy}} \\ &= \mathbf{r}_{\mathbf{xy}}^H \sum_{k=1}^{K_F} \frac{1}{\lambda_k} \mathbf{v_k} \mathbf{v_k}^H \mathbf{r}_{\mathbf{xy}} \\ &= \sum_{k=1}^{K_F} \frac{\left|\mathbf{r}_{\mathbf{xy}}^H \mathbf{v_k}\right|^2}{\lambda_k} \, . \end{aligned} \tag{4.19}$$

The quantity given by

$$\gamma_k = \frac{\left|\mathbf{r}_{\mathbf{xy}}^H \mathbf{v_k}\right|^2}{\lambda_k} \tag{4.20}$$

is referred to as the *cross-spectral metric* [25]. From (4.19), the greatest amount of interference is cancelled from the mainbeam by those eigenvectors associated with the largest cross-spectral metrics. In terms of choosing eigenvectors for $\mathbf{P_R}$, the cross-spectral metric is optimum in the MMSE sense [10, 25]. Therefore, reordering the eigenvectors according to the largest cross-spectral metrics in (4.20), the rank reduction projection matrix is

$$\mathbf{P_R} = \left[\mathbf{v_{k'(1)}} \; \mathbf{v_{k'(2)}} \; \cdots \; \mathbf{v_{k'(K_R)}}\right] \tag{4.21}$$

where $k'(1)$ is the index of the largest cross-spectral metric eigenpair, $k'(2)$ the one for the second largest, and so on. There are two other things worth pointing out about the cross-spectral metric. First, the cross-spectral metric criterion is only superior to principal components when the reduced rank is below the rank of the interference. Otherwise, the two approaches yield identical results. Second, the cross-spectral metric is optimum in the MMSE sense for choosing the projection matrix only when $\mathbf{P_R}$ is confined to consist of eigenvectors. Should this restriction be removed, it is possible to find a projection matrix with better MMSE performance. In fact, the performance of the full rank case can be achieved for any reduced rank if the full rank MMSE adaptive weight vector $\mathbf{w_{bs}}$ is contained in the subspace spanned by the columns of the rank reduction projection matrix [55].

4.1.3 Cross-Covariance Based Rank Reduction Methods

In this section, two methods are given that perform rank reduction based on the elements of the cross-covariance vector $\mathbf{r_{xy}}$ in (4.9). In contrast to the eigendecomposition methods discussed in Section 4.1.2, both are implemented prior to the computation and inversion of the covariance matrix and only require $\mathbf{r_{xy}}$. As a result, both methods are much less computationally intensive.

Cross-Covariance Thresholding

Recall that TSI is produced by weighted, delayed replicas of the original jammer waveform whose samples are approximately uncorrelated. Therefore, the TSI signal is correlated with samples over an interval of the jammer source waveform, assumed to be a broadband (approximately white) noise signal. The number of samples in this interval is the rank of the mainbeam interference. In order to achieve suppression to the thermal noise floor, the full rank adaptive canceler must observe the samples on the contributing interval. However, if a slight loss in performance can be tolerated, then a reduced rank processor can be employed. Note that it should be possible to

reduce the rank to a certain level without a significant loss in performance since the different delays on the interval do not all contribute equally to the overall TSI signal. Each delay is due to the difference in propagation paths associated with the various scatterers which inevitably do not produce the same amount of reflected energy in the mainbeam signal $y(n)$. Therefore, if the lesser contributors are not used by the adaptive processor, there is a modest penalty in terms of residual interference. One possible means of implementing such a strategy is to threshold the full rank cross-covariance vector. The components of the signal prediction vector $\mathbf{x}(n)$ corresponding to the elements of $\mathbf{r_{xy}}$ with the largest magnitudes are chosen for the reduced rank adaptive processor. With this approach, the projection matrix $\mathbf{P_r}$ becomes a sparse cross-covariance selection matrix with columns equal to $\mathbf{e_k}$, a $K_F \times 1$ vector with all elements equal to zero except the kth element which equals one

$$\mathbf{e_k} = \begin{bmatrix} 0 \cdots 0 & 1 & 0 \cdots 0 \\ & \uparrow & \\ & k\text{th element} & \end{bmatrix}^T . \tag{4.22}$$

When applied to the signal prediction vector, the vector $\mathbf{e_k}$ selects the kth element of $\mathbf{x}(n)$. The rank reduction projection matrix becomes

$$\mathbf{P_R} = \left[\mathbf{e_{k'(1)}}\ \mathbf{e_{k'(2)}}\ \cdots \mathbf{e_{k'(K_R)}}\right] \tag{4.23}$$

where the index $k'(1)$ corresponds to the element of $\mathbf{r_{xy}}$ with the largest magnitude, $k'(2)$ the second largest, and so on.

Normalized Cross-Covariance Thresholding

Although the cross-spectral metric is clearly superior to principal components, the requirement of a full eigendecomposition may still be too imposing for real-time use. However, it is possible to approximate the cross-spectral metric by choosing another set of basis vectors in place of the eigenvectors. The requirement on the alternate basis vectors is that they reasonably decorrelate the individual interference sources, i.e., that the basis vectors approximate the actual eigenvectors. Consider the beamspace

TSI canceler in Fig. 4.1, where the blocking matrix $\mathbf{B_s}$ in the lower branch is responsible for forming the $(M-1)$ auxiliary beams. The blocking matrix approximately isolates the individual TSI signals within beams according to their directions of arrival. The level of spatial decorrelation between beams improves as the number of elements in the array is increased [48]. Since the auxiliary beam signals have already been transformed into beamspace, the approximation to the cross-spectral metric is obtained by replacing $\mathbf{v_k}$ with $\mathbf{e_k}$ in (4.20) and choosing the unit vectors $\mathbf{e_k}$ that maximize

$$\xi_k = \frac{\left|\mathbf{r}_{\mathbf{xy}}^H \mathbf{e_k}\right|^2}{\sigma_m^2} = \frac{|\mathbf{r_{xy}}(k)|^2}{\sigma_m^2} , \tag{4.24}$$

where σ_m^2 is the signal power of the mth beam and $\mathbf{r_{xy}}(k)$ is the kth element of the cross-covariance vector. The signal power of the mth beam is used to approximate the eigenvalue in the cross-spectral metric because the eigenvalue measures the power projected onto its companion eigenvector and the power within each beam is equal at all delays. Note that this metric is very similar to the one used to perform cross-covariance based rank reduction except the elements of $\mathbf{r_{xy}}$ are normalized by the power in their corresponding beams. The projection matrix $\mathbf{P_R}$ is again a sparse selection matrix, as in (4.23), that selects the elements of $\mathbf{x}(n)$ corresponding to the elements of $\mathbf{r_{xy}}$ that maximize (4.24).

4.2 Experimental Results

The various rank reduction strategies were applied to experimental data collected as part of the DARPA/Navy Mountaintop program [40, 61] in order to study their performance for TSI mitigation purposes. The TSI data was produced by a ground-based jammer and collected with a ground-based receiver (Mountaintop file `mmit004v1.mat`). The first two experiments compare the performance of the four rank reduction methods: cross-spectral metric (solid line), principal components (+ line), normalized cross-covariance thresholding (dashed line), and cross-covariance

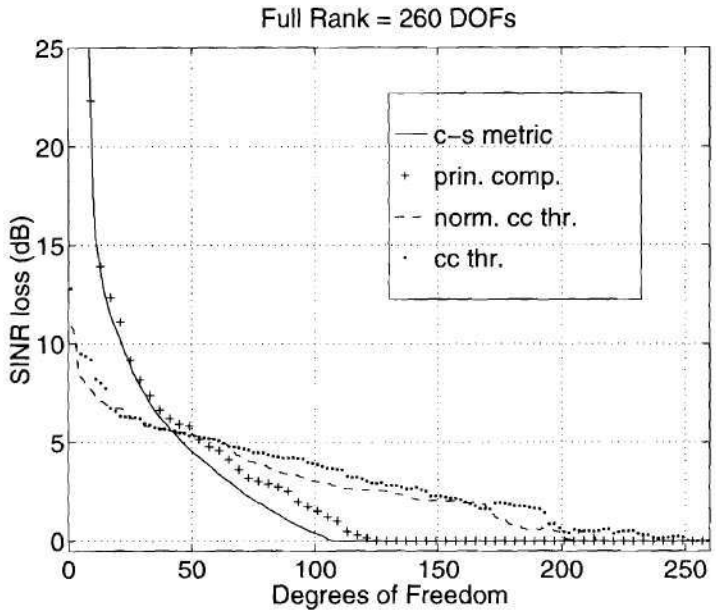

Figure 4.4: Rank reduction results, SINR vs. degrees of freedom (full rank is 260 degrees of freedom).

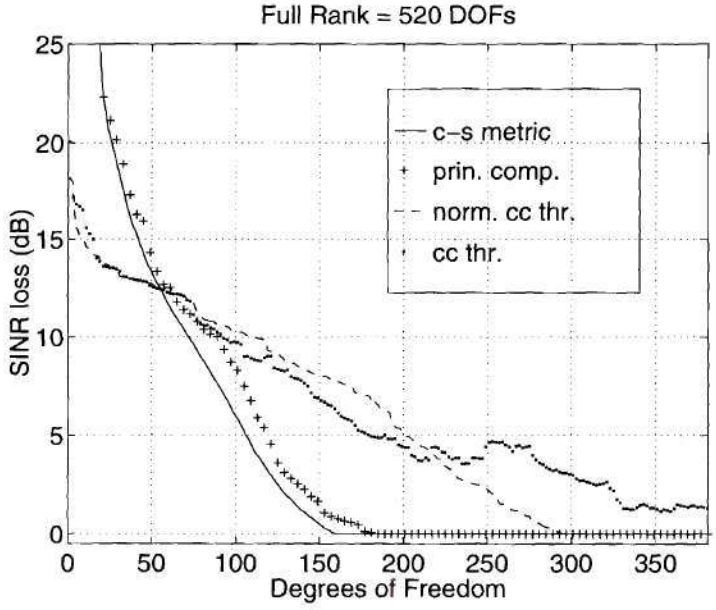

Figure 4.5: Rank reduction results, SINR vs. degrees of freedom (full rank is 520 degrees of freedom).

thresholding (dotted line). Rank reduction results are shown where the full rank was set to 260 and 520 degrees of freedom in Figs. 4.4 and 4.5, respectively. The performance criterion used is the loss in SINR, i.e., the difference in residual interference after and before rank reduction, and is plotted versus the adaptive degrees of freedom of the reduced rank processor. In both cases, the cross-spectral metric is shown to outperform principal components for all degrees of freedom, achieving full rank performance after about 100 and 150 degrees of freedom for the two different full rank cases. The two cross-covariance based methods actually outperform the eigendecomposition based methods for low ranks ($r < 50$). In this case, the subspace dimension is much smaller than the rank of the interference. The subspaces determined by the cross-covariance based methods are not limited to individual sources as with the decorrelating eigendecomposition based methods. This result confirms that these eigendecomposition based methods are not necessarily optimum if the restriction of covariance matrix eigenvectors is relaxed for the selection of the rank reduction projection matrix. In general, the cross-covariance based methods have similar performance and are within 5 dB of full rank performance after 50 and 200 degrees of freedom for the two experiments, a rank reduction of greater than 50%.

The next set of experiments compares the performance of a full rank processor with an equivalent rank processor obtained by rank reduction on a larger full rank processor. The same set of data was used with the full rank set to 260 and 520 for the reduced rank processors. The results are shown in terms of residual interference-to-noise ratio (INR) in Figs. 4.6 and 4.7. The solid line is the full rank processor and the dashed and dotted lines are the reduced rank processors using the cross-spectral metric and the normalized cross-covariance, respectively. Note that the full rank processor cannot match the performance of either rank reduction method for more than 50 degrees of freedom. Intuitively, the reduced rank processors have more components to choose from and are therefore able to select the more crucial information.

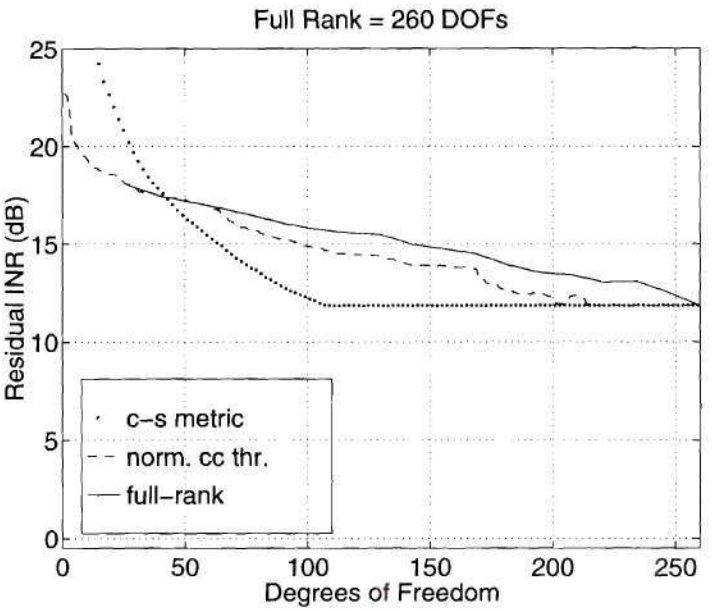

Figure 4.6: Reduced rank (with full rank of 260 degrees of freedom) vs. full rank results.

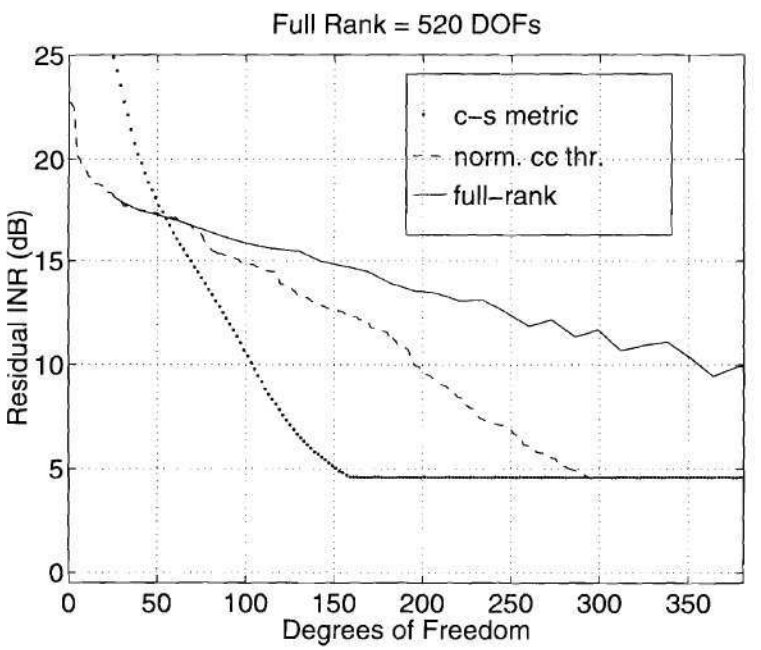

Figure 4.7: Reduced rank (with full rank of 520 degrees of freedom) vs. full rank results.

4.3 Conclusions

This chapter has demonstrated the utility of properly applied rank reduction methods. The reduced rank processors need less computation and have the advantage of a smaller sample support requirement. Four methods were presented, two based on eigendecompositions and two based on cross-covariance vector thresholding, and all were demonstrated on experimental TSI data. Although the eigenvector methods usually have better performance in terms of residual SINR, they are much more computationally intensive, requiring almost the same amount of computation as the full rank processor. Of the two, the cross-spectral metric was demonstrated to be a more appropriate means of selecting eigenvectors for the rank reduction projection matrix. In addition, the eigendecomposition based methods are not always optimum in terms of MMSE. The results with the experimental TSI data showed that the two cross-covariance methods outperform the eigenvector methods for low ranks. Even for the higher ranks at which the eigenvector methods achieved better cancellation, the slight drop-off in performance associated with the cross-covariance methods might be tolerated given the tremendous amount of computational savings.

CHAPTER 5

Factored Processing for Combined TSI and Monostatic Clutter Mitigation

The subject of this chapter is the mitigation of interference consisting of both terrain scattered interference (TSI) and monostatic ground clutter. The proposed cancellation architecture is a combination of the beamspace TSI canceler, introduced in Chapter 3, and the space-time adaptive processing (STAP) for canceling monostatic clutter, as discussed in Chapter 2. The resulting processor has adaptivity in the element-space, PRI, and range domains. Note that this scenario is more likely to occur than TSI alone because the airborne radar is primarily in active mode, transmitting in order to detect targets. As a result, terrain is illuminated by the radar and the corresponding reflections produce monostatic clutter returns in the radar system.

The chapter begins with a discussion of the problem, along with a brief review of the characteristics of TSI and monostatic clutter. Next, the motivation for factored processing is discussed. Several issues relating to TSI mitigation in the presence of clutter are treated, followed by a description of the proposed algorithm: factored full beamspace TSI/STAP. For comparison, an alternate method is described, namely, factored beamspace TSI/MTI processing. Finally, experimental results comparing the two techniques are given, followed by some concluding remarks.

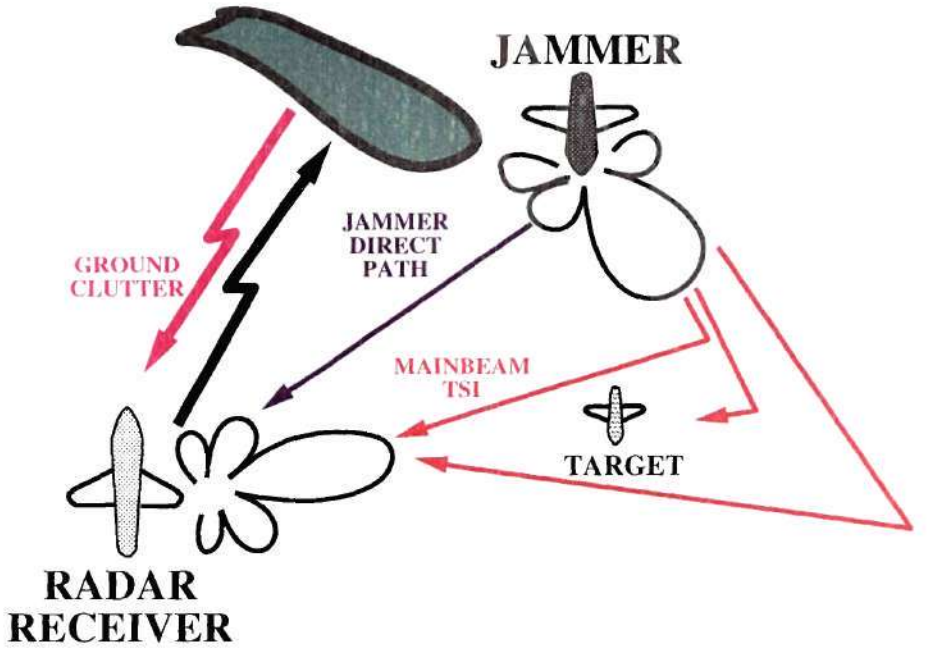

Figure 5.1: Scenario with both TSI and monostatic clutter interference.

5.1 Problem Statement

The scenario of combined TSI and monostatic clutter interference is shown in Fig. 5.1. The overall interference presented to the radar receiver consists of both TSI and monostatic clutter returns, produced by terrain reflections of the jammer and the radar's own signals, respectively. Thus, the CPI interference $LM \times 1$ signal vector has both TSI and monostatic clutter components and is given by

$$\mathbf{z_i}(n) = \mathbf{z_{tsi}}(n) + \mathbf{z_c}(n) \tag{5.1}$$

where $\mathbf{z_{tsi}}(n)$ and $\mathbf{z_c}(n)$ are the TSI and monostatic clutter components, respectively. Likewise, the $M \times 1$ PRI interference signal vector is

$$\mathbf{x_i}(n) = \mathbf{x_{tsi}}(n) + \mathbf{x_c}(n) \tag{5.2}$$

where $\mathbf{x_{tsi}}(n)$ and $\mathbf{x_c}(n)$ are the TSI and monostatic clutter PRI signal vectors, respectively.

As discussed in detail in Chapter 2, TSI is produced by the terrain reflections of a stand-off barrage noise jammer [19]. Recall from Chapter 2 that the TSI received from each azimuth angle is

$$x_{tsi}(t,\phi) = \int_0^{T_{tsi}} h(\tau,\phi) x_j(t-\tau) d\tau \tag{5.3}$$

where $x_j(t)$ is the continuous-time signal transmitted by the jammer, T_{tsi} is the maximum delay in the TSI signal (range extent), and $h(t,\phi)$ is the complex weighting of the TSI signal as a function of delay and angle ϕ. The weighting function $h(t,\phi)$ incorporates the antenna pattern of the jammer and the terrain reflections. The overall TSI signal at the radar receiver array is the result of projecting the TSI signals from all azimuth angles onto the array manifold

$$\mathbf{x_{tsi}}(t) = \int_{-\pi}^{\pi} x_{tsi}(t,\phi) \cdot \mathbf{a}(\phi) d\phi \tag{5.4}$$

where $\mathbf{a}(\phi)$ is the phase-centered steering vector from (2.7) for azimuth angle ϕ or spatial frequency $u = \frac{d}{\lambda}\sin\phi$. The discrete-time TSI signal $\mathbf{x_{tsi}}(n)$ is obtained by sampling its continuous-time counterpart from (5.4) where N samples are collected for each PRI. The TSI signal for an entire CPI, $\mathbf{z_{tsi}}(n)$, is formed by stacking the TSI signals from the individual PRIs (L total).

Mitigation techniques exploit spatial and range correlations in the TSI in order to suppress the mainbeam interference. PRI processing alone cannot achieve TSI cancellation because TSI returns are uncorrelated from one PRI to the next. In addition, the adaptive weights for TSI mitigation have to be recomputed for each PRI because the environment is non-stationary, particularly when TSI is produced by an airborne jammer. The general TSI mitigation processor is shown in Fig. 5.2. In the case of the algorithm given in Chapter 3, the cancellation is performed in the beamspace/range domains. The adaptive filter predicts the TSI signals present in the

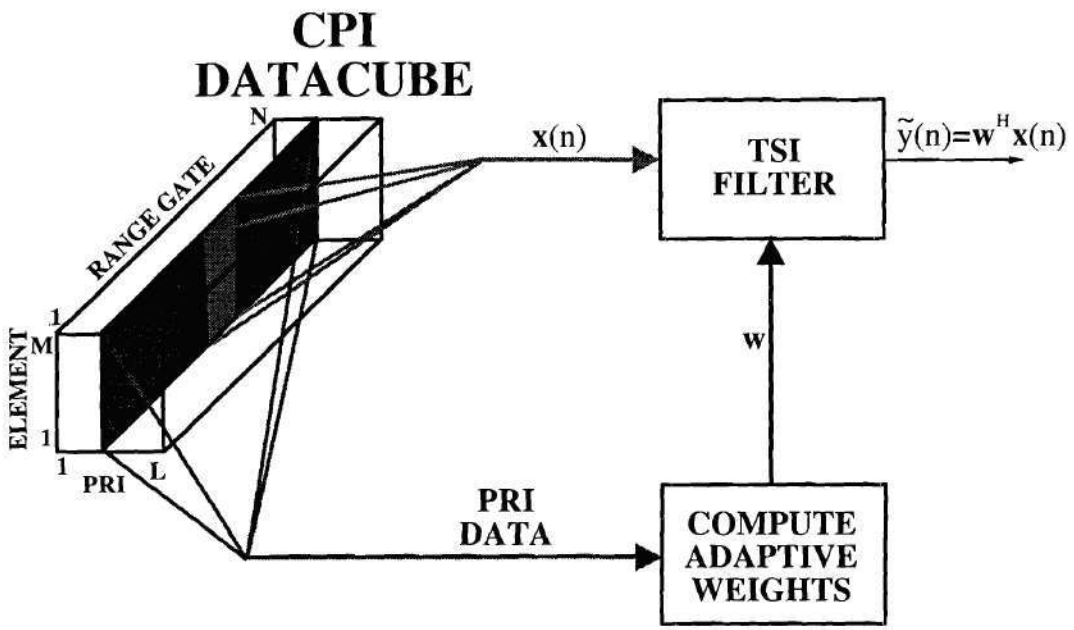

Figure 5.2: TSI mitigation processing.

mainbeam (direction-of-look) using an observation window of range samples over all of the available spatial degrees of freedom (elements or beams). The adaptive weights are computed from a training interval made up of a subset of the PRI.

Monostatic clutter returns, on the other hand, are produced by ground or terrain reflections of the signal transmitted by the airborne surveillance radar [57]. Recall that for monostatic clutter there is a unique relationship between spatial frequency, u, and normalized Doppler frequency $\bar{f}$

$$\bar{f} = \beta u \tag{5.5}$$

where β is given by (2.25). Therefore, the monostatic clutter CPI signal vector is the result of clutter from all azimuth angles and is given by

$$\mathbf{z_c}(n) = \int_{-\pi}^{\pi} \sigma_c(n,\phi)\mathbf{s}(\phi)d\phi \tag{5.6}$$

where $\sigma_c(n, \phi)$ is the unknown surface scattering function at the range cell n. The space-time steering vector $\mathbf{s}$ is the Kronecker product of the Doppler and spatial steering vectors from (2.7) and (2.10)

$$\mathbf{s}(\phi) = \mathbf{s}(u, \bar{f}) = \mathbf{b}(\beta u) \otimes \mathbf{a}(u) \ . \tag{5.7}$$

where u is spatial frequency and $\bar{f}$ is normalized Doppler frequency. Therefore, the signal in (5.6) is produced by integrating in space and time along the clutter ridge, determined by β, on which the monostatic clutter returns lie.

In the case of monostatic clutter, both frequencies, u and $\bar{f}$, are uniquely determined by the azimuth angle ϕ. See Chapter 2, Section 2.2.3 for details. Since the target and clutter are at different spatial locations and/or Doppler frequencies [35], cancellation is performed in the spatial and PRI domains as opposed to the spatial and range domains used to mitigate TSI. The generic space-time clutter canceler is shown in Fig. 5.3. This type of processing is often referred to as space-time adaptive processing (STAP) [67] and has been discussed in Chapter 2. A training interval around the range cell of interest is used to compute the adaptive weights [67]. Typically, a guard band is set up around the presumed target range that excludes the neighboring samples from the adaptive weight computation. Since, the target signal may leak into these range cells, the guard band helps to prevent target signal cancellation [67].

Monostatic clutter is produced by terrain reflections. As a result, the corresponding returns are subject to large fluctuations coinciding with the terrain characteristics. Regions where the clutter is approximately stationary tend to be small, in some cases as little as 20 kilometers [40, 61]. Since STAP makes the assumption that the samples have invariant statistics [8, 67], the amount of data available for training is limited by the amount of stationary clutter returns available in the region of the assumed target range.

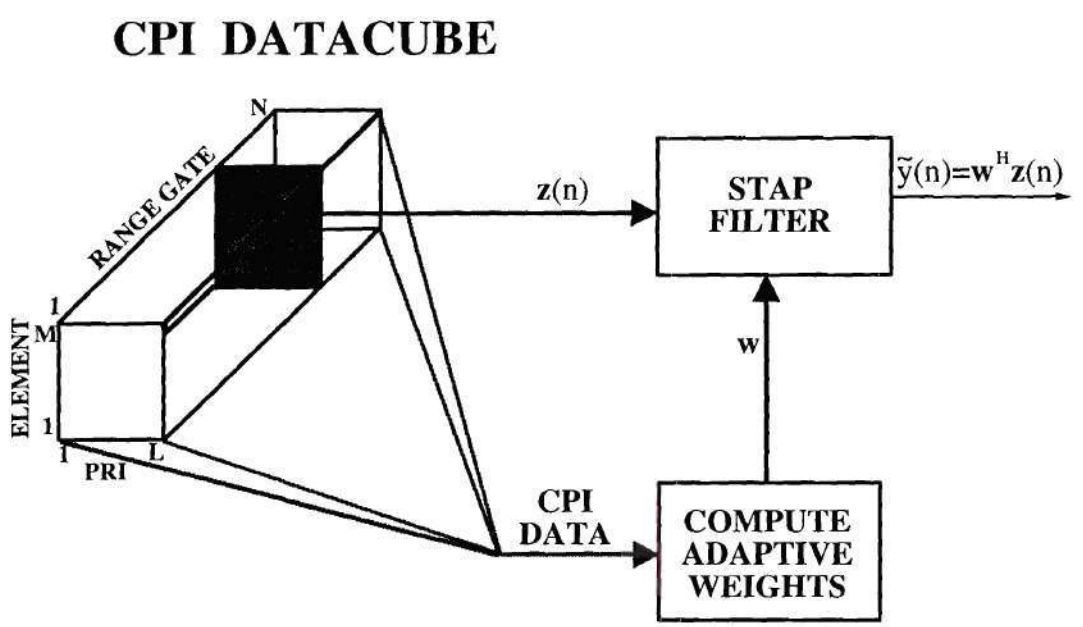

Figure 5.3: Space-time adaptive processing for monostatic clutter mitigation.

5.2 Factored Mitigation: Discussion

The combined mitigation of TSI and monostatic clutter involves processing in three dimensions: element, PRI, and range. Fully adaptive 3-D processing is theoretically possible, but it requires an adaptive processor with degrees of freedom equal to

$$N_{dof} = L \cdot M \cdot N_{bs} \tag{5.8}$$

where L is the number of PRIs, M is the number of elements in the array, and N_{bs} is the number of range samples used by the adaptive canceler. However, 3-D adaptive processing is not always feasible. Due to sample support limitations imposed by non-stationarities in the returns as well as computational restrictions, processing resources can be limited and, consequently, may not be able to support 3-D processing.

The typical adaptive processor seeks to minimize the output power subject to certain constraints designed to preserve the target. In practice, the linearly con-

strained minimum variance (LCMV) processor is implemented using the sample matrix inversion (SMI) method [54] which estimates covariance statistics from the sample data. Since the sample covariance matrix is the maximum-likelihood estimate of the actual covariance matrix, it will converge as the number of independent realizations, N_t, approaches infinity. However, an infinite number of realizations is never available and the resulting weight vector is always sub-optimal. The recommended number of snapshots for acceptable performance (within 3 dB of optimal performance) is [54]

$$N_t > 2K_F - 3 \tag{5.9}$$

where K_F is the degrees of freedom of the adaptive processor. However, the sample support available for the estimation of the covariance statistics is generally not large enough to satisfy (5.9). In practice, most terrain tends to be rapidly changing, leading to small regions over which the monostatic clutter returns are approximately stationary. As a result, the number of samples available is typically less than the degrees of freedom of the adaptive processor from (5.8) which is far below the minimum requirement in (5.9).

A possible solution is to factor the processing into two stages [45, 39]: TSI mitigation followed by monostatic clutter cancellation. The order of processing is influenced by the nature of the actual data. TSI returns are present throughout the PRI, whereas significant monostatic clutter returns are predominantly in the closer range cells [57]. As a result, the weights for the TSI mitigation adaptive processor should be estimated using a "clutter-free" training interval made up of samples at far-field ranges. Following the TSI mitigation, clutter nulling can be performed. A block diagram of the processing time-line is shown in Fig. 5.4.

Now consider the second stage of factored processing for monostatic clutter mitigation. The benefits of spatial processing for monostatic clutter nulling have been demonstrated using STAP [67]. In the absence of spatial processing, monostatic clutter nulling can only be achieved using moving target indicator (MTI) processing which lacks the performance of STAP. However to support STAP, the TSI mitigation

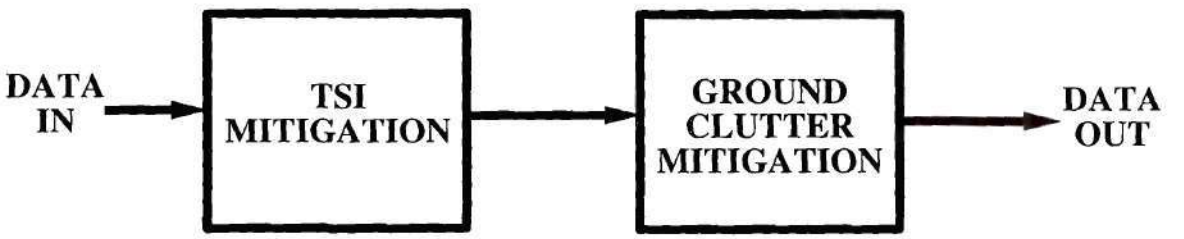

Figure 5.4: Block diagram of factored processing for TSI and monostatic clutter mitigation.

stage must maintain the spatial dimension of the data. In addition, the TSI canceler should preserve the structure of the monostatic clutter, i.e., azimuth and Doppler information. The details of the proposed TSI mitigation method will be covered in Section 5.4. The second portion of the processor is the monostatic clutter canceler. Although a variety of STAP methods exist [67], we restrict ourselves to minimum variance STAP, also known as fully adaptive STAP, and concentrate on the development of a TSI canceler capable of supporting STAP.

5.3 TSI Mitigation Considerations

The TSI mitigation algorithm to be used is the beamspace approach [36, 37], discussed in detail in Chapter 3. The two major considerations for TSI mitigation as part of the factored processor are the selection of a training interval for adaptive weight computation and the effect of TSI mitigation on the monostatic clutter returns. Covariance matrix diagonal loading is proposed as a method of helping to pass the clutter returns through the TSI mitigation with as little distortion as possible.

5.3.1 Training Interval Selection

The issue of the training interval for the computation of the adaptive weights of the TSI canceler was touched upon in the previous section with regard to the sequential

order of factored processing. TSI mitigation is performed independently on individual PRIs. The training interval is the portion of the PRI dedicated to the computation of the adaptive weights of the canceler for the current PRI. In the case of interference made up of both TSI and monostatic clutter, the weights are ideally trained on a "clutter-free" region [22, 46] to minimize the influence of the clutter returns. Note that although the TSI and monostatic clutter PRI signals are uncorrelated with one another, i.e.,

$$\mathrm{E}\left\{\mathbf{x_{tsi}}(n)\mathbf{x_c}(n-k)\right\} = \mathbf{0} \quad \forall k \ , \tag{5.10}$$

the signals nonetheless corrupt each other's sample statistics and, thus, affect the performance of the canceler when a finite number of data samples is available [22]. The use of a "clutter-free" training interval for the computation of the adaptive weights of the TSI canceler helps to mitigate the effects of non-zero cross-correlation terms from finite sample data sets.

TSI returns are found at all ranges, assuming the jammer is continuously transmitting, yet monostatic clutter is limited to ranges close to the radar, known as the near-field. Due to the curvature of the earth, longer ranges do not have terrain in the line-of-sight to the radar receiver [51, 57]. As a result, very little, if any, clutter returns are received from these far-field range cells. Fig. 5.5 shows experimental clutter return signals at one azimuth angle in terms of the clutter-to-noise ratio (CNR). The clutter signal falls below the thermal noise floor (CNR $<$ 0 dB) after about 1200 range cells. Therefore, the best choice for the training interval of the adaptive weights for TSI mitigation is in these far-field range cells that only contain TSI returns.

5.3.2 Diagonal Loading of the Sample Covariance Matrix

Since the cancellation is performed in a two-step process, namely TSI followed by clutter mitigation, it is important to ensure that the clutter interference is not distorted during TSI processing [22]. Ideally, we would like to pass the clutter returns (thick, gray line) unchanged through the beamspace TSI canceler as shown in Fig. 5.6.

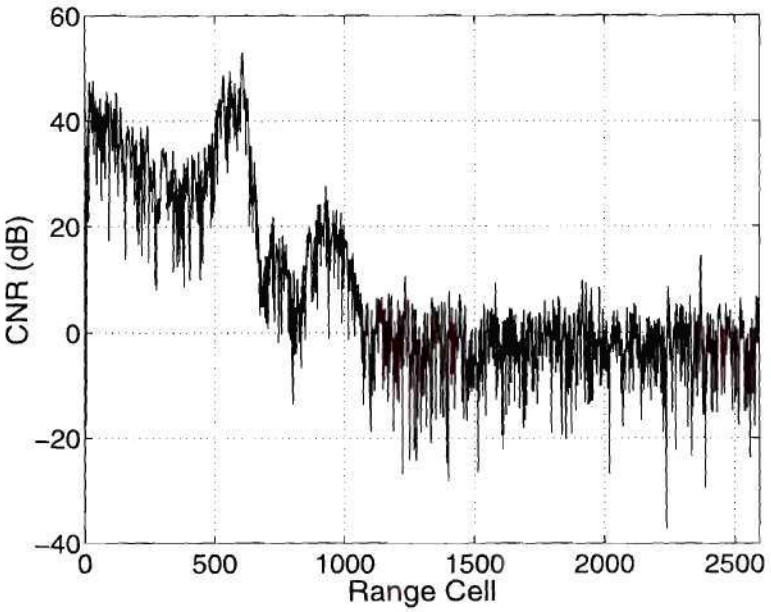

Figure 5.5: Clutter-to-Noise Ratio (CNR) (dB) versus Range Cell for monostatic clutter only. The signal is for $\phi = 0°$ in one PRI.

Therefore, the clutter may be looked upon as a target signal, i.e., pass clutter in the direction-of-look ϕ_t with unity gain and zero phase, while keeping it out of the adaptive predictor in the lower branch using the blocking matrix $\mathbf{B_s}$. However, clutter is not necessarily be at the exact target azimuth angle ϕ_t and, thus, may leak into the lower branch interference predictor. The result is the distortion of the overall monostatic clutter signal output from the TSI canceler. In order to reduce this distortion, the magnitudes of the adaptive weights in the lower branch, $\mathbf{w_{bs}}$, should be minimized. In addition, the frequency response of the adaptive weights is an important issue. The TSI filter should not amplify portions of the spectrum that do not contain TSI, yet potentially contain monostatic clutter.

One approach that helps reduce the amplification/distortion of clutter through TSI mitigation is the diagonal loading of the sample covariance matrix [22] which was covered in Chapter 3. The major source of frequency response distortion in an

adaptive canceler is the sample covariance matrix. Reed, Mallett, and Brennan [54] showed that the number of snapshots required to maintain acceptable performance (within 3 dB of the optimum) with a sample covariance matrix is on the order of twice the degrees of freedom of the adaptive canceler. The fewer snapshots used to estimate the covariance statistics, the worse the estimates of the smaller eigenvalues corresponding to the thermal noise subspace become. As a result, the noise eigenvalues are not equal to but distributed around the true noise power. Although the noise subspace should have no effect on the adaptive canceler, the estimation errors in the noise eigenvalues result in the addition of random eigenvectors to the adaptive weight vector. The frequency response of the adaptive weights suffers severe degradation [12, 23], potentially amplifying portions of the spectrum not associated with interference.

Diagonal loading of the sample covariance matrix adds the loading power to each of the eigenvalues and, if properly chosen, can bring these eigenvalues close to the true thermal noise floor. The cost of diagonal loading is a modest loss in sensitivity to weak interference sources with power near the noise floor. However, the drastic improvement in the frequency response of the adaptive weights easily justifies this minimal drop-off in cancellation performance. The improved frequency response helps to minimize monostatic clutter amplification/distortion. As shown in Chapter 3, the recommended diagonal loading level is at the thermal noise floor power.

5.4 Factored Full Beamspace/Space-Time Adaptive Processing

The motivation behind the use of space-time adaptive processing (STAP) is the performance gain made possible by including spatial adaptivity in the mitigation of monostatic clutter. By exploiting the coupling in space and time, STAP is able to cancel monostatic clutter interference more effectively than Doppler only processing

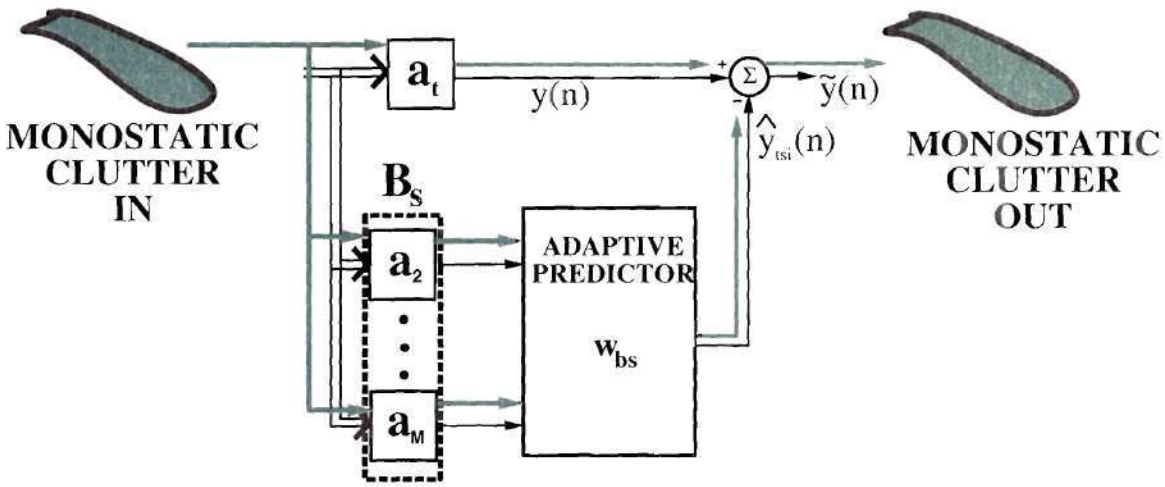

Figure 5.6: The processing of ground clutter returns (thick, green line) through the beamspace TSI canceler.

---

[67]. The cost of this performance gain is an increase in computational cost associated with two-dimensional rather than one-dimensional adaptive processing.

The characteristics of monostatic clutter have been described in detail in Chapter 2 and to a lesser degree at the beginning of this chapter. Clutter returns have a unique relationship in angle and Doppler so that they form a "ridge" in the space-time (PRI) frequency domain. This relationship is illustrated in Fig. 5.7 which shows the azimuth-Doppler spectrum with simulated clutter present across all azimuth angles and Doppler frequencies. In this case, the velocity of the radar receiver aircraft is chosen such that the slope of the clutter ridge is $\beta = 1$. In addition to the clutter ridge, a target is present, isolated to a single point in the 2-D frequency plane (at azimuth $\phi = 5^\circ$ and normalized Doppler frequency $\bar{f}_t = -0.25$). Here, the mainlobe clutter at the same azimuth angle as the target can be cancelled since it is at a distinct Doppler frequency different than that of the target. On the other hand, the clutter at the target Doppler frequency is in the spatial sidelobes of the receiver array so that it can be removed via spatial processing. In fact, the entire clutter ridge can

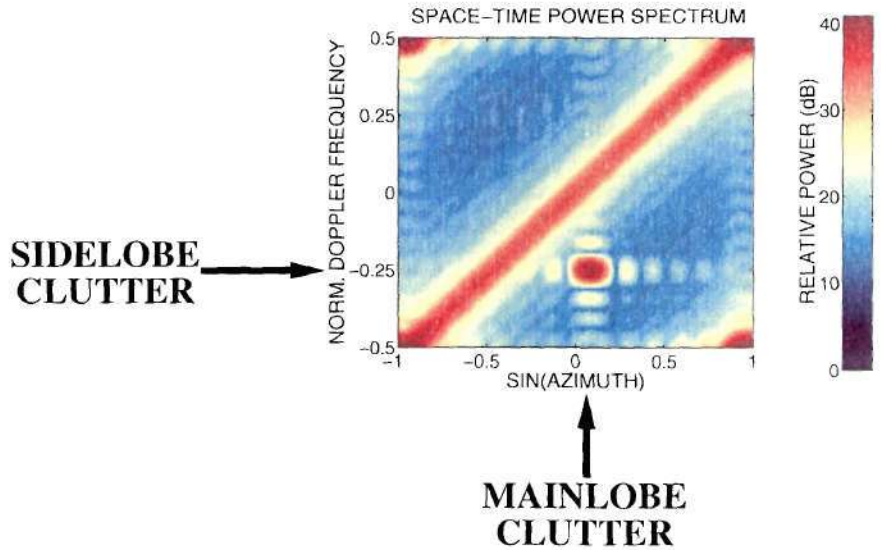

Figure 5.7: Azimuth-Doppler spectrum of simulated monostatic clutter returns and target. The aircraft velocity is chosen so that the slope of the clutter ridge is $\beta = 1$. A target is at azimuth $\phi_t = 5°$ and Doppler frequency $\bar{f}_t = -0.25$.

be effectively nulled by employing STAP [67]. By using the entire azimuth-Doppler frequency plane, STAP is able to simultaneously cancel both mainlobe and sidelobe clutter returns. Note that a full clutter ridge is not typical of actual returns because directional transmission of the radar confines monostatic clutter energy to a portion of the azimuth-Doppler spectrum [40, 61]. Nonetheless, Fig. 5.7 serves to illustrate the potential benefits of STAP.

As outlined in the Section 5.2, the factored processor performs STAP monostatic clutter nulling following TSI mitigation. Therefore, the TSI mitigation stage must preserve the spatial dimension during processing to allow for STAP. The beamspace TSI canceler, shown in Fig. 5.8, operates on one PRI at a time, taking in an M-dimensional PRI signal and producing a 1-D output corresponding to the assumed target direction. In this configuration, the only option for processing the outputs of the TSI canceler from the L PRIs is MTI processing, i.e., Doppler

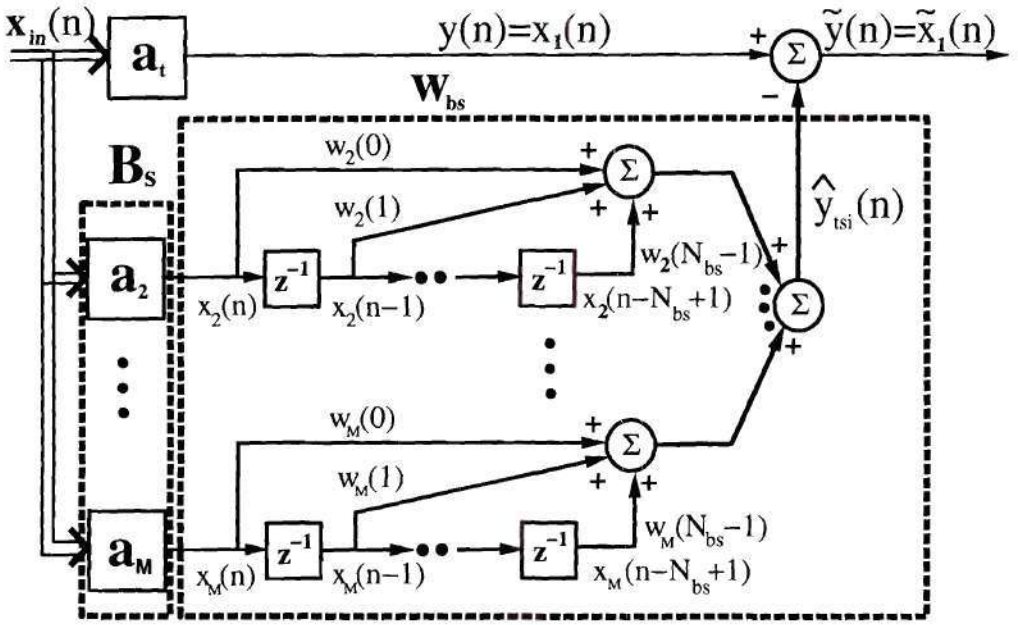

Figure 5.8: Beamspace TSI canceler.

only processing. However, full STAP is possible if TSI mitigation for each PRI is performed on all M orthogonal beams used in the beamspace canceler. The beamspace signals are transformed back into element-space prior to STAP because a transform into beamspace was inherent in the directional constraints used for the TSI processing of the M beams. The TSI-filtered beamspace signals can then be passed on to the STAP algorithm for monostatic clutter nulling. Note that this transform is not necessary when using beamspace/PRI STAP algorithms [67].

5.4.1 Full Beamspace TSI Mitigation

The goal of the overall TSI mitigation routine is to take a CPI data-cube with both TSI and monostatic clutter, remove TSI, and provide an output CPI data-cube with the same dimensions as the input. The subsequent clutter nulling stage can then exploit the full set of spatial degrees of freedom using STAP.

The beamspace TSI canceler [37], shown in Fig. 5.8, operates on the sensor array signal $\mathbf{x_{in}}(n)$ for one PRI. First the returns are non-adaptively, spatially filtered in the assumed target direction ϕ_t. The data vector is projected onto a phase-centered steering vector given by

$$\mathbf{a_t} = \frac{1}{\sqrt{M}} \left[e^{-j2\pi \frac{M-1}{2} u_t} \cdots e^{-j2\pi (\frac{M-1}{2} - m) u_t} \cdots e^{j2\pi \frac{M-1}{2} u_t} \right]^T \tag{5.11}$$

where u_t is the spatial frequency of the target given by

$$u_t = \frac{d}{\lambda} \sin \phi_t \ . \tag{5.12}$$

The inter-element spacing and the wavelength of the radar operating frequency are d and λ, respectively. The PRI signal $\mathbf{x_{in}}(n)$ is also passed through the beamspace blocking matrix which projects the PRI input signal onto the subspace orthogonal to the upper branch steering vector $\mathbf{a_t}$. The blocking matrix $\mathbf{B}$ is made up of spatial steering vectors as in (5.11) at the spatial frequencies corresponding to steering vectors orthogonal to $\mathbf{a_t}$

$$u_m = u_t + \frac{1}{M} \ , \cdots , \ u_t + \frac{m-1}{M} \ , \ , \ u_t + \frac{M-1}{M} \tag{5.13}$$

where $m = 2, 3, \ldots, M$. Therefore, the blocking matrix is

$$\mathbf{B} = [\mathbf{a}(u_2) \ \cdots \ \mathbf{a}(u_m) \ \cdots \ \mathbf{a}(u_M)] \tag{5.14}$$

where the columns of $\mathbf{B}$ are mutually orthogonal. Since the columns of $\mathbf{B}$ are steering vectors as well, the outputs of the blocking matrix are signals representing returns from other azimuth angles $\phi_m = \frac{\lambda}{d} \arcsin(u_m)$, i.e., beamspace signals. If we set $u_1 = u_t$, the steering vector is

$$\mathbf{a}(u_1) = \mathbf{a_t} \ . \tag{5.15}$$

This vector together with the blocking matrix makes up a beamspace transform matrix

$$\begin{aligned} \mathbf{T} &= [\mathbf{a_t} \ \ \mathbf{B}] \\ &= [\mathbf{a}(u_1) \ \ \mathbf{a}(u_2) \ \ \ldots \ \ \mathbf{a}(u_M)] \end{aligned} \tag{5.16}$$

which is unitary ($\mathbf{T}^H \mathbf{T} = \mathbf{I}$) and performs a transformation from element to beamspace [48].

The beamspace TSI canceler from Fig. 5.8 is an implementation of a LCMV processor in a generalized sidelobe canceler (GSC) structure. The upper branch signal is obtained by non-adaptively filtering the PRI input signal by the assumed target direction constraint

$$\begin{aligned} y(n) &= x_1(n) \\ &= \mathbf{a}^H(u_1)\,\mathbf{x_{in}}(n)\ . \end{aligned} \tag{5.17}$$

The lower branch signal is the output of the blocking matrix consisting of the $(M-1)$ auxiliary beam signals

$$x_m(n) = \mathbf{a}^H(u_m)\,\mathbf{x_{in}}(n) \tag{5.18}$$

for $m = 2, 3, \ldots M$. The beamspace signal vector is then formed by concatenating the upper and lower branch signals

$$\begin{aligned} \mathbf{x_{bs}}(n) &= \mathbf{T}^H\,\mathbf{x_{in}}(n) \\ &= \begin{bmatrix} x_1(n) \\ x_2(n) \\ \vdots \\ x_M(n) \end{bmatrix}\ . \end{aligned} \tag{5.19}$$

An estimate of the upper branch interference is found by adaptively weighting the lower branch signals $x_m(n)$ at the tapped delays within the range window of the canceler. The tap spacing is uniform with an equal number of taps per beam, N_{bs}. All of the prediction components, i.e., the auxiliary beam signals at the various delays, can be collected as part of a signal prediction vector

$$\mathbf{x}(n) = \begin{bmatrix} \mathbf{x_2}(n) \\ \mathbf{x_3}(n) \\ \vdots \\ \mathbf{x_M}(n) \end{bmatrix}\ . \tag{5.20}$$

The individual component vectors are made up of the auxiliary beam signals at the various delays

$$\mathbf{x_m}(n) = [x_m(n) \ \cdots \ x_m(N - N_{bs} - 1)]^T \ . \tag{5.21}$$

The beamspace adaptive weights are found from the Wiener-Hopf equation [48]

$$\mathbf{w_{bs}} = \mathbf{R_x^{-1}}\, \mathbf{r_{xy}} \ , \tag{5.22}$$

where $\mathbf{R_x} = \mathrm{E}\left\{\mathbf{x}(n)\,\mathbf{x}^H(n)\right\}$ is the signal prediction vector covariance matrix and $\mathbf{r_{xy}} = \mathrm{E}\left\{\mathbf{x}(n)\,y^*(n)\right\}$ is the cross-covariance vector between the signal prediction vector and the upper branch signal.

The estimate of the mainbeam TSI is found by applying the adaptive weights to the signal prediction vector which is subsequently subtracted from the upper branch to obtain the output of the canceler for the first beam

$$\begin{aligned} \tilde{y}(n) \ = \ \tilde{x}_1(n) \ &= \ y(n) - \hat{y}_{tsi}(n) \\ &= \ x_1(n) - \mathbf{w_{bs}^H}\,\mathbf{x}(n) \ . \end{aligned} \tag{5.23}$$

In practice, neither $\mathbf{R_x}$ nor $\mathbf{r_{xy}}$ is known and must be estimated from the sample data returns. The adaptive weights are found using the SMI technique [54] which is combined with diagonal loading [12]

$$\hat{\mathbf{w}}_{\mathbf{bs}} = \left(\hat{\mathbf{R}}_{\mathbf{x}} + \sigma_l^2\mathbf{I}\right)^{-1} \hat{\mathbf{r}}_{\mathbf{xy}} \ . \tag{5.24}$$

$\hat{\mathbf{R}}_{\mathbf{x}}$ and $\hat{\mathbf{r}}_{\mathbf{xy}}$ are the sample covariance matrix and cross-covariance vector, σ_l^2 is the diagonal loading power, and $\mathbf{I}$ is an identity matrix with the same dimensions as $\hat{\mathbf{R}}_{\mathbf{x}}$. Diagonal loading is necessary to ensure that the adaptive weights have a desirable frequency response when only a limited number of samples is available for training. Recall that it also helps to prevent amplification and distortion of the monostatic clutter through TSI mitigation.

The beamspace TSI canceler can be recast as an adaptive predictor that uses the $(M-1)$ auxiliary beam signals ($x_m(n)$ for $m = 2, 3, \ldots, M$) to estimate the

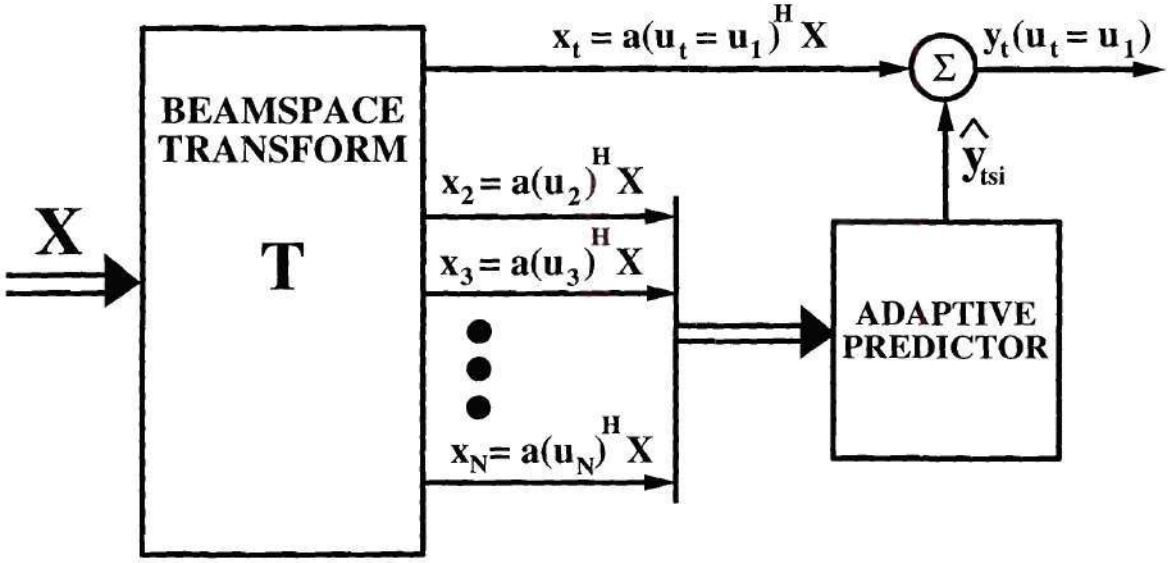

Figure 5.9: Beamspace TSI canceler with beamspace transform. Adaptive weights applied to signals from beams orthogonal to target mainbeam.

interference in another beam, $x_1(n)$. This interpretation of the beamspace canceler is shown in Fig. 5.9. The adaptive weights of the canceler can be rewritten as

$$\mathbf{w_1} = \mathbf{R_1^{-1}}\,\mathbf{r_1} \tag{5.25}$$

where $\mathbf{R_1} = \mathbf{R_x}$ and $\mathbf{r_1} = \mathbf{r_{xy}}$. The subscript 1 is used to denote that the adaptive weights, sample covariance matrix, and sample cross-covariance vector correspond to the TSI canceler for the first beam. The output for the first beam is given by (5.23).

Note that each of the beamspace signals corresponds to a different direction-of-look, has a non-adaptive spatial filter associated with it, and potentially contains TSI energy. The beamspace transform uniformly tiles the spatial frequency spectrum into the individual beams. Therefore, in the same manner that the beamspace signals $x_m(n)$ for $m = 2, 3, \ldots, M$ were used to filter the TSI present in $y(n) = x_1(n)$, the TSI present in each of the $(M-1)$ auxiliary beamspace signals can have its TSI filtered using the other beamspace signals and the target beam. Thus, TSI

cancellation for an entire PRI is performed on the assumed target direction beam and on the $(M-1)$ auxiliary beams at the spatial frequencies given by (5.13) [39]. The implementation of the full beamspace TSI canceler is shown in Fig. 5.10. Each TSI filter represents a beamspace canceler from Fig. 5.8 in which TSI is removed from the beamspace signal with spatial frequency u_m. In this manner, the spatial dimension is preserved through TSI processing because the output $\mathbf{x_{out}}(n)$ has the same dimension as $\mathbf{x_{in}}(n)$. For example, a TSI filter is applied to $x_2(n)$ using $\{x_1(n), x_3(n), \ldots x_M(n)\}$ in the same manner as the TSI was removed from $x_1(n)$ using the beamspace signals $\{x_2(n), x_3(n), \ldots x_M(n)\}$. Therefore, in the TSI canceler for the mth beam, the upper branch signal is the mth beamspace signal from (5.19) and is given by

$$y(n) = x_m(n) \tag{5.26}$$

where now there is presumably no actual target present. Instead, $x_m(n)$ is the beamspace signal for which TSI is removed. Note that although no targets are present, monostatic clutter is potentially contained in the beam. In order to pass the it through the TSI mitigation stage, the clutter signal should be treated as a target by imposing the distortionless response constraint of the beamspace canceler. The signal prediction vector in the lower branch is formed with the remaining beamspace signals from (5.19), excluding $x_m(n)$, at the various delays

$$\mathbf{x}(n) = \begin{bmatrix} \mathbf{x_1}(n) \\ \vdots \\ \mathbf{x_{m-1}}(n) \\ \mathbf{x_{m+1}}(n) \\ \vdots \\ \mathbf{x_M}(n) \end{bmatrix} \tag{5.27}$$

where the individual vectors $\mathbf{x_j}(n)$ for $j = 1, \ldots, m-1, m+1, \ldots, M$ are given by (5.21). The adaptive weights for beamspace TSI cancellation of the mth beamspace signal are

$$\mathbf{w_m} = \mathbf{R_m^{-1}}\,\mathbf{r_m}\ , \tag{5.28}$$

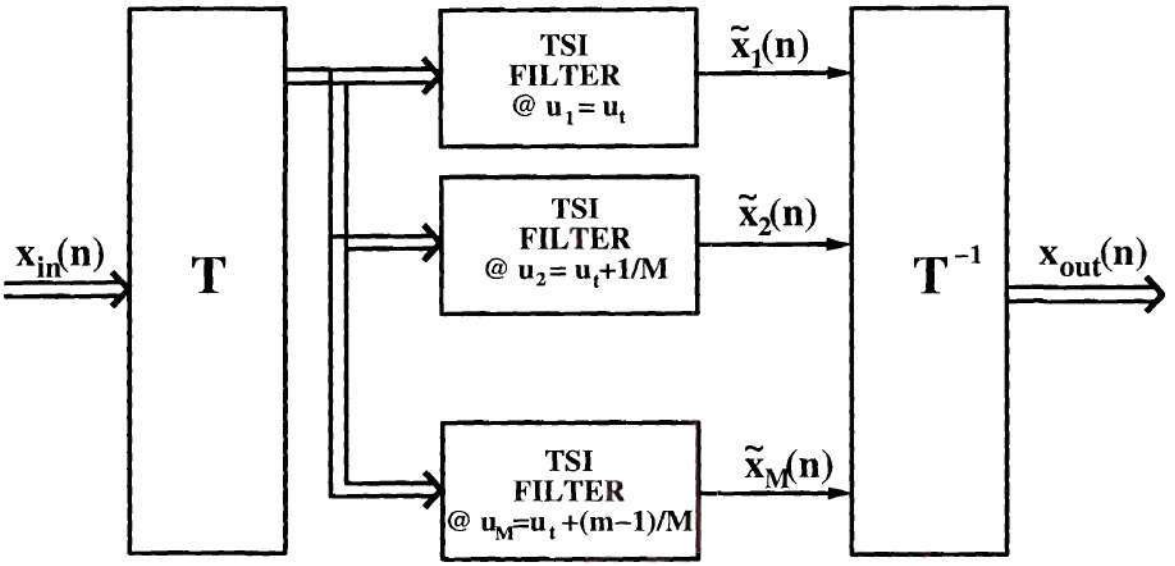

Figure 5.10: Full beamspace TSI processing for one PRI. Mitigation performed on all M beamspace signals. The TSI canceler outputs are transformed back into element space.

---

where now $\mathbf{R_m}$ and $\mathbf{r_m}$ are the covariance matrix and cross-covariance vector corresponding to the signal prediction vector $\mathbf{x}(n)$ from (5.27) and upper branch signal in (5.26). The output of the beamspace TSI canceler for the mth beamspace signal is

$$\begin{aligned} \tilde{x}_m(n) &= y(n) - \hat{y}_{tsi}(n) \\ &= x_m(n) - \mathbf{w_m}^H \mathbf{x}(n) \end{aligned} \tag{5.29}$$

where $\mathbf{x}(n)$ is the signal prediction vector specific to the mth beam from (5.27). All of the M beamspace TSI cancelers that make up the full beamspace canceler are implemented using the SMI method [54].

In this manner, each individual beamspace signal $x_m(n)$ has its TSI removed using spatial and range information in the other $(M-1)$ beams. If TSI mitigation has been performed in all of the M beams, the output signals can be concatenated

to form the TSI-filtered beamspace signal

$$\tilde{\mathbf{x}}_{\mathbf{bs}}(n) = \begin{bmatrix} \tilde{x}_1(n) \\ \tilde{x}_2(n) \\ \vdots \\ \tilde{x}_M(n) \end{bmatrix} . \tag{5.30}$$

Note that the distortionless look-direction constraints in the M TSI cancelers make up an inherent transform from element to beamspace. The $M \times 1$ beamspace TSI-filtered signal can be converted back to element-space by applying an inverse beamspace transform. The output of the PRI beamspace TSI mitigation stage is

$$\begin{aligned} \tilde{\mathbf{x}}_{\mathbf{out}}(n) &= \left(\mathbf{T}^{-1}\right)^H \tilde{\mathbf{x}}_{\mathbf{bs}}(n) \\ &= \mathbf{T}\tilde{\mathbf{x}}_{\mathbf{bs}}(n) \end{aligned} . \tag{5.31}$$

The resulting PRI output signal can now use STAP for monostatic clutter nulling. If the signals from each PRI are processed in the same manner, a CPI data-cube is available for STAP as is shown in Fig. 5.11. The CPI data-cube on the left of the figure contains TSI, while the CPI on the right has had its TSI removed or at least diminished. In this sense, the input CPI can be viewed as being contaminated with TSI, while the output CPI has been "cleansed" of interference. Note that each TSI mitigation filter block represents the full beamspace canceler from Fig. 5.10 whose adaptive weights must be computed independently for each PRI.

Now we wish to address the computational aspects of the full beamspace TSI mitigation scheme just outlined. The TSI mitigation must be performed independently in each beam, i.e., a different set of adaptive weights must be computed for each beam. The task of independently computing the adaptive weights associated with all of the TSI cancelers becomes quite formidable, particularly since the covariance matrices differ for the cancelers of all the different beams. Some savings in computation can be realized by exploiting the redundancies in the sample covariance statistics by adding and deleting rows and columns of the covariance matrices of the individual cancelers. However, it is also possible to perform all of the processing in a

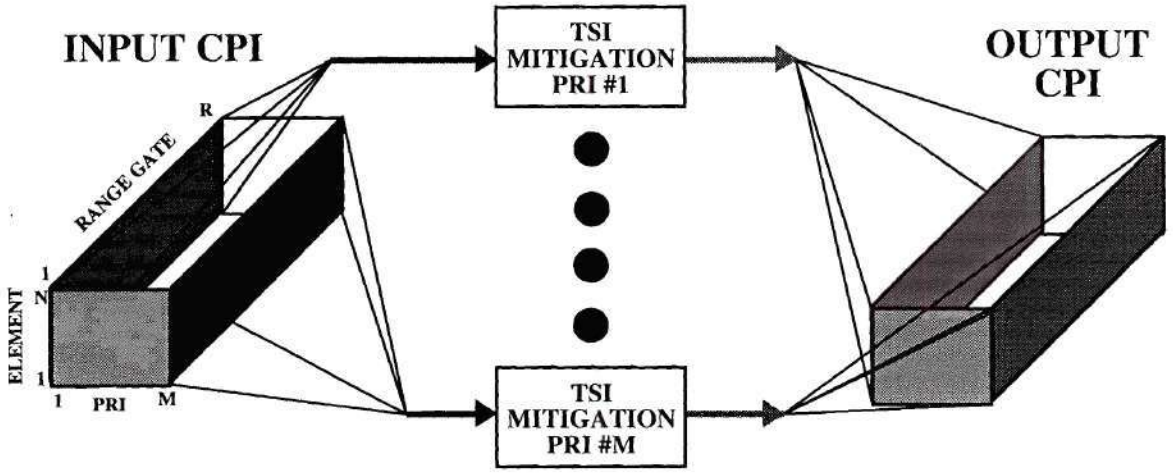

Figure 5.11: Beamspace TSI processing for an entire CPI. The details for each TSI mitigation block are found in Fig. 5.10

block fashion on the entire PRI. Recall that the GSC has an alternate implementation as a linearly constrained minimum variance (LCMV) processor [20]. In Chapter 3, the constrained element space processor (CESP) was shown to be alternate representation of the beamspace TSI canceler. The CESP uses an element space covariance matrix that remains unchanged for any assumed target direction ϕ_t. Therefore, the adaptive weights for TSI mitigation can be found as

$$\mathbf{w_e} = \mathbf{R_e^{-1}C}\left(\mathbf{C}^H\mathbf{R_e^{-1}C}\right)^{-1}\mathbf{d} \tag{5.32}$$

where $\mathbf{R_e}$ is the element space covariance matrix, $\mathbf{C}$ is the constraint matrix, and $\mathbf{d}$ is the constraint response vector. See Section 3.5 for details. The advantage with this formulation is that when the processor is implemented using SMI, the sample covariance matrix need only be computed once. Only the constraint matrix $\mathbf{C}$ changes for each different assumed target direction. Note that the term $\left(\mathbf{C}^H\mathbf{R_e^{-1}C}\right)^{-1}$ must be inverted for each TSI filter since the constraint matrix $\mathbf{C}$ does not remain the same.

5.4.2 Minimum Variance STAP

The output CPI from the TSI mitigation stage is now ready for monostatic clutter cancellation. By utilizing adaptivity in both space and PRI, clutter nulling algorithms are able to achieve significant suppression, reducing clutter interference below the thermal noise floor [67]. The technique, known as space-time adaptive processing (STAP), dates back to the early work of Brennan and Reed [8, 6] and is the topic of a recent technical report by Ward [67]. Our goal is not to perform a thorough investigation of STAP techniques, but rather to choose an effective algorithm to perform the clutter nulling function within the factored full beamspace/STAP architecture. For further details on STAP see Chapter 2.

From (5.31), the output of the TSI mitigation stage for each PRI is $\tilde{\mathbf{x}}_{\mathbf{out}}(n)$. If we define the TSI mitigation output signal from the lth PRI as $\tilde{\mathbf{x}}^{\mathbf{l}}_{\mathbf{out}}(n)$, then the output CPI space-time signal vector is obtained by stacking the $M \times 1$ PRI signals

$$\tilde{\mathbf{z}}(n) = \begin{bmatrix} \tilde{\mathbf{x}}^{(\mathbf{1})}_{\mathbf{out}}(n) \\ \vdots \\ \tilde{\mathbf{x}}^{(\mathbf{l})}_{\mathbf{out}}(n) \\ \vdots \\ \tilde{\mathbf{x}}^{(\mathbf{L})}_{\mathbf{out}}(n) \end{bmatrix}, \tag{5.33}$$

where L is the number of PRIs in a CPI. The full CPI signal $\tilde{\mathbf{z}}(n)$ is then sent on to the clutter mitigation processor.

The STAP method chosen is minimum variance STAP processing, sometimes referred to as fully adaptive STAP [67]. Note that several, more efficient, partially adaptive methods are available [67] but are not considered here. Minimum variance STAP applies an adaptive space-time weight vector directly to the full rank space-time snapshot vectors $\mathbf{z}(n)$. The output signal is used as a detection statistic to determine if a target signal is present. The space-time adaptive weights are found using the minimum variance criterion with a single linear constraint corresponding to an assumption on the target. The algorithm is implemented using SMI [54] and the

SMI adaptive weights are

$$\hat{\mathbf{w}}_{\mathbf{stap}} = \hat{\mathbf{R}}_{\mathbf{z}}^{-1}\mathbf{s_t} \tag{5.34}$$

where $\mathbf{s_t}$ is the target constraint. The space-time sample covariance matrix is

$$\hat{\mathbf{R}}_{\mathbf{z}} = \frac{1}{N_t}\sum_{k=1}^{N_t}\mathbf{z}(n_t(k))\mathbf{z}^H(n_t(k)) \ . \tag{5.35}$$

$n_t(k)$ for $k = 1, 2, \ldots, N_t$ are the N_t are indices of the space-time snapshots that determine the training interval within a CPI for weight computation. Typically, a region around the range cell of interest is selected over which the clutter statistics are approximately stationary. In addition, a guard band about the range cell of interest is used, whose space-time snapshots are removed from the computation of the sample covariance matrix $\hat{\mathbf{R}}_{\mathbf{z}}$. Potential target leakage into neighboring range gates can cause target signal cancellation.

The space-time constraint vector $\mathbf{s_t}$ is determined by the assumed target azimuth and Doppler frequencies. The constraint is given by

$$\mathbf{s_t} = \mathbf{b_t} \otimes \mathbf{a_t} \tag{5.36}$$

where again $\otimes$ denotes a Kronecker product. The vectors $\mathbf{b_t}$ and $\mathbf{a_t}$ are target Doppler and spatial steering vectors given by (2.18). A block diagram of the minimum variance or fully adaptive STAP processor is shown in Fig. 5.12. For further details on STAP see Chapter 2.

5.5 Factored Beamspace/Adaptive MTI Processing

In order to evaluate the performance of the factored full beamspace/STAP algorithm for combined TSI and monostatic clutter interference, we describe a factored beamspace and adaptive moving target indicator (MTI) processing algorithm [7, 41, 51, 57]. This method does not retain the spatial degrees of freedom through TSI

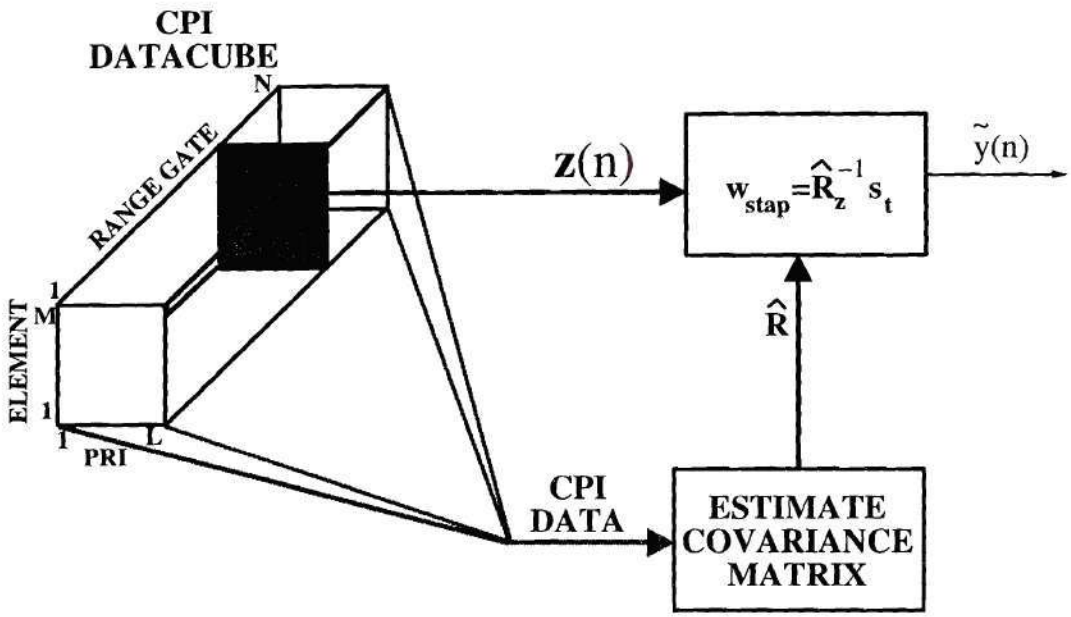

Figure 5.12: Minimum variance space-time adaptive processor.

cancellation and as a result lacks the ability to utilize spatial adaptivity for clutter nulling. Instead, the clutter and target signals are distinguished by their respective velocities with respect to the radar receiver platform through MTI processing, also commonly referred to Doppler processing.

Using the beamspace TSI mitigation routine described in Chapter 3 and shown in Fig. 5.8, each PRI is processed in the target direction-of-look ϕ_t. A non-adaptive beam is formed at the target azimuth angle ϕ_t and beamspace TSI mitigation is performed by estimating the mainbeam interference using TSI energy found in the beams orthogonal to the target beam. The output of the lth PRI, $\tilde{x}_l(n)$, is the target beam signal with the TSI removed. The same operation is performed for all L PRIs with the resulting target beam signals passed on to the clutter nulling stage from

Fig. 5.4. The signal vector of beamspace TSI canceled (target beam only) signals is

$$\mathbf{x_d}(n) = \begin{bmatrix} \tilde{x}_1^{(1)}(n) \\ \vdots \\ \tilde{x}_1^{(l)}(n) \\ \vdots \\ \tilde{x}_1^{(L)}(n) \end{bmatrix} . \tag{5.37}$$

Clutter nulling is performed using adaptive MTI processing. The L PRI signals are adaptively combined. The adaptive weights are found with the minimum variance criterion subject to the assumed target Doppler frequency constraint. The output power of the processor is minimized subject to the Doppler frequency constraint

$$\mathbf{b_t} = \mathbf{b}(\bar{f}_t) = \frac{1}{\sqrt{L}} \left[e^{-j2\pi \frac{L-1}{2} \bar{f}_t} \cdots e^{-j2\pi (\frac{L-1}{2} - l) \bar{f}_t} \cdots e^{j2\pi \frac{L-1}{2} \bar{f}_t} \right]^T \tag{5.38}$$

where $\bar{f}_t$ is the normalized Doppler frequency of the target determined by the target velocity relative to the radar receiver and given by (2.9). Again, the SMI technique is used to compute the adaptive weights. The SMI adaptive weights of the MTI filter are

$$\hat{\mathbf{w}}_\mathbf{d} = \hat{\mathbf{R}}_\mathbf{d}^{-1} \mathbf{b_t} \tag{5.39}$$

where the Doppler sample covariance matrix is

$$\hat{\mathbf{R}}_\mathbf{d} = \frac{1}{N_t} \sum_{k=1}^{N_t} \mathbf{x_d}(n_t(k)) \mathbf{x_d}^H(n_t(k)) . \tag{5.40}$$

The training interval is defined by the indices $n_t(k)$ for $k = 1, 2, \ldots, K$. Note that non-adaptive MTI processing is performed by setting the weight vector $\mathbf{w_d} = \mathbf{b_t}$. A block diagram of the processing is shown in Fig. 5.13.

The adaptive MTI processor passes all signals at the target Doppler frequency $\bar{f}_t$ without distortion (zero phase). Other portions of the Doppler spectrum with significant energy content are assigned frequency nulls in order to minimize the output power (variance). The shortcoming of the adaptive MTI filter is that it is unable to

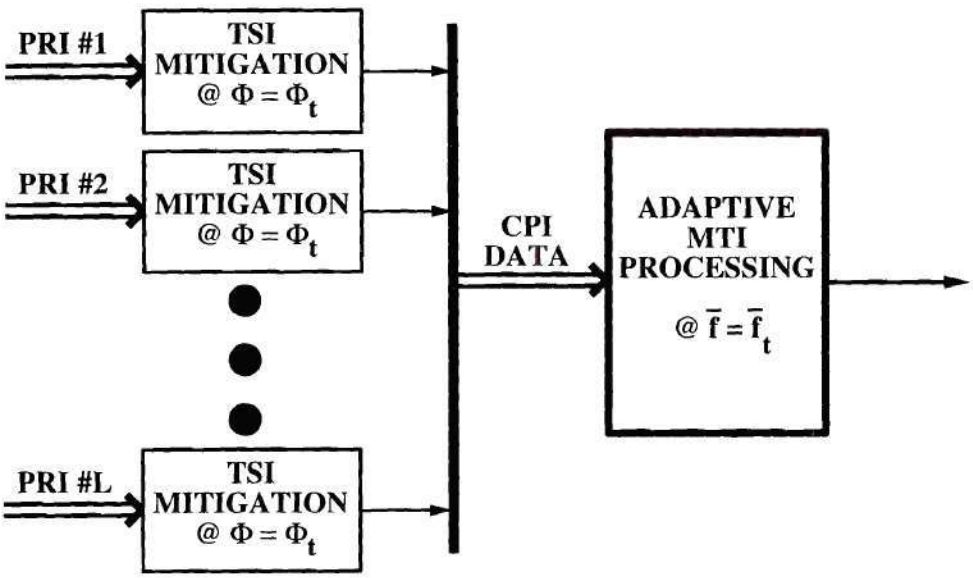

Figure 5.13: TSI mitigation and adaptive MTI processing.

filter out interference energy at the same Doppler as the target. As can be seen from the azimuth-Doppler spectrum in Fig. 5.7, sidelobe clutter is potentially at the same Doppler frequency as the target. By not preserving the spatial adaptivity for clutter nulling purposes, the factored beamspace/adaptive MTI processor lacks the ability to extract targets in such interference environments.

5.6 Experimental Results

In this section, the factored full beamspace/STAP method from Section 5.4 is demonstrated on radar returns collected as part of the DARPA/Navy Mountaintop experiment [40, 61]. The goal here is to determine the effect of full beamspace TSI mitigation (in M beams) on the clutter returns and to demonstrate the ability of the method to extract targets in combined TSI and monostatic clutter environments. In addition, the performance of the method is compared to TSI mitigation in the target

beam only with clutter nulling via adaptive and non-adaptive MTI processing from Section 5.5.

The Mountaintop data sets used all contained experimental TSI collected at the White Sands Missile Range with the RSTER-90 radar system [13]. The radar receiver ULA has adaptivity in azimuth with $M = 14$ horizontally-aligned elements spaced at $\lambda = 0.33$ meters. The operating frequency in all experiments was 435 MHz and the sampling rate of the A/D converter was 1 MHz. The radar was operated in pulsed mode with $L = 16$ PRIs per CPI transmitted at a pulse repetition frequency (PRF) of 312.5 Hz [40, 61]. Two sets of data were used: one containing experimental TSI and simulated clutter returns and the second containing both experimental TSI and clutter.

5.6.1 Simulated Monostatic Clutter

In the first group of trials, simulated monostatic clutter returns were added to the experimentally collected TSI in order to demonstrate the ability of the full beamspace/STAP method in a controlled environment. In addition, the simulated returns allow for the examination of the effect of TSI mitigation on the entire clutter ridge across the azimuth-Doppler spectrum.

The experimental TSI was produced by a ground-based (stationary) jammer at 303° (`mmit004v1.mat` file) with a direct-path JNR of approximately 75 dB. The clutter returns were simulated using a "sandpaper" model [67] with scatterers in the first 1000 range cells (150 kilometers) at all azimuth angles. The magnitudes of the clutter returns are random (complex Gaussian distribution) with an average power level or clutter-to-noise ratio (CNR) of 40 dB. The airborne radar velocity is chosen so that the slope of the clutter ridge is $\beta = 1$. In addition, a target signal is injected at a range of 75 kilometer (range cell 500) with an input SNR of 20 dB at an azimuth of $\phi_t = 275°$ and normalized Doppler frequency of $\bar{f}_t = -0.25$. The azimuth-Doppler spectrum of the input CPI returns is shown in Fig. 5.14. The direct-path jammer

signal and the sidelobes associated with it dominate the returns. The TSI, monostatic clutter, and target signal are hidden at lower power levels.

The factored full beamspace/STAP method was applied to the returns with the number of taps used by the TSI canceler set to $N_{bs} = 20$. The TSI weight training interval was at far-field ranges (range cells $1001 - 1824$) and the diagonal loading level of the sample covariance matrix was equal to the thermal noise power. First we examine the output of the full beamspace TSI canceler in order to determine how well the clutter returns were preserved through the TSI mitigation stage. The azimuth-Doppler spectrum of the TSI mitigation output CPI is shown in Fig. 5.15. The jammer direct-path signal has been removed along with a large portion of the TSI so that the clutter ridge is now clearly visible. The spreading of the clutter ridge is minimal. In addition, residual TSI energy is still present in the vicinity of the jammer location at spatial frequencies slightly less than and greater than the jammer ($\phi = 303°$ or $\sin\phi \approx 0.5$). The azimuth-Doppler frequency response of the STAP filter is shown in Fig. 5.16 which has the desired behavior: unity gain (0 dB) on the target ($\phi_t = 275°$, $\bar{f}_t = -0.25$) and nulls along the clutter ridge and in the regions of residual TSI.

The performance of the factored full beamspace/STAP processor is compared to the factored beamspace/MTI method described in Section 5.5. Both adaptive and non-adaptive MTI were used. The outputs of the three different processors are shown in Fig. 5.17. Clearly, the full beamspace/STAP method is the only one that was able to extract the target (range 75 kilometers) with a residual INR of approximately 14 dB. On the other hand, the two MTI methods, adaptive and non-adaptive, had residual INRs of 20.4 and 21.5, respectively, which is not sufficient to detect the target signal. Note that in all cases the target signal experiences a 12 dB gain due to coherent integration over the 16 pulses. Therefore, the target output signal is expected to be approximately 32 dB. In all cases, the target signal experienced some gain since it was greater than its original 20 dB level but was not at the expected

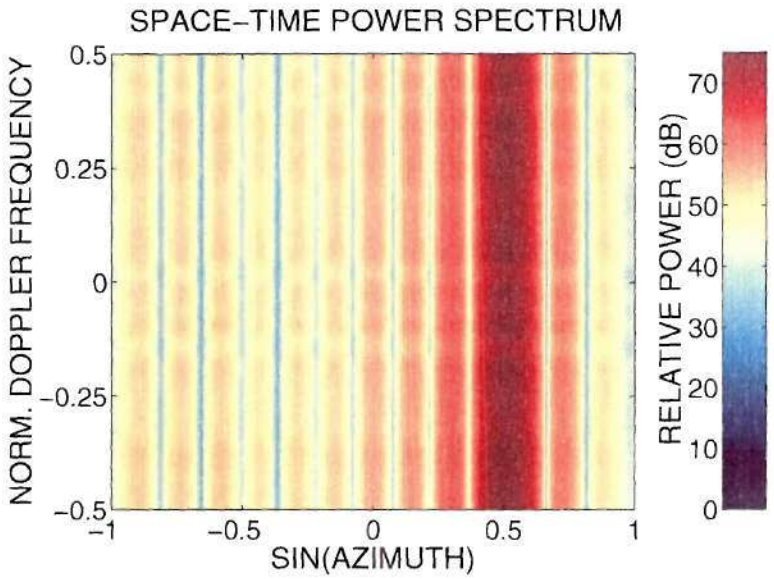

Figure 5.14: Simulated clutter/experimental TSI azimuth-Doppler spectrum before TSI mitigation.

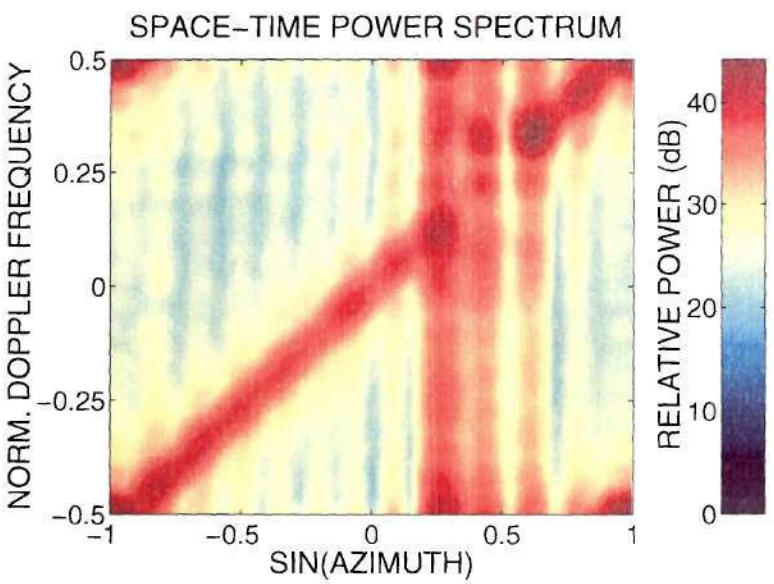

Figure 5.15: Simulated clutter/experimental TSI azimuth-Doppler spectrum after TSI mitigation.

power of 32 dB. Therefore, some target loss was experienced during processing. The source of the signal loss might be attributed to the fact that during TSI mitigation of non-target beams, the target signal may find itself passed through the lower branch of the canceler, creating possible target leakage into other azimuth angles.

5.6.2 Experimental Monostatic Clutter

The factored full beamspace/STAP method was next applied to radar returns containing both experimental clutter and TSI. In this case, simulated platform motion was generated using the inverse displaced phased center array (IDPCA) method [2]. The aircraft velocity was set to the maximum detectable velocity ($\beta = 1$). In this case, TSI was produced by an airborne jammer at $\phi = 268°$ with a direct-path signal greater than 70 dB. The injected target had the same parameters as in the previous experiment: input SNR = 20 dB, azimuth $\phi_t = 275°$, and normalized Doppler frequency $\bar{f}_t = -0.25$. The azimuth-Doppler spectrum of the input CPI is shown in Fig. 5.18 which again is dominated by the jammer direct-path signal.

The factored full beamspace/STAP method is applied to the returns with 20 taps per beam for TSI mitigation. Weight training is again performed at far-field ranges. First, examining the output of the full beamspace TSI canceler in terms of the azimuth-Doppler spectrum shown in Fig. 5.19, we observe that the structure of the clutter is again well preserved, lying mostly along the expected clutter ridge. Note that in the case of experimental clutter the returns are primarily from the sector of the azimuth plane between $\phi = -30°$ and $\phi = 30°$. Since the antenna directionally transmits in the direction-of-look ($\phi = 0°$), the monostatic returns are confined to the portion of the angular spectrum near the assumed target direction. Next, the azimuth-Doppler frequency response of the STAP filter is shown in Fig. 5.20, again with the desired results: unity gain on target ($\phi_t = 275°$, $\bar{f}_t = -0.25$) with a null in the regions of the strong clutter returns and residual TSI.

The performance of the factored full beamspace/STAP method was again com-

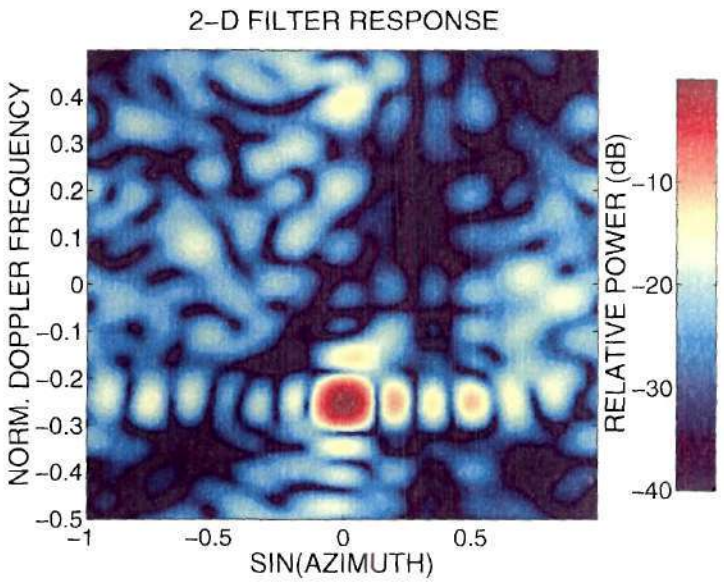

Figure 5.16: Simulated clutter/experimental TSI azimuth-Doppler frequency response of STAP filter for factored full beamspace/STAP mitigation.

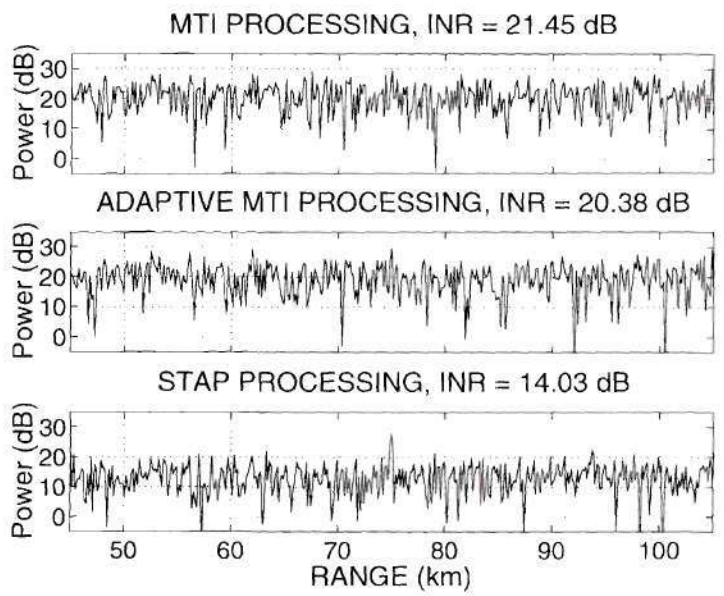

Figure 5.17: Simulated clutter/experimental TSI output signals. The factored processing methods considered use conventional and adaptive MTI processing and STAP for monostatic clutter mitigation.

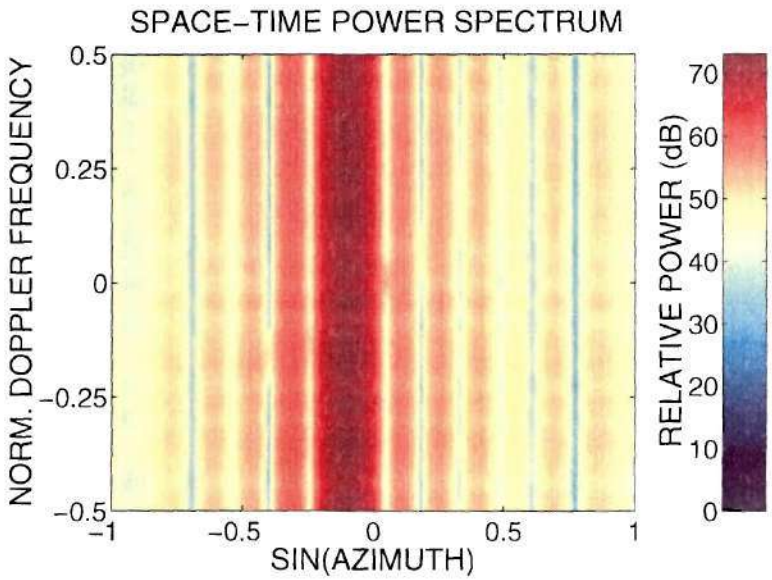

Figure 5.18: Experimental clutter/TSI azimuth-Doppler spectrum before TSI mitigation.

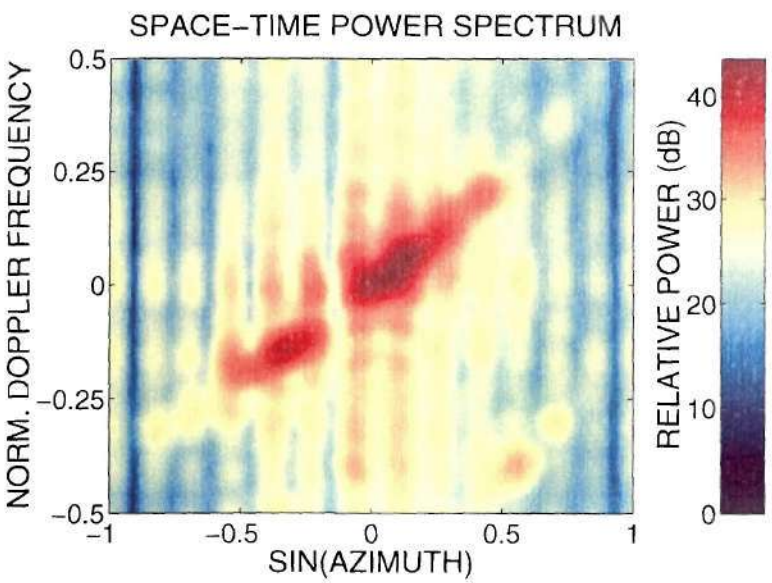

Figure 5.19: Experimental clutter/TSI azimuth-Doppler spectrum after TSI mitigation.

pared to the two factored beamspace/MTI methods. The output signals of the respective cancelers are shown in Fig. 5.21. The full STAP method reduced the interference to 10.8 dB while the adaptive and non-adaptive MTI methods had residual INRs of 28.4 dB and 29.4 dB, respectively. Therefore, the target at range 75 kilometers can only be extracted using the full beamspace/STAP approach. Target attenuation is much less significant than in the prior case for simulated clutter with an output SNR level of about 30 dB (32 dB expected). Also, note that the performance of the proposed algorithm is actually better with experimental clutter than with simulated clutter. However, by examining Fig. 5.15, it is evident the simulated clutter produced a more stressing environment in terms of degrees of freedom by filling the entire clutter ridge with interference energy. On the other hand, the experimental clutter, as seen in Fig. 5.19, is confined to only a portion of the expected clutter ridge.

5.7 Conclusions

In this chapter, a mitigation technique has been presented for the extraction of target signals in environments containing *both* TSI and monostatic clutter interference. Prior to the derivation of the method, the justification for a factored approach was explained. Namely, the sample support required for a 3-D adaptive processor is typically not available, in addition to the computational burden such a processor imposes. Training interval considerations and sample covariance matrix conditioning were also discussed.

The processing technique consists of performing TSI mitigation in M orthogonal beams for each PRI in order to preserve the spatial degrees of freedom for the subsequent clutter nulling. In addition to removing TSI from the target beam, TSI is also removed from auxiliary beams which potentially contain clutter returns necessary for nulling purposes. Without TSI removal in these beams, the clutter nulling algorithm would suffer performance loss due to its reduced ability to estimate and

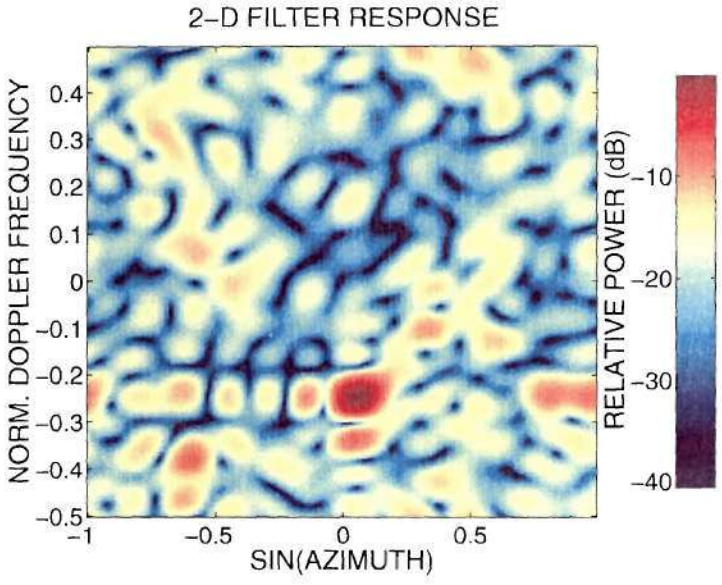

Figure 5.20: Experimental clutter/TSI azimuth-Doppler frequency response of STAP filter for factored full beamspace/STAP mitigation.

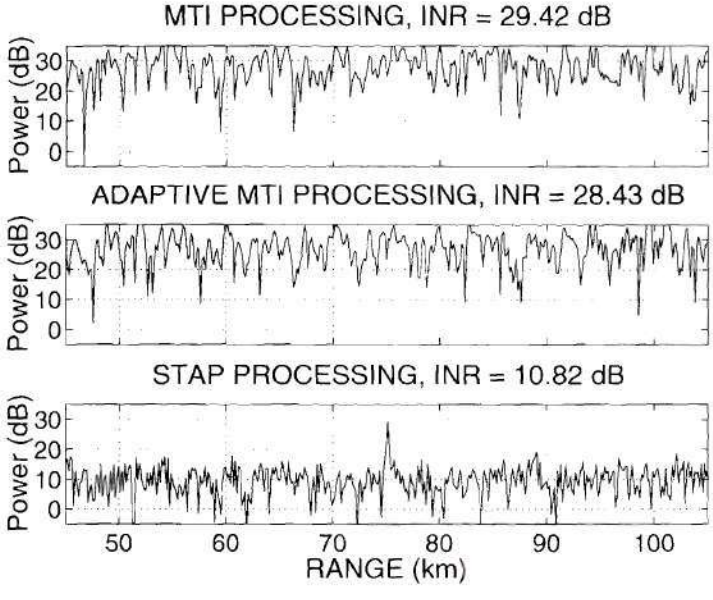

Figure 5.21: Experimental clutter/TSI output signals. The factored processing methods considered use conventional and adaptive MTI processing and STAP for monostatic clutter mitigation.

subsequently null the clutter coherent with the target. Following a transform back into element-space, the TSI mitigation processor passes a CPI, "cleansed" of TSI, to the monostatic clutter nulling stage. The preservation of the spatial degrees of freedom through TSI mitigation allows for the full spatial adaptivity required for STAP.

The factored full beamspace/STAP method was applied to experimental returns collected as part of the Mountaintop experiment. The proposed technique demonstrated the ability to extract targets in interference environments containing both TSI and monostatic clutter. The factored full beamspace/STAP method was also compared to two MTI methods, adaptive and non-adaptive Both of these methods performed TSI mitigation on only the target beam prior to MTI processing. The factored full beamspace/STAP method clearly outperforms both of the MTI methods. While the proposed method can extract targets from these severe environments, the performance degradation associated with the loss of spatial adaptivity for clutter cancellation resulted in the two MTI methods being unable to extract targets.

CHAPTER 6

Beamspace Mainbeam Jammer Cancellation

Adaptive array processing techniques have been shown to be an effective means of mitigating jamming interference in the sidelobes of an array [15, 30, 32, 48]. However, as the separation angle between the target and jammer decreases, the jamming source enters the mainbeam of the array and the problem becomes much more difficult. A variety of adaptive processing methods have been suggested for the mainbeam jamming problem. One approach, originally proposed by Adams, Horowitz, and Senne, uses a series of overlapping beams clustered around the direction-of-look [1, 23]. The signals from the various beams are adaptively weighted in order to enhance the desired signal while steering a null at the jammer, where the adaptive weights are found via frequency diversity techniques. Other proposed methods include an interferometric technique using an auxiliary sidelobe array [24, 18] and another method of steering nulls at the mainbeam jamming sources [60]. These techniques provide a degree of cancellation which helps to partially restore detection capability in the assumed target direction [3]. However, the mainbeam jamming problem studied in this chapter differs from the problem addressed by the aforementioned methods because the jammer is considered to be so close to the target that the two are essentially co-located. This problem has not been studied in great detail in the unclassified literature. The goal here is to extend the beamspace TSI mitigation methods developed in Chapter 3 to the problem in which the target and jammer are spatially coherent, i.e., co-located.

The hope is to exploit temporal correlation, rather than spatial, and to study the cancellation capabilities of the beamspace canceler for this mainbeam interference. For the purposes of this chapter, the problem is treated in one spatial dimension, azimuth, and the radar receiver is assumed to consist of a uniform linear array (ULA) of sensor channels, all digitized to allow for adaptivity in azimuth. The generalization to 2-D arrays with adaptivity in azimuth and elevation is fairly straightforward, as the same principles discussed here apply there as well.

6.1 Problem Statement

The presence of jammers within the mainbeam of the radar receiver array presents a particularly challenging adaptive processing problem. Technically, a mainbeam jammer is defined as a jammer that is spatially located within the 3 dB beamwidth of the assumed target direction. Although the jammer is in the mainlobe of the radar receiver, it is sometimes possible to cancel the jammer through spatial nulling techniques [1, 3, 23, 24, 42, 60]. Consider the quiescent beam pattern (spatial frequency response) of a 14 element ULA with an assumed target direction of $\phi_t = 0°$, shown as the solid line in Fig. 6.1. In the case of a jammer in the mainbeam, whose location is indicated with an arrow, a null can be steered in the direction of the jammer using a minimum variance distortionless response (MVDR) spatial filter [11]. The MVDR weight vector is given by

$$\mathbf{w} = \mathbf{R}^{-1}\mathbf{a_t} \ , \tag{6.1}$$

where, again, $\mathbf{R}$ is the element space covariance matrix and $\mathbf{a_t} = \mathbf{a}(u_t)$ is the phase-centered steering vector in the assumed target direction, ϕ_t. The resulting adapted beam pattern is shown as the dashed line in Fig. 6.1 where the jammer is successfully *mitigated* while maintaining unity gain on the target. However, as the separation angle between the jammer and target decreases, the adapted pattern begins to degrade severely as shown in Fig. 6.2, again as the dashed line. The sidelobes are raised

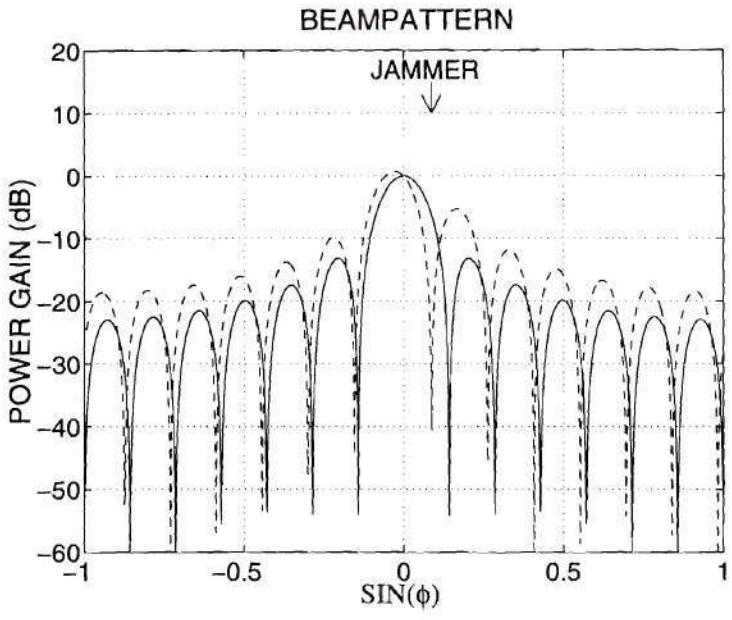

Figure 6.1: Quiescent beampattern (solid line) and MVDR adapted beampattern (dashed line) for assumed target direction of $\phi_t = 0°$ and a jammer at $\phi_j = 5°$ (JNR = 50 dB).

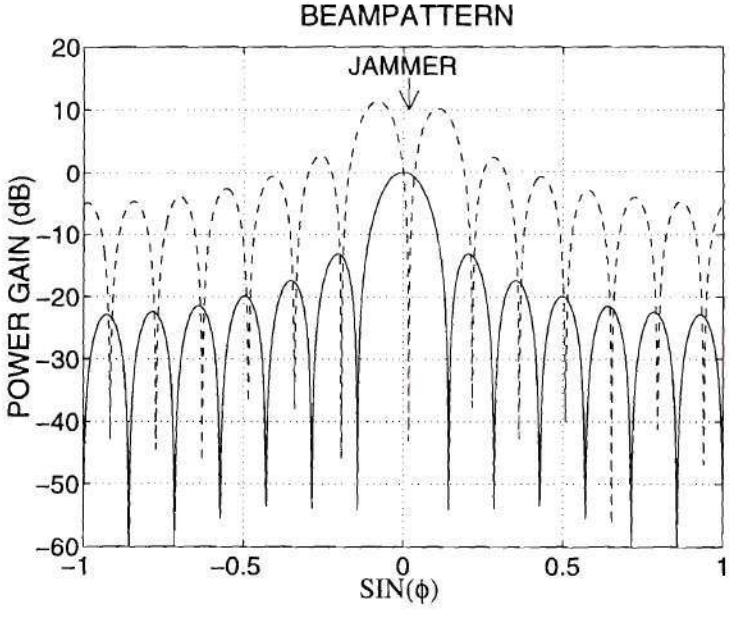

Figure 6.2: Quiescent beampattern (solid line) and MVDR adapted beampattern (dashed line) for assumed target direction of $\phi_t = 0°$ and a jammer at $\phi_j = 1°$ (JNR = 50 dB).

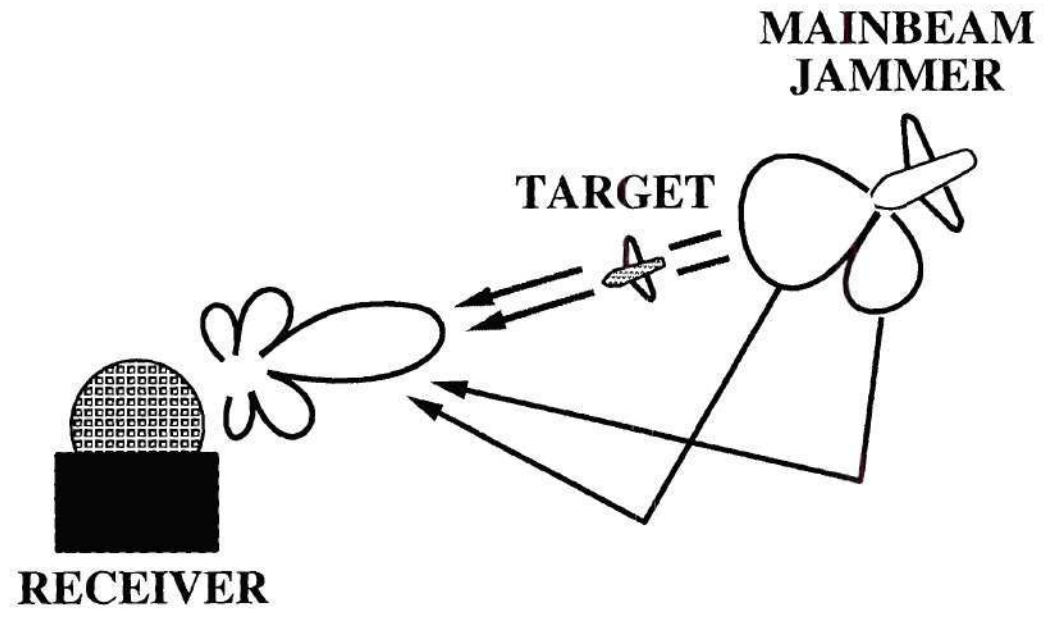

Figure 6.3: Mainbeam jammer scenario indicating potential jammer multipath reflections present at the radar receiver.

to unacceptable levels, actually amplifying signals found outside of the mainbeam. The result is a dramatic increase in vulnerability to sidelobe jammers and an actual amplification of the thermal noise. This increase in the thermal noise floor causes a decrease in SNR and is equivalent to target signal cancellation in terms of processor performance. These problems are accentuated when multiple jammers are found in the mainbeam.

In many systems the jammer/target separation angle becomes so small that the two are assumed to be co-located. This scenario is depicted in Fig. 6.3. The jamming source may actually be on-board the target or on a hostile aircraft intentionally aligned with the target. In this case, spatial nulling is futile since the target signal would also fall in the null and be cancelled along with the jammer. The jammer is usually considered to be of the barrage-noise variety, transmitting a broadband waveform significantly greater than the bandwidth of the radar receiver so that the

sampled returns are uncorrelated. In addition, the jammer energy is significantly greater in magnitude than the target returns. As a result, the radar receiver is unable to resolve the target using conventional techniques and is essentially blind in the assumed target direction. If we define the sampled target signal at the array as

$$\mathbf{x_t}\,(n) = \alpha_t\,(n)\;\mathbf{a_t} \tag{6.2}$$

where $\mathbf{a_t}$ is the array response in the target azimuth ϕ_t, namely a phase-centered steering vector defined by the array geometry [32]. The target return signal is $\alpha_t\,(n)$ where n is the discrete-time index. On the other hand, the jammer signal is defined as

$$\mathbf{x_j}\,(n) = \alpha_j\,(n)\;\mathbf{a_j} \tag{6.3}$$

where $\mathbf{a_j}$ is the array response in the jammer azimuth ϕ_j and $\alpha_j\,(n)$ is the sampled jammer signal, which for our purposes is considered to be uncorrelated, Gaussian noise. The resulting received signal is

$$\begin{aligned} \mathbf{x_{in}}(n) &= \mathbf{x_t}(n) + \mathbf{x_j}(n) + \mathbf{x_n}(n) \\ &= \alpha_t(n)\,\mathbf{a_t} + \alpha_j(n)\,\mathbf{a_j} + \mathbf{x_n}(n)\;, \end{aligned} \tag{6.4}$$

where $\mathbf{x_n}(n)$ represents the thermal noise found in the sensor elements and is assumed to be both spatially and temporally uncorrelated. In the case of a mainbeam jammer spatially co-located with the target, the jammer and target steering vectors are equal

$$\mathbf{a_j} = \mathbf{a_t}$$

and the received signal becomes

$$\mathbf{x_{in}}(n) = [\alpha_t(n) + \alpha_j(n)]\,\mathbf{a_t} + \mathbf{x_n}(n)\;. \tag{6.5}$$

Therefore, the target signal cannot be extracted using spatial techniques. Spatial nulling methods aimed at eliminating the jammer returns inevitably cancels the target signal as well, while the MVDR processor from (6.1) simply passes the target and jammer signals unchanged.

The current approach to this problem is to acquire the mainbeam signal, containing both target and jammer, and perform matched filtering [57]. The matched filter correlates the signals with the transmitted waveform which is uncorrelated with the white noise jammer signal. Thus, the target signal energy is integrated over time, boosting the target with respect to the jammer since the jammer interference is temporally incoherent. When the matched filtering is performed over extremely long intervals, the target signal eventually becomes visible as the SNR finally becomes greater than the JNR. This method is often referred to as "burn-through" since the target signal is essentially burned through the interference. The problem with this approach is that the time durations, and therefore the radar pulse widths, required to extract the target are very large. The result is a significant decrease in the maximum pulse repetition frequency (PRF) of the radar system. A decrease in the PRF subsequently reduces the minimum detectable target velocity and can create severe aliasing problems in the PRF domain which manifest themselves in the returns as ambiguous velocities. Since velocity information is essential for target tracking, velocity errors cause a significant loss in the tracking capability of the radar system. The use of mitigation techniques to cancel the mainbeam jammer signal offer significant promise if they can achieve a mild amount of suppression. Even a modest cancellation of 5 to 10 dB would provide considerable performance gains in terms of reducing the pulse interval, increasing the PRF, and restoring target tracking capabilities.

6.2 Cancellation via Temporal Correlation

As discussed in the previous section, spatial-only processing cannot defeat jamming interference when the jammer is physically co-located with the target. Therefore, the presence of the interference in the mainbeam is conceded and the radar receiver must resort to cancellation in another domain, namely the temporal domain. The goal here is to exploit temporal correlation present in the returns to reduce the main-

beam interference. The jammer signal itself is assumed to be white noise, containing no temporal correlation. However, due to size and cost limitations imposed by an airborne platform, the jammer transmitter has a broad transmit beam with high side-lobe levels [57]. As a result, the jammer signal is transmitted in many directions and is potentially reflected by the terrain. Thus, the jammer signal may be incident on the radar receiver from azimuth angles other than the direct-path signal found in the mainbeam. Each reflected signal received by the radar array is a delayed replica of the mainbeam direct-path jammer signal, so that the sum of all the bi-static jammer reflections is a signal temporally correlated with the jammer source. In fact, the reflected signal can be viewed as the output of a linear system, determined by the terrain reflections, that is excited by a white noise source due to the jammer waveform. Therefore, the problem becomes one of adaptive equalization where the source signal (the jammer direct-path) is recovered from an auxiliary signal (the bi-static returns due to the terrain reflections). In a sense, the mainbeam jammer problem is the reverse of the TSI problem: the jammer direct-path is predicted using TSI. The proposed canceler must perform space-time adaptive processing (STAP), consisting of temporal processing in range and spatial processing, to separate the original jammer signal from the reflected signals. The jammer multipath reflections are then used to form an estimate of the mainbeam jammer signal. The estimate of the jammer signal is then subtracted from the mainbeam signal to achieve partial suppression of the interference.

The sum of the reflected signals contains both temporal and spatial correlation and can be modeled in a similar manner to the TSI signal in Chapter 2. The difference is that the direction-of-look, ϕ_t, now coincides with the jammer signal. The continuous-time reflected jammer multipath signal model is

$$\mathbf{x_{jm}}(t) = \int_0^{T_{jm}} \int_{-\pi}^{\pi} h(\tau, \phi) \alpha_j(t - \tau)\, \mathbf{a}(\phi) d\phi\, d\tau \tag{6.6}$$

where $h(t, \phi)$ is the unknown space-time system function of the terrain reflections,

$\alpha_j(t)$ is the jammer source signal, and $\mathbf{a}(\phi)$ is the array response vector determined by the array geometry. Since the mainbeam direct-path jammer signal is not contained in the reflected signal, the function is constrained such that

$$h(t, \phi_t) = 0 \ .$$

On the other hand, the mainbeam jammer signal is given by (6.3); a white noise signal projected onto the receiver ULA by the steering vector $\mathbf{a_t} = \mathbf{a}(\phi_t)$. The overall radar receiver returns are found by adding the sampled version of the jammer multipath signal in (6.6) to (6.4)

$$\mathbf{x_{in}}(n) = \mathbf{x_t}(n) + \mathbf{x_j}(n) + \mathbf{x_{jm}}(n) + \mathbf{x_n}(n) \ . \tag{6.7}$$

The number of elements contained in the receiver ULA is M. Since one spatial degree of freedom is dedicated to the mainbeam, $(M-1)$ auxiliary beams can be formed to acquire the jammer multipath signals. The auxiliary beam signals are then input into an adaptive processor that estimates the jammer direct-path signal. Since the reflected jammer signals are from different directions and at various delays with respect to the direct-path signal, weighted temporal taps must be used in order to time-align and normalize these signals in a data-adaptive manner. Recall from Chapter 3 that the multiple beams allowed for a greatly reduced temporal window. In a sense, the adaptive processor can be viewed as a spatio-temporal deconvolution filter since it estimates the jammer source from the terrain reflections corresponding to the input and output of a linear system, respectively. The estimate of the jammer direct-path signal is then subtracted from the mainbeam signal. Assuming the estimate is coherent with the interference while incoherent with the target, the resulting output signal passes the target while achieving a certain amount of interference suppression. This processing approach is depicted in Fig. 6.4.

The processor described above can be split into two parts: a non-adaptive mainbeam signal and an adaptive processor that estimates the interference. The

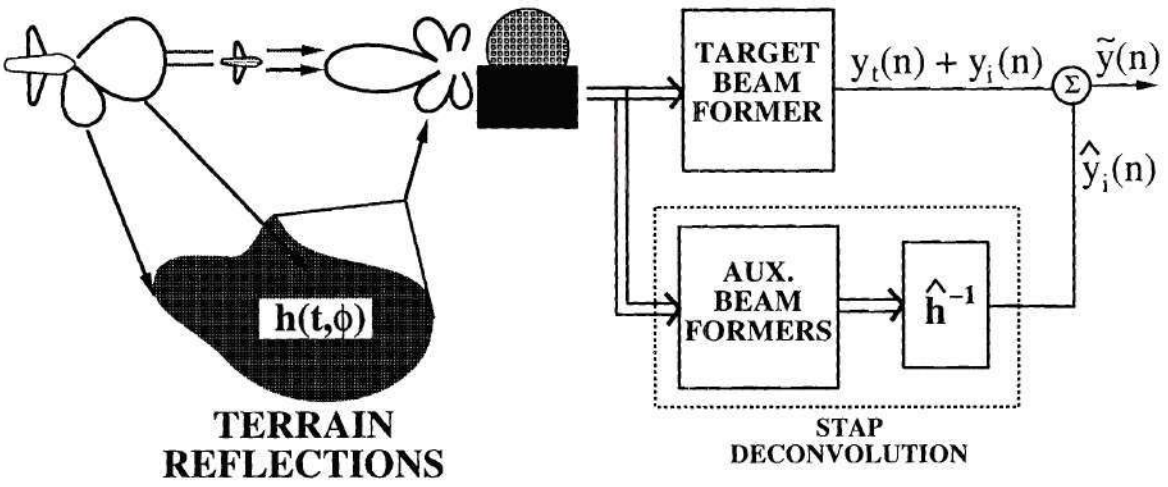

Figure 6.4: Mainbeam jammer cancellation approach.

mainbeam signal is found by applying the spatial steering vector $\mathbf{a_t} = \mathbf{a}(\phi_t)$ in the assumed target direction to the radar returns

$$y(n) = \mathbf{a_t}^H \mathbf{x_{in}}(n) \ . \tag{6.8}$$

The auxiliary beam signals are then obtained with similar spatial filters, consisting of phase-centered steering vectors in other directions ϕ. One requirement is that the target signal does not leak into the auxiliary beams. As shown for the beamspace TSI canceler in Chapter 3, this requirement is easily satisfied by using a beamspace blocking matrix $\mathbf{B_s}$ made up of steering vectors orthogonal to the target steering vector (i.e., $\mathbf{B_s}^H \mathbf{a_t} = \mathbf{0}$) where the spatial frequencies of the blocking matrix steering vectors are offset from the target spatial frequency by multiples of $\frac{1}{M}$ [36, 37]. The auxiliary beam signals are found by applying $\mathbf{B_s}$ to the radar returns

$$\mathbf{x_{aux}}(n) = \mathbf{B_s}^H \mathbf{x_{in}}(n) = \begin{bmatrix} x_2(n) \\ x_3(n) \\ \vdots \\ x_M(n) \end{bmatrix} \tag{6.9}$$

where $x_m(n)$ are the auxiliary beam signals for $m = 2, 3, \ldots, M$. Using the auxiliary beam signals, the signal prediction vector is

$$\mathbf{x}(n) = \begin{bmatrix} \mathbf{x_2}(n) \\ \mathbf{x_3}(n) \\ \vdots \\ \mathbf{x_M}(n) \end{bmatrix} \tag{6.10}$$

where $\mathbf{x_m}(n)$ are the auxiliary beam signal vectors made up of the tap delay outputs on the individual auxiliary beam signals

$$\mathbf{x_m}(n) = [x_m(n)\ x_m(n-1)\ \cdots\ x_m(n-N_{bs}+1)]^T\ . \tag{6.11}$$

An equal number of temporal taps, N_{bs}, is used for each beam. The adaptive weight vector for the canceler is then found using the Wiener-Hopf equation [28, 32]

$$\mathbf{w_{bs}} = \mathbf{R_x^{-1}}\,\mathbf{r_{xy}} \tag{6.12}$$

where

$$\mathbf{R_x} = \mathrm{E}\left\{\mathbf{x}(n)\mathbf{x}^H(n)\right\} \tag{6.13}$$

is the covariance matrix of the signal prediction vector and

$$\mathbf{r_{xy}} = \mathrm{E}\left\{\mathbf{x}(n)y^*(n)\right\} \tag{6.14}$$

is the cross-covariance vector between the signal prediction vector and the mainbeam signal. The adaptive weight vector is applied to the signal prediction vector to form an estimate of the mainbeam interference

$$\hat{y}_i(n) = \mathbf{w_{bs}^H}\,\mathbf{x}(n) \tag{6.15}$$

that is subtracted from the mainbeam signal

$$\tilde{y}(n) = y(n) - \hat{y}_i(n)\ . \tag{6.16}$$

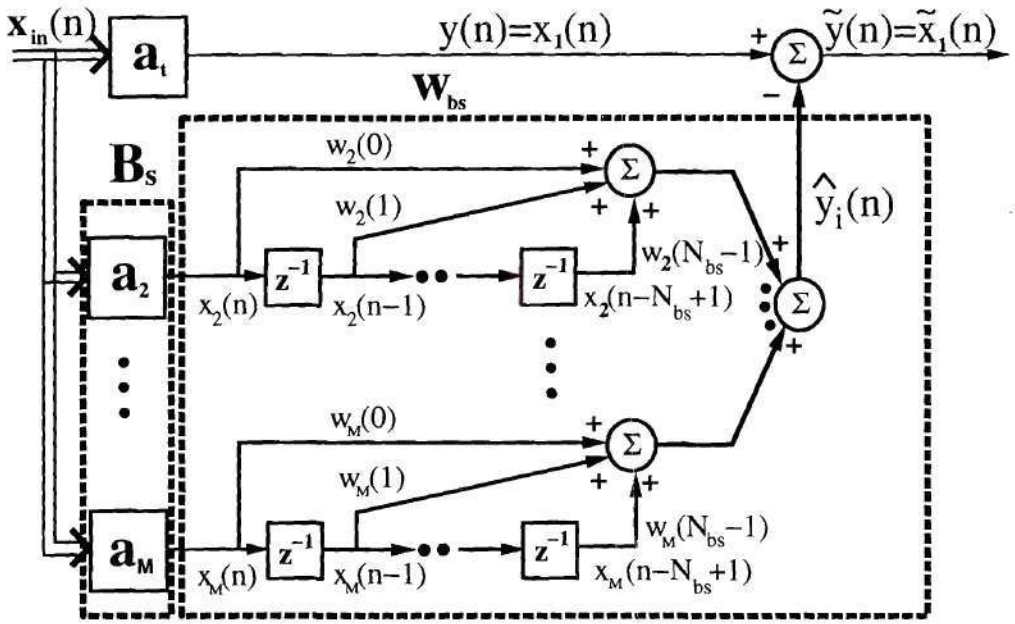

Figure 6.5: Mainbeam jammer beamspace canceler.

The beamspace mainbeam jammer canceler is shown in Fig. 6.5. In practice, the beamspace mainbeam jammer canceler is implemented with the sample matrix inversion (SMI) method [54] using estimates of $\mathbf{R_x}$ and $\mathbf{r_{xy}}$.

One of the concerns with the beamspace canceler is the possibility of multipath from the target signal entering the adaptive canceler through the auxiliary beams. Both signals experience the same amount of attenuation on reflection. However, the target signal tends to be much weaker than the jammer signal. Therefore, the target multipath signal is substantially less than the jammer multipath and is usually below the thermal noise floor. Signals below the thermal noise floor are dominated by the noise and effectively cannot be seen by the adaptive canceler [12, 31]. In the unlikely event of a very strong target signal, a certain amount of signal cancellation may be unavoidable. However, in this case the target can be extracted with a much shorter burn-through time (matched filter length) so that the mitigation of the mainbeam

jammer is probably not necessary. Note that the attenuation on reflection is the reason complete mainbeam jammer cancellation cannot be achieved. Many of the jammer multipath signals drop below the thermal noise floor, limiting the amount of jammer multipath energy available to the adaptive canceler to estimate the mainbeam interference. Therefore, the amount of cancellation possible is determined by the amount of jammer multipath the radar receiver can collect above the thermal noise floor and is dependent on the particular scenario.

The argument against such an approach might be the following: "Why do we expect to have a significant amount of bi-static scattering from the jammer signal?" Typically, the jammer signal is transmitted from an airborne platform where the amount of hardware available to the jammer is limited in both number of the transmitting elements as well as the computational resources. The result is an unsophisticated jammer with a very large beamwidth on its transmit pattern, as well as very high sidelobe levels [57]. The goal of the jammer is to transmit as much interfering energy as possible but not to direct this interference since the actual receiver location may be unknown to the jammer. Though not omni-directional, the transmitter nonetheless produces significant returns over a large sector of the azimuth/elevation plane. Subsequently, a large portion of terrain is illuminated by the jammer signal, creating multipath reflections. In the event that the attenuation of the reflections is so great that most of the jammer multipath falls below the thermal noise floor, suppression of the mainbeam jammer signal is not possible with the proposed beamspace canceler. However, all hope is not lost in this case, at least for the ground-based radar receiver. Numerous strong reflectors can be placed around the receiver at significant ranges in order to produce "artificial" terrain scattering at numerous delays. In order to avoid target leakage into the adaptive predictor, the scatterers should have enough attenuation on reflection to drive the reflections of the target signal below the thermal noise floor. Note that such an approach is similar to the use of an auxiliary array with a different physical location than the main array, known as a sidelobe canceler

[18]. However, the presence of the target signal in the auxiliary array for the sidelobe canceler is almost unavoidable. Thus such an approach is only appropriate for very weak targets.

6.3 Experimental Results

The beamspace canceler is applied to the mainbeam jammer problem using data collected as part of the Mountaintop experiment [40, 61]. The data was collected at White Sands Missile Range with the RSTER-90 radar receiver [13] which has 14 digital azimuth channels from a ULA with the inter-element spacing set to satisfy the spatial aliasing criteria $d = \frac{\lambda}{2}$ for an operating frequency of 450 MHz (λ is the radar wavelength, d is the element spacing). However, in these experiments, the operating frequency is set to 435 MHz.

The mainbeam jammer scenario is easily created by having the assumed target direction coincide with the jammer location in the actual returns. Data collected with a ground-based and an airborne jammer were used to verify the ability to cancel mainbeam jammer interference. Results are reported in terms of signal-to-interference plus noise ratio (SINR) gain, i.e., the difference between jammer energy before and after cancellation. Assuming no signal cancellation, the SINR gain is equivalent to the amount of mainbeam jammer energy cancelled. In addition, target signals were injected prior to processing in order to demonstrate the ability of the beamspace canceler to extract these targets.

6.3.1 Ground-based Jammer

The first data set used consisted of a ground-based jammer located at azimuth angle 302° with a direct-path JNR of approximately 70 dB at the radar receiver. First, we look at the amount of cancellation possible as the number of temporal taps per beam is increased. The assumed target direction is set to $\phi_t = 302°$ to coincide

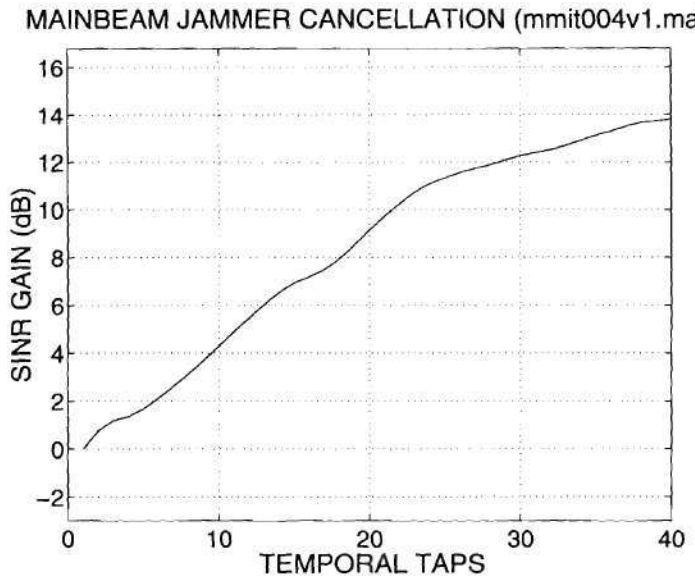

Figure 6.6: SINR gain versus the number of temporal taps per beam (file = `mmit004v1.mat`).

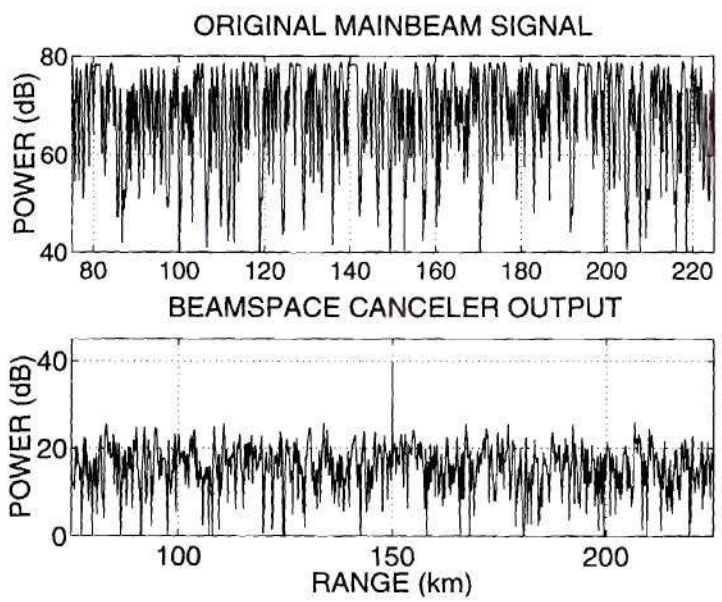

Figure 6.7: Beamspace canceler output normalized to the thermal noise floor (file = `mmit004v1.mat`). Target signal has been injected with an input SNR= 28 dB at the jammer azimuth angle $\phi = 302°$.

with the jammer azimuth. The results are shown in terms of SINR gain versus the number of taps per beam in Fig. 6.6. As expected, the SINR gain improves as the number of taps is increased. Note that 5 dB of suppression is achieved with as few as 12 temporal taps and 10 dB is achieved with just over 20 taps. The number of taps was limited to be less than 40 for computational considerations. The total degrees of freedom for the processor is the number of auxiliary beams (13 in this case) times the number of taps. The SINR gain for 40 taps was near 14 dB. Next, a target signal is injected with an input SNR of 28 dB at a range of 150 kilometers. The beamspace canceler was implemented with 40 taps per beam. The mainbeam signal before and after cancellation is shown in Fig. 6.7. After the 11.5 dB array gain for the 14 elements, the output signal is near 40 dB while the mainbeam jammer has been suppressed to approximately 20 dB. Note that the original mainbeam jammer signal, shown in the top portion of Fig. 6.7, is greater than 70 dB, so that about 50 dB of cancellation was achieved using the beamspace canceler.

6.3.2 Airborne Jammer

The airborne jammer scenario is considered next. In this experiment, the jammer is at an azimuth angle of 268° with a direct-path power of approximately 70 dB. Fig. 6.8 shows the SINR gain as a function of number of temporal taps per beam. In this case, a significant amount of cancellation is achieved even for a very small number of taps. With less than 10 taps per beam, an SINR improvement of greater than 10 dB is achieved. Although the SINR gains level off as the number of taps increases, the improvement in SINR is greater than 15 dB for slightly more than 20 taps. One possible reason for the better performance with the airborne jammer is the fact that aircraft motion causing spreading of the jammer multipath returns. These returns experience a Doppler shift and provide a larger number of independent replicas to the canceler. These results are promising since airborne jammers are more likely in tactical scenarios. Again, a target signal is injected at the same azimuth as the

jammer with an input SNR of 28 dB. The canceler is able to reduce the interference to below 20 dB while increasing the SNR 11.5 dB through the array gain.

6.4 Conclusions

The beamspace canceler used for TSI mitigation in Chapter 3 has been successfully demonstrated as a cancellation method for the mainbeam jammer problem in which the jammer is found in the assumed target direction. The adaptive canceler exploits jammer multipath reflections found in the sidelobes of the steered response in order to estimate and reduce the mainbeam interference. In this sense, the canceler uses all of the available information in the spatial and temporal domains in order to mitigate the interference. The result is significant because any amount of mainbeam jammer suppression directly results in a decrease in the required "burn-through" time, leading to an improvement in the tracking accuracy of the radar.

In the analysis for this chapter, the radar receiver consisted of a ULA with horizontal element placement allowing for adaptivity in azimuth. This receiver uses jammer multipath spread in azimuth to perform the mainbeam jammer cancellation. The generalization to 2-D arrays is straightforward. Here, beamforming is performed in azimuth and elevation, while also maintaining orthogonality between the main and auxiliary beams to prevent target cancellation. In fact, a processor utilizing adaptivity in elevation is anticipated to achieve better mainbeam jammer suppression for certain scenarios with a large amount of jammer multipath in the various elevation sidelobes of the mainbeam. Though the results with the Mountaintop data seem promising, the experiments were performed with the intent of creating jammer multipath. Therefore, to validate the proposed beamspace approach it is necessary to perform additional experiments with actual mainbeam jammers that are not purposely attempting to illuminate terrain.

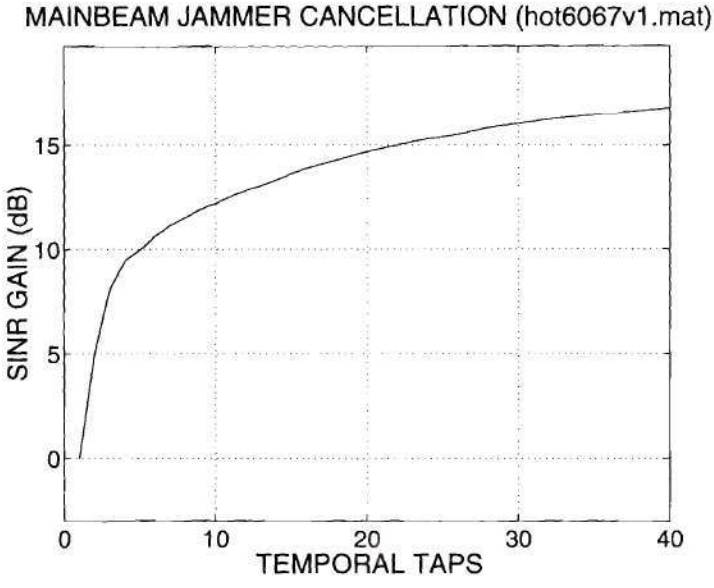

Figure 6.8: SINR gain versus the number of temporal taps per beam (file = `hot6067v1.mat`).

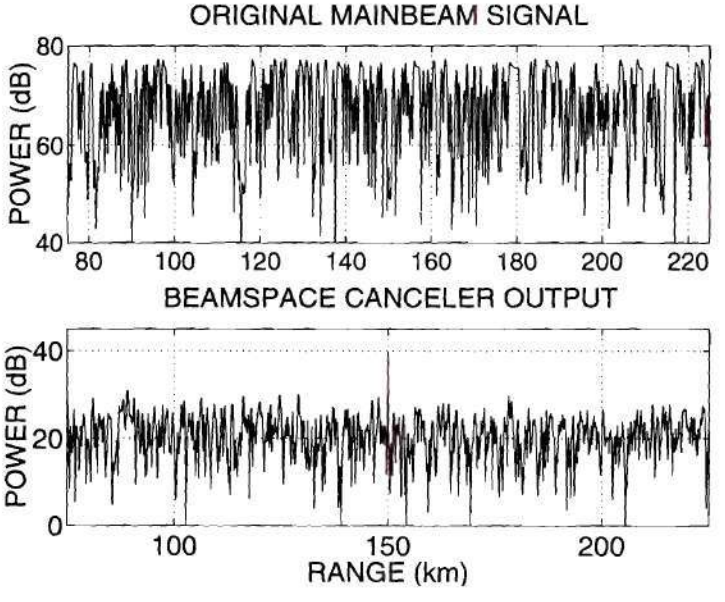

Figure 6.9: Beamspace canceler output normalized to the thermal noise floor (file = `hot6067v1.mat`). Target signal has been injected with an input SNR= 28 dB at the jammer azimuth angle $\phi = 268°$.

CHAPTER 7

Conclusions

The primary topic of this thesis has been the mitigation of TSI using adaptive filters with both spatial and temporal degrees of freedom. The proposed beamspace TSI canceler was shown to provide substantial improvement over the SRB canceler for the cancellation of TSI produced by an airborne jammer. In addition, the length of the blind interval was reduced by using the beamspace as opposed to the SRB approach. These results were verified with experimental TSI returns collected as part of the DARPA/Navy Mountaintop program. Other advantages of the beamspace canceler include the fact it does not require a priori knowledge of the jammer location and is capable of suppressing TSI produced by more than one jamming source. The issue of rank reduction was also addressed in terms of TSI mitigation. For operation in real-time systems, rank reduction becomes a necessity due to computational restrictions and sample support limitations. The study performed in this thesis compared the performance of existing weight thinning strategies applied to the beamspace TSI canceler.

An extension of the beamspace canceler was used in a factored processor for the mitigation of combined TSI and monostatic clutter interference. By preserving the spatial dimensions of the data during TSI mitigation, the processor is able to pass a full CPI data-cube to the monostatic clutter nulling stage. As a result, STAP algorithms can be applied which provide substantial performance gains over simple MTI processing. An important issue when performing factored processing is the

preservation of the monostatic clutter during TSI mitigation. Diagonal loading of the sample covariance matrix was shown to aid in this area, providing the canceler with sufficient robustness to prevent clutter distortion. The factored processor was also demonstrated using experimental TSI and monostatic clutter returns.

The last part of the thesis dealt with the cancellation of mainbeam jammers. In this problem, spatial co-location of the target and jammer prohibits the use of spatial nulling methods. However, exploiting multipath reflections of the jammer signal provides a means of mitigation while preserving the target signal. Space-time adaptive processing using the beamspace canceler was proposed for this problem. The beamspace canceler uses auxiliary beams to collect jammer multipath reflections. The mainbeam jammer signal can then be estimated from these multipath signals. The method was demonstrated on experimental data where it was shown to provide greater than 10 dB of mainbeam jammer suppression. Although the results are promising, more experiments need to be performed to verify this technique at other radar operating frequencies as well as for different interference scenarios.

7.1 Contributions

The contributions of this thesis include:

- The theoretical development of a new TSI mitigation technique that uses a beamspace approach to trade off temporal and spatial degrees of freedom.
- Vast improvement in the cancellation of TSI produced by airborne jammers without the use of Doppler compensation channels.
- Study of various rank reduction methods applied to the TSI problem.
- A factored processor for the mitigation of combined TSI and monostatic clutter.
- Cancellation of mainbeam jammer interference using multipath reflections of the jammer signal.

7.2 Future Work

There are a number of possibilities for future research related to the topics in this thesis. These include:

- The investigation of linear prediction coupled with beamspace TSI mitigation. Such a canceler would have temporal taps in the upper branch of the beamspace canceler and has promise in terms of its TSI cancellation performance. The key issue with the inclusion of temporal taps in the mainbeam is the preservation of the target signal.

- The study of efficient methods for cancelling TSI and monostatic clutter in three dimensions: element, PRI, and range. The implementation of a 3-D adaptive method allows for simultaneous suppression of all interference rather than resorting to a factored approach. Any 3-D adaptive method probably requires the incorporation of rank reduction methods.

- The study of target signal cancellation in adaptive arrays, particularly in the case of factored mitigation of TSI and monostatic clutter.

- The development of mainbeam jammer cancellation experiments in order to further verify the concept. In addition, the performance of the beamspace canceler must be quantified in terms of the amount of reflected TSI energy collected by the radar receiver array. In the absence of jammer multipath, little advantage is anticipated using this beamspace canceler.

- Study more sophisticated jamming techniques. Currently, TSI-producing jammers are modeled as white, Gaussian noise signal. However, more complex waveforms can be used for the TSI jamming source.

APPENDIX A

Symbols and Notation

The notational convention throughout this thesis uses boldfaced lower-case letters to signify complex vectors and boldfaced upper-case letters to signify complex matrices. Otherwise, the symbol denotes a complex scalar. Below is a list of the various symbols used and their respective definitions. The list contains scalars first, followed by vectors, and then matrices. In all cases the symbols appear in alphabetical order with Greek letters at the end.

Table A.1: Symbols and their various definitions.

Symbol	Definition
$\mathrm{E}\{\cdot\}$	mathematical expectation
^{H}	Hermitian operator (complex conjugate transpose)
^{T}	transpose operator
*	complex conjugate operator
$^{-1}$	matrix inverse operator
$\otimes$	Kronecker product operator
$< \cdot, \cdot >$	inner product of two vectors (i.e., $< \mathbf{x}, \mathbf{y} >= \mathbf{y}^H\mathbf{x}$)
	continued on next page

continued from previous page

Symbol	Definition
c	speed of light (3×10^8 meters/second)
c_k	coefficients of eigenvector filters
d	inter-element spacing in uniform linear array
f	Doppler frequency (Hz)
f_p	radar pulse repetition frequency (PRF) (Hz)
f_0	radar operating frequency (Hz)
$\bar{f}$	normalized Doppler frequency ($-0.5 \leq \bar{f} < 0.5$)
$\bar{f}_c$	clutter normalized Doppler frequency ($-0.5 \leq \bar{f}_c < 0.5$)
$\bar{f}_t$	target normalized Doppler frequency ($-0.5 \leq \bar{f}_t < 0.5$)
$h(t, \phi)$	TSI characteristic function
l	PRI or pulse number
m	element number
n	range sample number
n_t	training sample index
r	range (meters)
r_t	target range (meters)
t	continuous time (seconds)
u	spatial frequency ($-0.5 \leq u < 0.5$)
u_c	clutter spatial frequency ($-0.5 \leq u_c < 0.5$)
u_j	jammer spatial frequency ($-0.5 \leq u_j < 0.5$)
u_m	spatial frequency of mth beam ($-0.5 \leq u_m < 0.5$)
u_t	target spatial frequency ($-0.5 \leq u_t < 0.5$)
v	velocity (meters/second)
v_r	radar receiver velocity (meters/second)

continued on next page

continued from previous page

Symbol	Definition
$x_j(t)$	continuous-time jammer signal
$x_m(n)$	mth auxiliary beam signal
$\tilde{x}_m(n)$	TSI-filtered mth auxiliary beam signal
$\tilde{x}_m^{(l)}(n)$	TSI-filtered mth auxiliary beam signal of the lth PRI
$x_r(n)$	reference beam signal in SRB canceler
$x_{tsi}(t, \phi)$	TSI signal at azimuth angle ϕ
$y(n)$	mainbeam signal
$\tilde{y}(n)$	TSI-filtered mainbeam signal
$y_c(n)$	mainbeam monostatic clutter signal
$y_i(n)$	generic mainbeam interference signal
$\hat{y}_i(n)$	estimate of generic mainbeam interference signal
$y_j(n)$	mainbeam direct-path jammer signal
$y_n(n)$	mainbeam thermal noise signal
$y_t(n)$	mainbeam target signal
$y_{tsi}(n)$	mainbeam TSI signal
$\hat{y}_{tsi}(n)$	estimate of mainbeam TSI signal
F_s	A/D sampling frequency
K_F	degrees of freedom of the full-rank adaptive processor
K_R	degrees of freedom of the reduced-rank adaptive processor
L	number of PRIs or pulses in a CPI
M	number of elements in uniform linear array
N	number of range samples in a PRI
N_{bs}	number of samples (per beam) in the temporal window of beamspace canceler

continued on next page

continued from previous page

Symbol	Definition
N_r	number of samples in the temporal window of the SRB canceler
N_t	number of training samples used to compute SMI adaptive weights
R	rank of the interference
SINR_o	signal-to-interference-plus-noise ratio for optimum processor
SINR_{SMI}	signal-to-interference-plus-noise ratio for SMI processor
T_{bs}	length of temporal window of beamspace canceler
T_{jm}	length of interval on the jammer waveform producing jammer multipath signal
T_p	radar pulse period
T_r	length of temporal window of SRB canceler
T_{tsi}	length of interval on jammer waveform producing TSI (range extent)
$\alpha_t(n)$	target signal
$\alpha_j(n)$	jammer signal
$\alpha_c(n,u)$	clutter signal as a function of spatial frequency (azimuth angle)
β	clutter ridge slope
β_k	power of kth strongest interference source
$\delta(\cdot)$	impulse function
γ_k	cross-spectral metric of kth eigenvector
κ	upper bound on white noise gain
ϕ	azimuth angle
ϕ_c	clutter azimuth angle
ϕ_j	jammer azimuth angle
ϕ_m	azimuth angle of mth beam
ϕ_t	target azimuth angle

continued on next page

continued from previous page

Symbol	Definition
λ	wavelength of radar operating frequency (meters)
λ_k	covariance matrix eigenvalue (kth largest magnitude)
$\hat{\lambda}_k$	sample covariance matrix eigenvalue (kth largest magnitude)
ρ	ratio of SINRs from SMI and optimum processors
σ_i^2	interference power
σ_j^2	jammer signal power
σ_l^2	diagonal loading power
σ_n^2	thermal noise power
σ_t^2	target signal power
σ_y^2	mainbeam signal power
$\sigma_{\tilde{y}}^2$	TSI-filtered mainbeam signal power
θ	elevation angle
τ	propagation delay to and from scatterer (seconds)
ξ_k	cross-covariance approximation to the cross-spectral metric
$\mathbf{a}(u)$	spatial steering vector ($M \times 1$)
$\mathbf{a_j}$, $\mathbf{a}(\mathbf{u_j})$	jammer spatial steering vector ($M \times 1$)
$\mathbf{a_m}$, $\mathbf{a}(\mathbf{u_m})$	spatial steering vector ($M \times 1$) of mth beam
$\mathbf{a_r}$, $\mathbf{a}(\mathbf{u_r})$	reference beam spatial steering vector ($M \times 1$) for SRB canceler
$\mathbf{a_t}$, $\mathbf{a}(\mathbf{u_t})$	target spatial steering vector ($M \times 1$)
$\mathbf{b}(\bar{f})$	Doppler steering vector ($L \times 1$)
$\mathbf{b_c}$	clutter Doppler steering vector ($L \times 1$), also $\mathbf{b}(\bar{f}_c)$
$\mathbf{b_t}$, $\mathbf{b}(\bar{\mathbf{f}}_\mathbf{t})$	target Doppler steering vector ($L \times 1$)
$\mathbf{d}$	constraint response vector

continued on next page

continued from previous page

Symbol	Definition
$\mathbf{e_m}$	unit-vector, mth element has value of 1, all other elements have values of 0
$\mathbf{r_m}$	beamspace cross-covariance vector for mth beam
$\hat{\mathbf{r}}_\mathbf{m}$	beamspace sample cross-covariance vector for mth beam
$\mathbf{r_r}$	cross-covariance vector between mainbeam signal $y(n)$ and reference beam signal $x_r(n)$ in SRB canceler
$\hat{\mathbf{r}}_\mathbf{r}$	sample cross-covariance vector between mainbeam signal $y(n)$ and reference beam signal $x_r(n)$ in SRB canceler
$\mathbf{r_{xy}}$	cross-covariance vector between mainbeam signal $y(n)$ and signal prediction vector $\mathbf{x}(n)$
$\hat{\mathbf{r}}_\mathbf{xy}$	sample cross-covariance vector between mainbeam signal $y(n)$ and signal prediction vector $\mathbf{x}(n)$
$\hat{\mathbf{r}}_{\mathbf{xRy}}$	reduced rank cross-covariance vector
$\mathbf{s}(u, \bar{f})$	space-time (azimuth-Doppler) steering vector
$\mathbf{s_c}$	clutter space-time (azimuth-Doppler) steering vector
$\mathbf{s_t}$	target space-time (azimuth-Doppler) steering vector
$\mathbf{v_k}$	covariance matrix eigenvectors (corresponding to kth largest eigenvalue)
$\hat{\mathbf{v}}_\mathbf{k}$	sample covariance matrix eigenvectors (corresponding to kth largest eigenvalue)
$\mathbf{w}$	generic adaptive weight vector
$\hat{\mathbf{w}}$	SMI estimate of generic adaptive weight vector
$\mathbf{w_{bs}}$	beamspace canceler adaptive weight vector
$\hat{\mathbf{w}}_\mathbf{bs}$	SMI estimate of beamspace canceler adaptive weight vector

continued on next page

continued from previous page

Symbol	Definition
$\mathbf{w_d}$	MTI (Doppler) adaptive weight vector
$\hat{\mathbf{w}}_\mathbf{d}$	SMI estimate of MTI (Doppler) adaptive weight vector
$\mathbf{w_e}$	constrained element space processor (CESP) adaptive weight vector
$\hat{\mathbf{w}}_\mathbf{e}$	SMI estimate of constrained element space processor (CESP) adaptive weight vector
$\mathbf{w_m}$	beamspace canceler adaptive weight vector for mth beam
$\hat{\mathbf{w}}_\mathbf{m}$	SMI estimate of beamspace canceler adaptive weight vector for mth beam
$\mathbf{w_q}$	quiescent response weight vector
$\mathbf{w_r}$	SRB canceler adaptive weight vector
$\hat{\mathbf{w}}_\mathbf{r}$	SMI estimate of SRB canceler adaptive weight vector
$\mathbf{w_R}$	reduced rank beamspace canceler adaptive weight vector
$\mathbf{w_{stap}}$	STAP weight vector
$\hat{\mathbf{w}}_\mathbf{stap}$	SMI estimate of STAP weight vector
$\mathbf{x}(n)$	beamspace signal prediction vector
$\mathbf{x_{aux}}(n)$	auxiliary beam signal vector (for one PRI)
$\mathbf{x_{bs}}(n)$	PRI beamspace input signal vector
$\tilde{\mathbf{x}}_\mathbf{bs}(n)$	PRI beamspace output (TSI-filtered) signal vector
$\mathbf{x_c}(n)$	clutter PRI spatial signal vector (result of all azimuth angles)
$\mathbf{x_c}(n,u)$	clutter PRI spatial signal vector as a function of spatial frequency (angle)
$\mathbf{x_d}(n)$	MTI (Doppler) signal prediction vector of TSI-filtered mainbeam signals
$\mathbf{x_e}(n)$	element space signal prediction vector

continued on next page

continued from previous page

Symbol	Definition
$\mathbf{x_i}(n)$	overall interference PRI spatial signal vector
$\mathbf{x_{in}}(n)$	PRI element space input signal vector
$\mathbf{x_{in}^{(l)}}(n)$	PRI element space input signal vector of the lth PRI
$\mathbf{x_j}(n)$	jammer PRI spatial signal vector
$\mathbf{x_{jm}}(n)$	jammer multipath PRI spatial signal vector
$\mathbf{x_m}(n)$	mth auxiliary beam signal vector (contains delayed versions of $x_m(n)$)
$\mathbf{x_n}(n)$	thermal noise PRI spatial signal vector
$\mathbf{x_{out}}(n)$	PRI element space output (TSI-filtered) signal vector
$\mathbf{x_{out}^{(l)}}(n)$	PRI element space output (TSI-filtered) signal vector of the lth PRI
$\mathbf{x_r}(n)$	reference beam signal prediction vector made up of delays of $x_r(n)$
$\mathbf{x_t}(n)$	target PRI spatial signal vector
$\mathbf{x_{tsi}}(n)$	TSI PRI spatial signal vector (resulting from all azimuth angles)
$\mathbf{x_{tsi}}(n, \phi)$	TSI PRI spatial signal vector at azimuth angle ϕ
$\mathbf{x_R}(n)$	reduced rank beamspace signal prediction vector
$\mathbf{y}$	beamspace canceler upper branch data vector
$\mathbf{z_c}(n)$	CPI clutter space-time signal vector ($ML \times 1$)
$\mathbf{z_i}(n)$	CPI overall interference space-time signal vector ($ML \times 1$)
$\mathbf{z_{in}}(n)$	CPI input space-time signal vector ($ML \times 1$)
$\mathbf{z_j}(n)$	CPI jammer space-time signal vector ($ML \times 1$)
$\mathbf{z_t}(n)$	CPI target space-time signal vector ($ML \times 1$)
$\mathbf{z_{tsi}}(n)$	TSI CPI space-time signal vector (resulting from all azimuth angles)
$\mathbf{z_{tsi}}(n, \phi)$	TSI CPI space-time signal vector at azimuth angle ϕ
$\mathbf{B_s}$	spatial blocking matrix
$\mathbf{B_{st}}$	space-time (range) blocking matrix

continued on next page

continued from previous page	
Symbol	Definition
$\mathbf{C}$	constraint matrix
$\mathbf{I}$	identity matrix
$\mathbf{P_R}$	rank reduction projection matrix ($K_F \times K_R$)
$\mathbf{R}$	generic covariance matrix
$\mathbf{R_d}$	MTI (Doppler) covariance matrix of Doppler signal prediction vector
$\hat{\mathbf{R}}_\mathbf{d}$	MTI (Doppler) sample covariance matrix of Doppler signal prediction vector
$\mathbf{R_e}$	element space signal prediction vector covariance matrix
$\hat{\mathbf{R}}_\mathbf{e}$	element space signal prediction vector sample covariance matrix
$\mathbf{R_i}$	interference covariance matrix
$\mathbf{R_m}$	beamspace covariance matrix for mth beam
$\hat{\mathbf{R}}_\mathbf{m}$	beamspace sample covariance matrix for mth beam
$\mathbf{R_n}$	thermal noise covariance matrix
$\mathbf{R_r}$	covariance matrix of reference beam signal in SRB canceler
$\hat{\mathbf{R}}_\mathbf{r}$	sample covariance matrix of reference beam signal in SRB canceler
$\mathbf{R_R}$	reduced rank covariance matrix of beamspace signal prediction vector
$\mathbf{R_x}$	covariance matrix of beamspace signal prediction vector
$\hat{\mathbf{R}}_\mathbf{x}$	sample covariance matrix of beamspace signal prediction vector
$\mathbf{R_{tsi}}$	TSI covariance matrix
$\mathbf{R_z}$	covariance matrix of element space CPI space-time signal vector
$\hat{\mathbf{R}}_\mathbf{z}$	sample covariance matrix of element space CPI space-time signal vector
$\mathbf{T}$	transform from element space to beamspace
$\mathbf{X}$	beamspace canceler signal prediction data matrix
$\mathbf{Z_{in}}(n)$	CPI input range slice matrix ($M \times L$)

APPENDIX B

Acronyms

This appendix consists of a table with the acronyms and their respective meanings that are used throughout the thesis.

Table B.1: Acronyms and their respective meanings.

Acronym	Meaning
A/D	analog to digital
CESP	constrained element space processor
CNR	clutter-to-noise ratio
CPI	coherent processing interval
dB	decibel
DOF	degrees of freedom
GSC	generalized sidelobe canceler
INR	interference-to-noise ratio
JNR	jammer-to-noise ratio
km	kilometers
LCMV	linearly constrained minimum variance
LFM	linear frequency modulation
ML	maximum likelihood
MMSE	minimum mean-squared error

continued on next page

continued from previous page	
Acronym	Meaning
MTI	moving target indicator
MVDR	minimum variance distortionless response
PRF	pulse repetition frequency
PRI	pulse repetition interval
RCS	radar cross section
SRB	single-reference beam
SINR	signal-to-interference-plus-noise ratio
SMI	sample matrix inversion
SNR	signal-to-noise ratio
STAP	space-time adaptive processing
ULA	uniform linear array
TSI	terrain scattered interference

Bibliography

[1] R. N. Adams, L. L. Horowitz, and K. D. Senne. Adaptive main beam nulling for narrow-beam antenna systems. *IEEE Trans. on Aerospace and Electronic Systems*, 16(3):509–516, July 1980.

[2] H. M. Aumann, J. Ward, and F. G. Willwerth. Inverse diplaced phased center array for aircraft motion emulation. In *Proc. of 14th Antenna Measurement and Techniques Conf.*, 1992.

[3] W. P. Ballance and T. W. Miller. Impact of mainlobe interference angular extent on adaptive beamforming. In *Proc. of Asilomar Conf. on Signals, Systems, and Computers*, pages 989–993, 1991.

[4] D. M. Boroson. Sample size considerations for adaptive arrays. *IEEE Trans. on Aerospace and Electronic Systems*, 16(4):446–451, July 1980.

[5] L. E. Brennan. Preliminary results of hot clutter cancellation tests using WSMR data. In *Proc. of Adaptive Sensor Array Processing Workshop*, volume 2, pages 515–537. MIT Lincoln Laboratory, 1995.

[6] L. E. Brennan, J. D. Mallett, and I. S. Reed. Adaptive arrays in airborne MTI radar. *IEEE Trans. on Antennas and Propagation*, 24(5):607–615, Sept. 1976.

[7] L. E. Brennan and I. S. Reed. Optimum processing of unequally spaced radar pulse trains for clutter rejection. *IEEE Trans. on Aerospace and Electronic Systems*, 4(3):474–477, May 1968.

[8] L. E. Brennan and I. S. Reed. Theory of adaptive radar. *IEEE Trans. on Aerospace and Electronic Systems*, 9(2):237–252, Mar. 1973.

[9] E. Brookner and J. M. Howell. Adaptive-adaptive array processing. *Proc. of the IEEE*, 74(4):602–604, Apr. 1986.

[10] K. A. Byerly and R. A. Roberts. Output power based partial adaptive array design. In *Proc. of Asilomar Conf. on Signals, Systems, and Computers*, pages 576–579, 1989.

[11] J. Capon. High-resolution frequency-wavenumber spectrum analysis. *Proc. of the IEEE*, 57(8):1408–1418, Aug. 1969.

[12] B. D. Carlson. Covariance matrix estimation errors and diagonal loading in adaptive arrays. *IEEE Trans. on Aerospace and Electronic Systems*, 24(4):397–401, July 1988.

[13] B. D. Carlson *et al.* An ultralow sidelobe adaptive array antenna. *The Lincoln Laboratory Journal*, 3(2):291–310, Summer 1990.

[14] D. J. Chapman. Partial adaptivity for the large array. *IEEE Trans. on Antennas and Propagation*, 24(5):685–696, Sept. 1976.

[15] R. T. Compton. *Adaptive Arrays:Concepts and Performance.* Prentice-Hall, Englewood Cliffs, NJ, 1988.

[16] J. F. Doherty. Suppression of terrain-scattered jamming in pulse compression radar. *IEEE Signal Processing Letters*, 2(1):4–6, Jan. 1995.

[17] R. L. Fante. Cancellation of specular and diffuse jammer multipath using a hybrid adaptive array. *IEEE Trans. on Aerospace and Electronic Systems*, 27(5):823–837, Sept. 1991.

[18] R. L. Fante, T. P. Guella, and R. M. Davis. Wideband cancellation of multiple mainbeam jammers. *IEEE Trans. on Antennas and Propagation*, 44(10):1402–1413, Oct. 1996.

[19] R. L. Fante and J. A. Torres. Cancellation of diffuse jammer multipath by an airborne adaptive radar. *IEEE Trans. on Aerospace and Electronic Systems*, 31(2):805–820, Apr. 1995.

[20] O. L. Frost. An algorithm for linearly constrained adaptive array processing. *Proc. of the IEEE*, 60(8):926–935, Aug. 1972.

[21] R. A. Gabel. Mountaintop bistatic jamming experiments and analysis. In *Proc. of Adaptive Sensor Array Processing Workshop*, volume 2, pages 493–513. MIT Lincoln Laboratory, 1995.

[22] R. A. Gabel. TSI mitigation weight training experiments. In *Proc. of the 3rd ARPA Mountaintop Hot Clutter TIM*, pages 249–294. USAF Rome Laboratory, 1995.

[23] W. F. Gabriel. Using spectral estimation techniques in adaptive processing antenna systems. *IEEE Trans. on Antennas and Propagation*, 34(3):291–299, Mar. 1986.

[24] M. W. Ganz, J. Ward, and B. D. Carlson. Adaptive nulling with adaptive array interferometry. In *Proc. of Asilomar Conf. on Signals, Systems, and Computers*, pages 974–978, 1991.

[25] J. S. Goldstein *et al.* Inter-space and intra-space transformations for sensor array processing. In *Proc. of Asilomar Conf. on Signals, Systems, and Computers*, pages 638–642, 1994.

[26] J. S. Goldstein, D. B. Williams, and E. J. Holder. A frequency domain realization of an optimum partially adaptive sensor array. In *Proc. of IEEE MILCOM*, volume 2, pages 607–611, 1995.

[27] G. H. Golub and C. F. Van Loan. *Matrix Computations.* The Johns Hopkins University Press, Baltimore, MD, 1989.

[28] L. J. Griffiths and C. W. Jim. An alternative approach to linearly constrained adaptive beamforming. *IEEE Trans. on Antennas and Propagation*, 30(1):27–34, Jan. 1982.

[29] A. E. Hoerl and R. W. Kennard. Ridge regression: Biased estimation for nonorthogonal problems. *Technometrics*, 12(1):55–67, Feb. 1970.

[30] J. E. Hudson. *Adaptive Array Principles.* Peter Peregrinus, London, 1981.

[31] N. K. Jablon. Adaptive beamforming with the generalized sidelobe canceler in the presence of array imperfections. *IEEE Trans. on Antennas and Propagation*, 34(8):996–1012, Aug. 1986.

[32] D. H. Johnson and D. E. Dudgeon. *Array Signal Processing.* Prentice-Hall, Englewood Cliffs, NJ, 1993.

[33] I. I. Jouny and E. Culpepper. Modeling and mitigation of terrain scattered interference. In *Proc. of IEEE Int. Symp. on Antennas and Propagation*, volume 1, pages 455–457, 1995.

[34] E. J. Kelly. An adaptive detection algorithm. *IEEE Trans. on Aerospace and Electronic Systems*, 22(1):115–127, Mar. 1986.

[35] R. Klemm. Adaptive clutter suppression for airborne phased array radars. *IEE Proc. Part F and H*, 1:125–131, Feb. 1983.

[36] S. M. Kogon, D. B. Williams, and E. J. Holder. Beamspace mitigation of terrain scattered interference in airborne radar systems. submitted to *IEEE Trans. on Aerospace and Electronic Systems*, 1996.

[37] S. M. Kogon, D. B. Williams, and E. J. Holder. Beamspace techniques for hot clutter cancellation. In *Proc. of IEEE Int. Conf. on Acoustics, Speech, and Signal Processing*, volume 2, pages 1177–1180, May 1996.

[38] S. M. Kogon, D. B. Williams, and E. J. Holder. Reduced rank terrain scattered interference mitigation. In *IEEE Int. Sym. on Phased Array Sys. and Tech.*, pages 400–405, 1996.

[39] S. M. Kogon, D. B. Williams, and J. H. McClellan. Factored mitigation of terrain scattered interference and monostatic clutter. In *Proc. of Asilomar Conf. on Signals, Systems, and Computers*, to appear, 1996.

[40] USAF Rome Laboratory. Mountaintop program summit data. ASAP 1995 Data Release, Mar. 1995.

[41] N. Levanon. *Radar Principles.* John Wiley & Sons, New York, NY, 1988.

[42] R. L. C. Lin and F. Kretschmer. Angle measurement in the presence of mainbeam interference. *IEEE Aerospace and Electronic Systems Magazine*, pages 19–25, Nov. 1990.

[43] T. T. Ma and L. J. Griffiths. A solution space approach to achieving partially adaptive arrays. In *Proc. of IEEE Int. Conf. on Acoustics, Speech, and Signal Processing*, pages 2869–2872, 1988.

[44] D. Marquardt. Generalized inverses, ridge regression, biased linear estimation, and nonlinear estimation. *Technometrics*, 12:591–612, 1970.

[45] D. F. Marshall. A two step adaptive interference nulling algorithm for use with airborne sensor arrays. In *Proc. of the Seventh SP Workshop on Statistical Signal and Array Processing*, pages 301–304, 1994.

[46] D. F. Marshall and R. A. Gabel. Simultaneous mitigation of multipath jamming and ground clutter. In *Proc. of Adaptive Sensor Array Processing Workshop*, volume 1, pages 285–313. MIT Lincoln Laboratory, 1996.

[47] T. W. Miller and J. M. Ortiz. An overview of issues in hot clutter mitigation. In *Proc. of Adaptive Sensor Array Processing Workshop*, volume 1, pages 193–239. MIT Lincoln Laboratory, 1996.

[48] R. A. Monzingo and T. W. Miller. *Introduction to Adaptive Arrays.* John Wiley & Sons, New York, NY, 1980.

[49] D. R. Morgan. Partially adaptive array techniques. *IEEE Trans. on Antennas and Propagation*, 26(6):823–833, Nov. 1978.

[50] D. R. Morgan and A. Aridgides. Adaptive sidelobe cancellation of wide-band multipath interference. *IEEE Trans. on Antennas and Propagation*, 33(8):908–917, Aug. 1985.

[51] F. E. Nathanson. *Radar Design Principles: Signal Processing and the Environment.* McGraw-Hill, New York, NY, 2nd edition, 1991.

[52] N. L. Owsley. Chapter in *Array Signal Processing* , ed., S. Haykin, Sonar Array Processing, pages 115–193. Prentice-Hall, Englewood Cliffs, NJ, 1985.

[53] A. Papoulis. *Probability, Random Variables, and Stochastic Processes.* McGraw-Hill, New York, NY, 3rd edition, 1991.

[54] I. S. Reed, J. D. Mallett, and L. E. Brennan. Rapid convergence rate in adaptive arrays. *IEEE Trans. on Aerospace and Electronic Systems*, 10(6):853–863, Nov. 1974.

[55] L. L. Scharf. *Statistical Signal Processing: Detection, Estimation, and Time Series Analysis.* Addison-Wesley, Reading, MA, 1991.

[56] J. B. Schodorf and D. B. Williams. Partially adaptive multiuser detection. In *Proc. of IEEE Vehicular Tech. Conf.*, pages 367–371, 1996.

[57] M. I. Skolnik. *Introduction to Radar Systems.* McGraw-Hill, New York, NY, 2nd edition, 1980.

[58] M. I. Skolnik. *Radar Handbook.* McGraw-Hill, New York, NY, 2nd edition, 1990.

[59] K. Takao and K. Uchida. Beamspace partially adaptive antenna. *IEE Proc. Part H*, 136(6):439–444, Dec. 1989.

[60] A. Theil. Adaptive nullsteering of main lobe jamming; analysis of the ARTIST trials. In *Proc. of IEEE Int. Radar Conference*, pages 103–107, 1995.

[61] G. W Titi and D. F. Marshall. The ARPA/Navy mountaintop program: Adaptive signal processing for airborne early warning radar. In *Proc. of IEEE Int. Conf. on Acoustics, Speech, and Signal Processing*, volume 2, pages 1165–1168, 1996.

[62] D. W. Tufts and I. P. Kirsteins. Chapter in *High-Resolution Methods in Underwater Acoustics* , ed., M. Bouvet and G. Bienvenu, Rapidly Adaptive Nulling of Interference, pages 217–249. Springer-Verlag, New York, NY, 1991.

[63] M. Unser. On the approximation of the discrete Karhunen-Loève transform for stationary processes. *Signal Processing*, 7(3):231–249, Dec. 1984.

[64] B. D. Van Veen. Eigenstructure based partially adaptive array design. *IEEE Trans. on Antennas and Propagation*, 36(3):357–362, Mar. 1988.

[65] B. D. Van Veen. An analysis of several partially adaptive beamformer designs. *IEEE Trans. on Acoustics, Speech, and Signal Processing*, 37(2):192–203, Feb. 1989.

[66] B. D. Van Veen and R. A. Roberts. Partially adaptive beamformer design via output power minimization. *IEEE Trans. on Acoustics, Speech, and Signal Processing*, 35(11):1524–1532, Nov. 1987.

[67] J. Ward. Space-time adaptive processing for airborne radar. Technical Report 1015, MIT Lincoln Laboratory, 1994.

[68] B. Widrow, P. Mantey, L. Griffiths, and B. Goode. Adaptive antenna systems. *Proc. of the IEEE*, 55(12):2143–2159, Dec. 1967.

[69] C. L. Zahm. Application of adaptive arrays to suppress strong jammers in the presence of weak signals. *IEEE Trans. on Aerospace and Electronic Systems*, 9(2):260–271, Mar. 1973.

Vita

Stephen M. Kogon was born in Mt. Kisco, New York on October 16, 1965. He received the B.S. degree in Electrical Engineering from Rensselaer Polytechnic Institute in May 1987 and the M.S. degree in Electrical Engineering from Worcester Polytechnic Institute in December 1993. He received the Ph.D. degree in Electrical Engineering from the Georgia Institute of Technology in December 1996.

He was employed at Raytheon Company, Equipment Division in the Signal Processing Department of the Radar Systems Laboratory from 1987 to 1992. From 1992 to 1993, he was with Boston College, Institute for Space Research. Since 1994 he has been a graduate research assistant in both the School of Electrical and Computer Engineering at the Georgia Institute of Technology and at Georgia Tech Research Institute (GTRI) in the Sensors and Electromagnetic Applications Laboratory. He has recently accepted a technical research staff position at MIT Lincoln Laboratories as part of the Advanced Electromagnetic Systems group (Group 108). His research interests include adaptive array and statistical signal processing, radar, and long-memory or fractal signal modeling.